

University of Nebraska - Lincoln

**DigitalCommons@University of Nebraska - Lincoln**

---

Mechanical (and Materials) Engineering --  
Dissertations, Theses, and Student Research

Mechanical & Materials Engineering, Department  
of

---

Summer 8-2016

# Design, Testing and Evaluation of Robotic Mechanisms and Systems for Environmental Monitoring and Interaction

James K. Higgins

*University of Nebraska - Lincoln*, [jhiggins09@hotmail.com](mailto:jhiggins09@hotmail.com)

Follow this and additional works at: <http://digitalcommons.unl.edu/mechengdiss>



Part of the [Electro-Mechanical Systems Commons](#)

---

Higgins, James K., "Design, Testing and Evaluation of Robotic Mechanisms and Systems for Environmental Monitoring and Interaction" (2016). *Mechanical (and Materials) Engineering -- Dissertations, Theses, and Student Research*. 99.  
<http://digitalcommons.unl.edu/mechengdiss/99>

This Article is brought to you for free and open access by the Mechanical & Materials Engineering, Department of at DigitalCommons@University of Nebraska - Lincoln. It has been accepted for inclusion in Mechanical (and Materials) Engineering -- Dissertations, Theses, and Student Research by an authorized administrator of DigitalCommons@University of Nebraska - Lincoln.

DESIGN, TESTING AND EVALUATION OF ROBOTIC MECHANISMS AND  
SYSTEMS FOR ENVIRONMENTAL MONITORING AND INTERACTION

by

James K Higgins

A THESIS

Presented to the Faculty of

The Graduate College at the University of Nebraska

In Partial Fulfilment of Requirements

For the Degree of Master of Science

Major: Mechanical Engineering and Applied Mechanics

Under the Supervision of Carrick Detweiler and Carl Nelson

Lincoln, Nebraska

August, 2016



# DESIGN, TESTING AND EVALUATION OF ROBOTIC MECHANISMS AND SYSTEMS FOR ENVIRONMENTAL MONITORING AND INTERACTION

James K Higgins, M.S.

University of Nebraska, 2016

Adviser: Carrick Detweiler and Carl Nelson

Unmanned Aerial Vehicles (UAVs) have significantly lowered the cost of remote aerial data collection. The next generation of UAVs, however, will transform the way that scientists and practitioners interact with the environment. In this thesis, we address the challenges of flying low over water to collect water samples and temperature data. We also develop a system that allows UAVs to ignite prescribed fires. Specifically, this thesis contributes a new peristaltic pump designed for use on a UAV for collecting water samples from up to 3m depth and capable of pumping over 6m above the water. Next, temperature sensors and their deployment on UAVs, which have successfully created a 3D thermal structure map of a lake, contributes to mobile sensors. A sub-surface sampler, the “Waterbug” which can sample from 10m deep and vary buoyancy for longer in-situ analysis contributes to robotics and mobile sensors. Finally, we designed and built an Unmanned Aerial System for Fire Fighting (UAS-FF), which successfully ignited over 150 acres of prescribed fire during two field tests and is the first autonomous robot system for this application.

## DEDICATION

To my wife, Callie and our two boys, Mathias and Jediah. I'm grateful for the sacrifices you made so that I could have this opportunity.

## ACKNOWLEDGMENTS

Thank you to our limnologist and environmental engineering partners Dr. Michael Hamilton and Dr. Sally Thompson, and our invasive species and wildlife partners Allison Zach, and Dr. Craig Allen for their support of these efforts. Thank you to Dr. Dirac Twidwell, Evan Beachly, Christian Laney, and Becca Horzewski for their contributions to the prescribed fire and UAS-FF work. Thank you to all the members of the NIMBUS lab for their assistance with computer science and electronics matters. A special thank you to John-Paul for collaborating with me on many of the water research projects, it was a pleasure working with you. Thank you to Dr. Carrick Detweiler, Dr. Sebastian Elbaum, and Dr. Carl Nelson for their input and guidance.

## GRANT INFORMATION

This work was partially supported by USDA-NIFA 2013-67021-20947 and a graduate research fellowship from the Robert B. Daugherty Water for Food Institute. Any opinions, findings, conclusions, or recommendations expressed in this material are those of the authors and do not necessarily reflect the views of these agencies.

# Contents

<b>Contents</b>	<b>vi</b>
<b>List of Figures</b>	<b>x</b>
<b>List of Tables</b>	<b>xiv</b>
<b>1 Introduction</b>	<b>1</b>
1.1 Water Impact . . . . .	2
1.2 Sensing and Sampling . . . . .	3
1.3 Prescribed Fire . . . . .	4
1.4 Contributions . . . . .	5
1.5 Thesis Overview . . . . .	7
<b>2 Background and Related Work</b>	<b>8</b>
2.1 Peristaltic Pump . . . . .	8
2.2 Temperature Sensing . . . . .	11
2.3 Sub-Surface Sampling . . . . .	15
2.4 Control Theory . . . . .	19
2.5 Fire . . . . .	22
<b>3 UAV Sensing and Sampling</b>	<b>25</b>

3.1	UAV Platform . . . . .	25
3.2	UAV Sensing and Sampling: Pumps . . . . .	27
3.2.1	Pump Requirements . . . . .	27
3.2.2	Pump Design . . . . .	28
3.2.3	Pump Bench Tests . . . . .	30
3.2.4	Pump Field Tests . . . . .	33
3.2.5	Pump Summary and Contributions . . . . .	38
3.3	UAV Sensing and Sampling: Temperature Sensors . . . . .	40
3.3.1	Temperature Sensor Motivation and Requirements . . . . .	40
3.3.2	Temperature Sensor Bench Tests . . . . .	41
3.3.3	Temperature Sensor Field Tests . . . . .	46
3.3.4	Temperature Sensor Summary and Contributions . . . . .	52
<b>4</b>	<b>The Waterbug</b>	<b>53</b>
4.1	System Requirements . . . . .	53
4.2	Previous Iterations . . . . .	55
4.3	Final Mechanical Design . . . . .	59
4.3.1	Pneumatic System . . . . .	60
4.3.2	Sample Collection System . . . . .	62
4.3.3	Buoyancy Control System . . . . .	62
4.3.4	3D Printed Parts . . . . .	63
4.4	Electrical and Software Design . . . . .	64
4.4.1	Microcontroller . . . . .	64
4.4.2	Communications . . . . .	64
4.4.3	Sensors . . . . .	65
4.4.4	Mechanical Actuation . . . . .	65

4.4.5	Power . . . . .	66
4.4.6	Software . . . . .	66
4.5	Waterbug Control . . . . .	67
4.5.1	Challenges, Goals and Assumptions . . . . .	67
4.5.2	Computational Fluid Dynamics (CFD) Analysis . . . . .	69
4.5.3	Mathematical Model . . . . .	71
4.6	System Sensitivity . . . . .	75
4.7	Neutral Buoyancy Algorithm . . . . .	77
4.8	Evaluation . . . . .	79
4.8.1	Maximum Depth . . . . .	79
4.8.2	Neutral Buoyancy . . . . .	80
4.9	Waterbug Summary and Contributions . . . . .	83
<b>5</b>	<b>Prescribed Fire and the UAS-FF</b>	<b>84</b>
5.1	System Requirements . . . . .	85
5.2	Mechanical Design . . . . .	86
5.2.1	Version 1.0 . . . . .	87
5.2.2	Version 2.0 . . . . .	96
5.3	Evaluation . . . . .	103
5.3.1	Version 1.0.3 Evaluation . . . . .	104
5.3.2	Version 2.0.1 Evaluation . . . . .	106
5.4	Conclusion and Contributions . . . . .	109
<b>6</b>	<b>Conclusion and Future Work</b>	<b>111</b>
6.1	UAV Sensing and Sampling . . . . .	111
6.2	Waterbug . . . . .	112
6.3	UAS-FF . . . . .	113

6.4 Contributions . . . . .	114
<b>Bibliography</b>	<b>117</b>



# List of Figures

1.1	(a) Temperature sensor on UAV during testing (b) Peristaltic pump mounted on UAV (c) Waterbug sub-surface sampler in pool test (d) UAS-FF during field testing . . . . .	1
1.2	Fire fighters deploy UAVs equipped with fire starting mechanisms from a safe location. The left UAV monitors conditions in an occluded area and the right UAV drops ignition spheres to continue a line of fire.	4
2.1	Diagram of part of the peristaltic pump designed for UAV-based water sampling . . . . .	9
2.2	Block diagram of open loop control . . . . .	19
2.3	Block diagram of feedback control . . . . .	20
2.4	Interior ignition being conducted from an ATV . . . . .	23
3.1	Ascending Technologies Firefly . . . . .	26
3.2	Final peristaltic pump design with small motor . . . . .	29
3.3	Peristaltic pump characterization and performance for different voltages and altitudes . . . . .	31
3.4	Peristaltic pump mounted on Astec Firefly . . . . .	34

3.5	(a) Inlet side of tube and clamp/bobber float for controlling depth of sampling (b) Outlet side of tube with 64 micron filter and threaded adapter . . . . .	35
3.6	The black lines show the locations sampled for Zebra mussel veligers. .	36
3.7	Zebra mussel veligers captured by the UAV water filtering system . . .	38
3.8	MS5803 IC on a custom circuit board . . . . .	41
3.9	Comparison of HOBO and MS5803 . . . . .	43
3.10	(a) Thermocouple constructed with accompanying circuitry (b) thermistor constructed . . . . .	44
3.11	Temperature sensors' response when plunged into ice water . . . . .	45
3.12	Location of the HOBO arrays and sample locations for one experiment set . . . . .	47
3.13	Raw and filtered temperature data from UAV-mounted sensor. The filtering removed data when either temperature or depth were rapidly changing. . . . .	47
3.14	Comparison of UAS-borne and in-situ temperature sensors, including logged data and detected thermal gradient. (a) Bias in temperature measured at each depth (b) Comparison of derived temperature gradient at each depth . . . . .	50
3.15	Thermal structure of a $10 \times 10 \times 2.5\text{m}$ grid, interpolated and reconstructed from two UAS flights. White arrows indicate UAS's sampling locations, depth measurements were made throughout the water column at these sites. . . . .	51
4.1	(a) Waterbug Revision 1.1 (b) Section view of Revision 1.1 (c) Waterbug Revision 1.2 (d) Waterbug Revision 1.3 (e) Waterbug Revision 1.4 . . . .	56

4.2	(a) Rendering of final model (b) Completed prototype in water during testing . . . . .	60
4.3	(a) Pneumatic system (b) Sample collection system (c) Buoyancy control system . . . . .	61
4.4	Electrical hardware design courtesy of John-Paul Ore . . . . .	64
4.5	Section view of CFD analysis . . . . .	69
4.6	Drag force vs. velocity curve for CFD data combined with validation tests . . . . .	70
4.7	(a) Simulated depth for correct initial pressure (b) Simulated depth for under-pressurized tank (c) Simulated depth for over-pressurized tank .	76
4.8	10ft vertical water column for in-water lab testing . . . . .	81
4.9	Depth and descent rate data for a neutral buoyancy trial . . . . .	82
5.1	Autonomous aerial fire ignition system during a field trial . . . . .	84
5.2	The four subsystems that make up V1.0.3 of the fire ignition mechanism of the UAS-FF . . . . .	88
5.3	Ignition sphere in loading/releasing mechanism, ready to be processed through the ignition procedure . . . . .	89
5.4	Section View: Ignition sphere punctured onto needle by piercing mechanism . . . . .	90
5.5	Injection system squirts a small amount of fluid from syringe into ignition sphere . . . . .	91
5.6	Loading/releasing mechanism rotates again to move the ignition sphere to the bottom of the mechanism where it drops out of the UAS-FF . . .	92
5.7	(a) Version 1.0.1 with under-mounted hopper (b) Version 1.0.2 with over-mounted gravity fed hopper (c) Version 1.0.3 with agitated hopper	92

5.8	(a) Version 2.0.1 on the UAV with new mounting mechanism and hopper (b) Version 2.0.1 mechanism . . . . .	96
5.9	The four subsystems that make up version 2.0 of the fire ignition mechanism of the UAS-FF . . . . .	97
5.10	Section View: “C” shaped hopper chute to help keep design compact and align center of mass with UAV center . . . . .	98
5.11	Loading/releasing mechanism positioning a sphere in preparation for puncturing . . . . .	99
5.12	Section View: Piercing mechanism punctures a sphere for injection . . .	100
5.13	Injection mechanism primes the sphere with antifreeze . . . . .	101
5.14	Version 2.0 mounting mechanism that securely holds but quickly releases the mechanism . . . . .	102
5.15	UAS-FF Version 1.0.3 in flight . . . . .	103
5.16	UAS-FF returning from a sortie, flying 10 meters over ignited trees. In-picture shows trajectory on a 50m by 35m area, white markers indicate spheres dropped. . . . .	105
5.17	UAS-FF Version 2.0.1 outfitted for deployment . . . . .	107
5.18	Burn unit with flight paths flown by UAS-FF and burn perimeter started from the ground marked . . . . .	108
5.19	Locations of dropped ignition spheres as seen from the UAS-FF’s perspective . . . . .	109

# List of Tables

3.1	Summary of the power required to fly with the two peristaltic pumps and the overall efficiency . . . . .	32
3.2	Comparison of the three pumps at 1m altitude . . . . .	32
3.3	Sensor specifications . . . . .	42
3.4	Experimentally determined temperature sensor specifications . . . . .	45
4.1	Results of neutral buoyancy attempts . . . . .	82

# Chapter 1

## Introduction

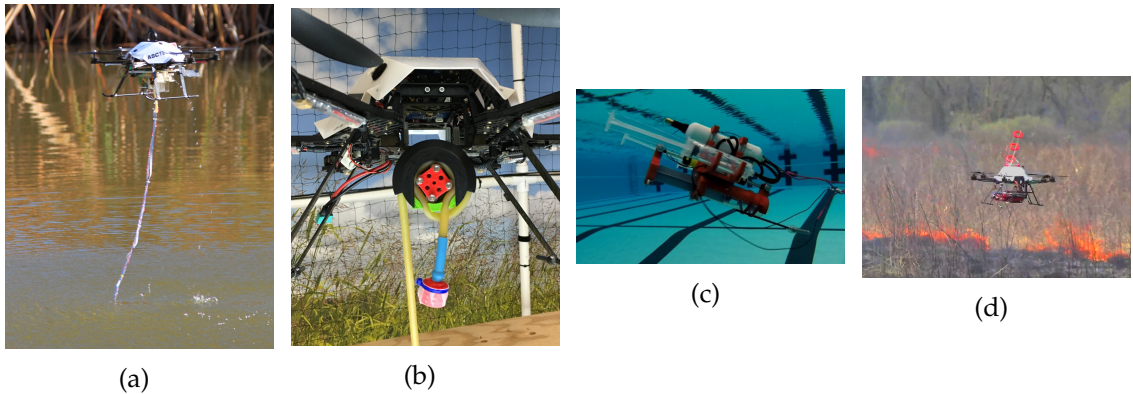


Figure 1.1: (a) Temperature sensor on UAV during testing (b) Peristaltic pump mounted on UAV (c) Waterbug sub-surface sampler in pool test (d) UAS-FF during field testing

The next generation of UAVs will be highly interactive with the environment. In this thesis we develop a number of electro-mechanical systems that can augment existing UAVs or work alongside them to enable environmental interactions. Key to all of these systems is the development of light-weight and robust mechanical designs that meet the requirements of the scientists and practitioners that use them. Chapters 3 and 4 of this thesis are focused on data collection and wa-

ter sampling with a temperature sensor shown in Figure 1.1(a), a pump system shown in Figure 1.1(b), and a sub-surface water sampler shown in Figure 1.1(c). Chapter 5 details the design of a UAV-based fire-ignition system shown in Figure 1.1(d) for interacting with the environment to ignite prescribed fires.

We now discuss the motivation for these projects and the specific contributions of this thesis.

## 1.1 Water Impact

Monitoring water quality is critical to understanding how and why it changes. Currently, collecting enough information to draw solid conclusions is quite challenging and is a bottleneck to developing effective management plans. Human influence on water systems degrades the water quality and alters ecosystems, which has an economic impact of approximately \$2.2 billion in the US alone [1]. Water quality has a much greater impact than money, however. In 2010, the United Nations Environment Program reported that, “Over half of the world’s hospitals beds are occupied with people suffering from illnesses linked with contaminated water and more people die as a result of polluted water than are killed by all forms of violence including wars” [2]. In addition to man-made pollution in water, there are organic forms of contamination that can degrade water quality. Invasive species, toxic microbes and plant life can significantly degrade water quality. More information provided by more frequent and more spatially dense sampling will yield a better understanding of how water is being affected and how it can be treated. Since one of the main barriers to increasing sampling is the required man-hours, automation and robotic aids can be particularly useful in this area to help increase the productivity of the man-hours available.

## 1.2 Sensing and Sampling

The current methods of collecting water samples include grab sampling which is simply dipping a pitcher off the side of a boat [3], static collection mechanisms [4], Autonomous Surface Vehicles (ASVs), [5], and Autonomous Underwater Vehicles (AUVs) [6]. All of these methods suffer from being either slow, expensive, difficult to deploy or spatially restricted.

Using an Unmanned Aerial Vehicle (UAV) for sample and data collection is advantageous over the previous methods for several reasons. As presented in prior UAV-based water sampling work [7] [8], UAVs are light, fast, have good range, and can be computer controlled for autonomous operation. They are especially useful when there are many disconnected bodies of water or difficult to reach areas because of their ability to fly over and around obstacles and land features. While a useful tool with definite benefits, a UAV-based water sampler does have limitations and unexplored applications. The depth from which samples can be retrieved is limited by the length of tube extending from the UAV and also the type of pump used to transfer water up to the UAV. Additionally, gathering temperature data with the water sampling UAV is a previously unexplored research application. In this work, temperature sensors and a peristaltic pumping mechanism are developed to add functionality to the UAV. The design and testing of an autonomous sub-surface sampling robot, the “Waterbug”, that complements the capabilities of the UAV is also discussed. A paper on the design, testing, and evaluation of the Waterbug is currently under submission.



### 1.3 Prescribed Fire

Lighting prescribed fires to combat wildfires and to improve the health of ecosystems is becoming increasingly common, but combating these wildfires is increasing in cost [9, 10, 11]. The tools used for igniting the prescribed fires, such as hand-tools, chainsaws, drip torches, and flare launchers are outdated and place firefighters on the ground at significant risk.

UAVs are increasingly being used to remotely measure and monitor fires [12, 13, 14], which includes simulations on how to track fire and optimize flight paths in these conditions [15, 16]. Our team has taken the next step by designing a system that actually performs aerial ignitions using an Unmanned Aerial System for Fire Fighting (UAS-FF). Figure 1.2 illustrates the concept of firefighters using the autonomous system to safely drop the delayed ignition spheres to manipulate the fire vectors while keeping the firefighters out of danger.



Figure 1.2: Fire fighters deploy UAVs equipped with fire starting mechanisms from a safe location. The left UAV monitors conditions in an occluded area and the right UAV drops ignition spheres to continue a line of fire.

## 1.4 Contributions

- In this thesis we design, analyze, and test a light-weight peristaltic pump that can be carried by a UAV. The peristaltic pump allows water to be pumped to greater heights and from greater depths while being more resilient to clogging and more sterile than previous work with the water sampling UAV. I was responsible for designing, building, and testing the peristaltic pump. The water sampling UAV was part of previous works by John-Paul Ore and other members of the NIMBUS Lab [7] [8]. Prior to my involvement, the Water Sampler could autonomously collect surface samples up to 12in deep using a miniature impeller pump. The new design has been tested at 3m depth and at a height of over 6m from the water.
- We also design and evaluate different temperature sensors for measuring water temperature. The temperature sensors make it possible for a UAV to quickly collect the data to construct three-dimensional thermal structure maps. We successfully mapped a  $10 \times 10 \times 2.5\text{m}$  area during field trials using one of the temperature sensors. John-Paul Ore was responsible for designing the PCB for the MS5803 pressure/temperature sensor used, I characterized its performance in the lab setting, and we jointly performed the field tests with the assistance of Michaela Chung and Sally Thompson from UC-Berkeley. The data were published in an article titled “Obtaining the Thermal Structure of Lakes from the Air” [17] in *Water*. I was responsible for constructing the thermocouples and the characterization of all the temperature sensors in the lab setting.
- In addition, we develop a sub-surface sampling robot called the Waterbug, which seeks to fill the needs of water sampling that the UAV cannot satisfy.

It is capable of retrieving data and water samples from depths up to 10m and is small and light enough to be deployed and retrieved via UAV. Additionally, an algorithm was developed that allows the Waterbug to achieve neutral buoyancy to monitor a specific point of interest in the water column despite only using uni-directional buoyancy control. The development of this robot resulted in a conference paper titled “The Waterbug Sub-Surface Sampler: Design, Control and Analysis” accepted at the International Conference on Intelligent Robots and Systems 2016 [18]. I was responsible for designing and prototyping the Waterbug. David Anthony worked with me on the first couple revisions and John-Paul Ore allowed me to use the MS5803 PCB for the embedded system running the control software that I wrote. Dave and John-Paul both helped me construct the electronics and trouble-shoot software and communication bugs.

- The UAS-FF is an unmanned aerial system capable of autonomously igniting prescribed fires and has the potential to significantly reduce the danger to firefighters performing interior ignitions for controlled burns. It is small, light, and inexpensive enough that it is accessible to a crew of any size. The system successfully ignited over 150 acres over two field tests. Christian Laney was responsible for designing and populating the PCB. He also did much of the electrical integration with the mechanism. Evan Beachly and Christian Laney designed the software. Christian performed the testing for the early revisions and Evan did so for the later revisions. I was responsible for the design, prototyping and physical tests of the mechanical device as well as for maintaining, fixing and modifying the mechanisms when they required revisions to increase their strength and durability after field tests

exposed weak components.

## 1.5 Thesis Overview

This thesis explores the use of robotics for environmental monitoring and interaction by first looking at related works in the areas of water monitoring, sensors, control theory, robotics, and fire (Chapter 2). Next the design, bench testing, and field testing of a pumping mechanism and various temperature sensors respectively are discussed (Chapter 3). A novel sub-surface sampling robot, the “Waterbug”, is discussed next (Chapter 4). After this, an autonomous aerial system for igniting controlled burns is detailed (Chapter 5). Finally, concluding remarks and an outlook for future work on these projects is given (Chapter 6).

## Chapter 2

# Background and Related Work

This chapter examines five research areas that relate to this work. First, the background of peristaltic pumps and some applications are covered. Next, temperature sensing applications and types of temperature sensors are examined. Sub-surface sampling and data collection methods including manual, static sensors, sensor networks and robots are discussed next. After this, a section on basic control theory lays the groundwork for research presented in Chapter 4. Finally, background and motivation for the autonomous aerial fire ignition system, the UAS-FF, are given.

### 2.1 Peristaltic Pump

The peristaltic pump was first patented in 1881 [19] by Eugene Allen for the purpose of facilitating blood transfusions. Figure 2.1 shows an example of a rotary peristaltic pump. The main components are a rotor in the middle, that is driven by a DC motor in this case. Attached to the rotor are four rollers that squeeze the flexible tube containing the fluid being pumped against the interior

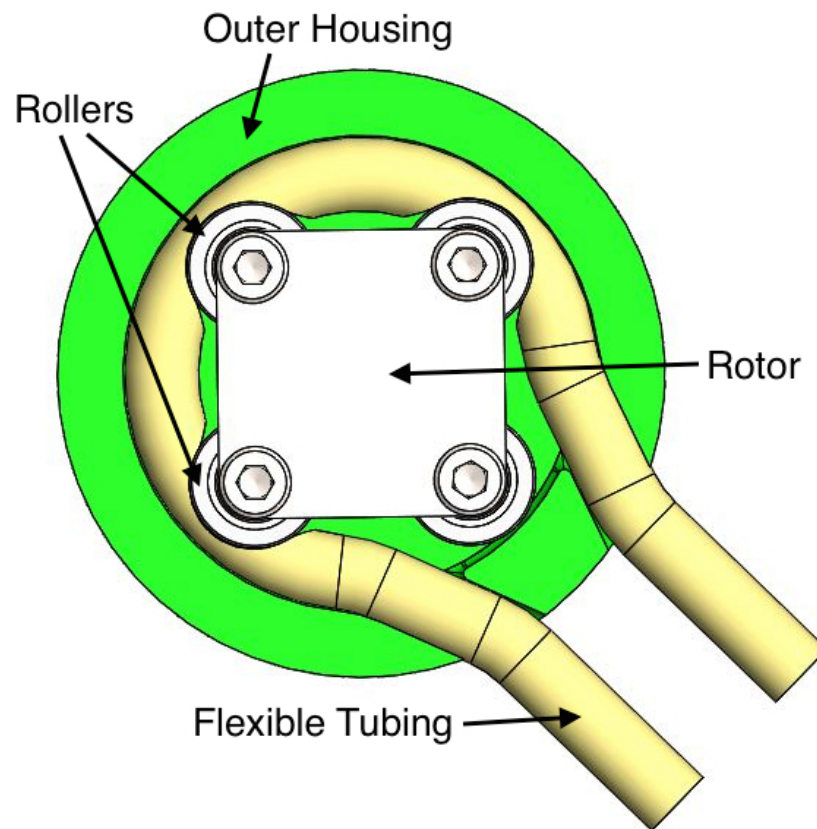


Figure 2.1: Diagram of part of the peristaltic pump designed for UAV-based water sampling

of the outer housing. When the flexible tube is pinched by the rollers against the interior wall, fluid is entrapped between adjacent rollers and carried along between the rollers until the leading roller loses contact as the rotor circumference and tube diverge and the formerly entrapped fluid is forced out the outlet side by the trailing roller. The rotation of the rotor repeats this motion over and over and new fluid is drawn in by the vacuum created by rollers trapping and moving fluid through the tube. Peristaltic pumps are widely used in medical applications for more than just blood transfusions [20, 21, 22, 23]. There are several reasons why this type of pump is advantageous in the realm of medicine. It is very easy to maintain a sterile environment because none of the inner workings of

the pump ever contact the fluid passing through the tube. The pump simply squeezes the exterior of the tube which is a safety benefit and a significant cost savings because the same pump can be used over and over instead of requiring replacement or extensive cleaning between uses. Another key feature is that the precise amount of fluid pumped can be predicted because of the way in which fluid is pumped. The space between the rollers is fixed which means the same amount of fluid is entrapped each time. By utilizing an encoder on the driving motor, the number of revolutions the pump rotor has turned is measurable and subsequently the quantity of entrapped fluid pockets that have been transferred to the outlet of the pump is known. Collecting water samples shares some of the same concerns with the medical world in regards to sterility and protecting against contamination. Using a peristaltic pump in our research helps ensure we prevent contamination from our sampling mechanism. The flexible tubing dipped into the water for collecting samples is inexpensive which allows us to simply swap in a new tube for quick redeployment in the field instead of needing to extensively clean internal mechanisms to prevent contamination of subsequent samples.

Robotic applications of peristaltic pumps tend to be more like bio-mimicry of intestinal or esophageal peristalsis than a rotary pump. A micro-peristaltic pump was designed that used a single actuator to create traveling waves on a polymer membrane to produce a flow rate of 1.5mL/min for a soft robotics application [24]. Other research has explored making robotic models of the swallowing mechanism in humans, which presented interesting challenges in control and trajectory generation [25]. One final robotic application that uses a rotary type peristaltic pump is a cocktail mixing robot called “Bartendro” sold by Party Robotics [26]. Using peristaltic pumps allows Bartendro to mix drinks with sub-milliliter accuracy.

One final property of the peristaltic pump that makes it useful for sampling in water with a high quantity of particulate matter is its resistance to clogging. Because the fluid never contacts the working mechanisms of the peristaltic pump, clogging and wear are minimized which has made it quite popular in applications for moving sludges of all kinds [27], slurry from agriculture and manufacturing [28], powders [29], wastewater [30], abrasive chemicals [31], mining material [32], and fluids containing long polymer chains [33]. Typical impeller or centrifugal pumps have small internal orifices, channels or valves, which clog easily when pumping fluids with high particle content. In addition, the particles in the fluid quickly wear the internal structure of the pump requiring replacement or conversely the moving components of the pump damage the fluid.

The commercial systems we found were not well suited for use on an aerial vehicle. They were either too heavy or had flow rates too low to be useful. Thus, the challenge was designing a system that was light enough, yet had a high enough flow rate and integrated easily with the UAV. Additionally, we designed our pump to allow the tube to be quickly swapped out for fast redeployment in the field.

## 2.2 Temperature Sensing

The thermal structures of an aquatic ecosystem are one of the primary factors in determining the quality of the habitat [34] [35]. The thermal structures also provide the physical forces that drive the macroscopic dynamics including the stability and overturning of the water column, which affects biogeochemistry, oxygen demand, and the ecology as a whole [36, 37, 38, 39, 40, 41]. Typically, bulk thermal properties of surface water bodies are characterized by point measure-



ments taken vertically in the water column. This assumes that the water is well mixed and the conditions are uniform in lateral directions. However, non-uniform properties in the lateral direction of surface water bodies are increasingly being recognized as a driving force behind mixing and habitat development. Examples of this are two alpine rivers in floodplain environments in Italy that have shown lateral temperature variations as large as diurnal variation at any given point [42].

At river and stream confluences, the mixing due to thermal gradients plays a dynamic role [43]. Rivers with cool areas due to tributaries with significantly cooler water than the main channel, bank side shading, deep pools, and groundwater inputs create thermal structure and cold water refuges that are critical for fish habitats [44, 45, 46, 47, 48].

In smaller lakes, variances in depth, bottom sediment, shading, or exposure to wind cause lateral thermal gradients which may be large enough to cause convective currents, contributing to mixing-layer deepening and over-turning dynamics [49, 50, 51, 52, 53].

Clearly, thermal gradients in both the vertical and lateral directions can occur in surface water bodies and they play a critical role in the physical mixing process that determines important water and habitat qualities. Characterizing the non-uniform structures with high spatio-temporal resolution is challenging for researchers who currently use four methods for obtaining data including manual sampling, in-situ sensing, remote sensing, and mobile sensing.

Typically, collecting temperature data manually requires either a boat to transport a researcher or a researcher wading into the shallows. Both of these methods are time consuming, which limits the amount of data they can collect. Additionally, these methods have the potential for disturbing the water and skewing the measurements taken.

In-situ sensors are readily available, capable of continuously reporting data, and require minimal maintenance [54]. These sensors are tied to a line and then anchored in place in the water. They are useful for long-term deployments, but because of their lack of mobility, a dense grid would have to be deployed to capture 3D spatial structures. This would quickly become very costly and could disrupt the normal commercial or recreational use of the water. Further, these sensors tend to have a slow response time (e.g. 15 minutes for the HOBO pendant data logger we tested), so they must be fixed in place for long periods. Recent developments in thermal sensing using fiber optics provide greater spatial continuity in the measurements made. In these measurements, the exponential dependence of the scattering of light on fiber temperature allows travel times for light within a fiber optic cable to be used to infer local temperature variations along the cable length [55]. This technique works well for sampling along the length of a stream but is poorly suited for constructing a three-dimensional grid because of the difficulty of managing many long cables. Cost also remains a constraint for measuring temperature using fiber optic cable.

Remote sensing involves using a manned helicopter [56], fixed-wing aircraft [57], or unmanned aerial vehicle [58] equipped with a thermal camera to collect images of the surface temperature of water bodies. Satellites can also be used to collect data on a much larger scale. Temperatures are typically inferred from the relationship between the intensity of the emitted radiation of a water body, with radiant temperature corrected for emissivity to yield kinetic temperatures. The resulting data sets are quite accurate ( $\pm 1^\circ\text{C}$ ) [56, 59, 60], but their major limitation is that they only report surface temperatures.

Our approach seeks to combine the advantages from other techniques into one procedure. We aim to produce the same degree of accuracy as remote sens-

ing techniques while also producing high resolution data sets of the entire 3D structure instead of just the surface. In addition, the data sets should be collected quickly to allow large scale operation over short periods.

Mobile sensing combines the utility of in-situ sensors for high resolution with the ability to autonomously move in three-dimensional space. These Autonomous Surface Vehicles (ASVs) and Autonomous Underwater Vehicles (AUVs) are increasingly being used to construct thermal maps [61, 62, 63, 64, 65]. These systems can autonomously collect high resolution spatio-temporal data in 3D over long periods of time. However, they are best suited for large, open bodies of water with easy access because they can be difficult to deploy without a boat ramp or dock. They typically don't employ extensive obstacle avoidance capabilities, which limits their utility in shallow water with vegetation. Additionally, GPS and radio communication is limited underwater, so geo-referencing the data collected is difficult and expensive for AUVs.

The system created by Zhang et. al. [65] resembles a robotic fish that glides through the water via either buoyancy driven gliding or fin-actuated swimming. A significant amount of effort was put into designing a robust controller that efficiently achieved descending, ascending, and spiraling motions to best monitor the environment. The methods of motion combine high efficiency with maneuverability, however, the maximum velocity achievable is less than 0.5m/s. The high efficiency and low speed makes it ideal for long missions that gather very high resolution data. With this type of system, it would be impossible to quickly create thermal maps of water bodies simply because it cannot move fast enough.

## 2.3 Sub-Surface Sampling

Both the wireless sensor networking and robotics communities have a large body of research dedicated to underwater operation. To date, most work has considered either static sensor networks, or fully autonomous robots for monitoring water bodies. Our work combines advantages from both of these communities to create new, more effective environmental monitoring tools.

Underwater sensor networks have a multitude of uses, including seismic monitoring, pollution detection, and environmental monitoring [66]. Most underwater sensor networks are assumed to be sparse, statically deployed networks that use expensive acoustic modems for communication [66, 67, 68]. Optical links for underwater communications have also been considered [69]. Traditional wireless sensor network (WSN) ideas guide these designs, which rely on many small nodes to generate and route sensor information to centralized sinks. Traditional WSNs assume that the nodes must be low cost and complexity, which reduces manufacturing and maintenance costs. The threat of water intrusion in marine environments makes this a difficult goal to achieve.

Anchoring nodes to the seafloor with a winch allows nodes to travel vertically in the water [70, 71]. This mobility allows the nodes to find areas of interest within the water column. These nodes are expensive, and the winching mechanism consumes significant energy, which limits the deployment time and how much information is collected.

Small “drifter” nodes that float with the current of tides or rivers have been successfully deployed in the environment to take Lagrangian measurements of current. They are constrained to the surface of the water, both because they lack the actuation or buoyancy control to dive and also because their communication

methods require an antenna that extends above the surface [72, 73, 74]. Other drifting and gliding nodes capable of descending and ascending are used to take sub-surface measurements but are more complex and expensive [75, 76].

The Waterbug, designed as part of this thesis, combines many of the capabilities of the vertically mobile nodes and the drifting nodes while adding some improvements. It has the ability to ascend and descend efficiently and to drift while still being simple and inexpensive.

Aquatic robots have also been used as mobile sensing platforms to study water bodies [77, 78, 79, 80, 81]. The autonomy of these robots and collaboration between them potentially resolves the difficulties of using communication between static sensor nodes. However, these robots are large, expensive, and difficult to deploy. These shortcomings are especially evident when working with multiple small, disconnected water bodies. In these environments it is highly desirable to avoid redeploying robots, and the number of water bodies makes it impractical to dedicate a robot for every lake and pond [8]. Using small UAVs in these areas is attractive, because the high mobility allows a large area to be monitored with a small number of robots. The drawback to using UAVs is that it is extremely difficult to interact with the water, which limits the utility of their sensor data.

The high attenuation of water in both the radio and optical domains forces sparse underwater networks to use acoustic modems, which have the range to link medium to long range nodes. However, acoustic modems are extremely expensive and have low channel capacities, which further increases costs, and limits how much information is collected [82, 83, 84, 85]. Optical links for transmitting information are extremely short range ( $<10\text{m}$ ), and use high power LEDs that consume significant energy [69]. The cost, complexity, and size of these communication devices were significant influencing factors in our decision to design

the Waterbug to not require external communication capabilities while deployed underwater.

Engineers and researchers at the Monterey Bay Aquarium Research Institute (MBARI) created a water sampling module to add to their existing 6.4m long autonomous underwater vehicle (AUV), which they presented in an article by L. Bird, A. Sherman, and J. Ryan in 2007 [86]. The water sampler had several functional requirements that were contrived by a team of engineers and scientists. They were interested in sampling within thin layers of the water column and also detecting sparse microbial populations which drove the decision to require a relatively large collection volume of 2L collected over only 2s. These two requirements for the design led to the nickname “the Gulper”. Several other requirements such as having clear sample collection chambers, depth of operation, and number of sample chambers were driven by requirements specific to the interests of the particular users at the MBARI.

The sample collecting mechanism of the Gulper operates much like a large syringe driven by spring force. Some of the challenges encountered were machining parts to tight enough tolerances and finding proper O-rings to achieve a leak-free seal while avoiding high drag forces while actuating the sampler. Additionally, finding a spring that exerted the required force to actuate the sampler while being safe to set by hand and having the capability to fit inside the space envelope available proved challenging as well. After some experimentation, a custom machined polycarbonate cylinder, quad O-ring, and dual extension springs were chosen to solve the previously mentioned challenges. Both lab tests and field tests were carried out and compared to standards to validate the performance of the Gulper. The samples collected during field tests were compared to samples collected using more traditional techniques and the results were highly correlated. The team

at MBARI concluded after several successful missions that using mechanisms like the Gulper, “for coupling rapid, large-volume water sampling with the autonomy of an AUV will provide a better observational platform for diverse research areas in oceanography.”

The Waterbug shares some functional similarities with the Gulper. It also uses a syringe mechanism for quickly collecting samples which allows it to sample within thin layers of the water column. Both autonomous water sampling platforms have the potential to provide a better observational platform in their own domain. The Waterbug is much smaller and is more suited to blanket deployment for wider spread observation than the point sampling the Gulper provides.

Small UAVs have been used to collect water samples from freshwater bodies as part of previous work in the NIMBUS Lab [8, 7, 87]. This UAV pumps water from near the surface of a water body to a reservoir in the UAV. The water samples are brought back to laboratories for detailed analysis. The small payload capacity and control complexities limit this approach to collecting small water samples from near the water’s surface. The weight and complexity of a long tube make it impractical to collect water samples from deeper than a meter or two below the surface with a UAV. The Waterbug provides a good complement to the capabilities of the water sampling UAV. It is light enough to be deployed and retrieved by UAV but it has the capability to sample from deeper than the UAV alone can reach, and it can loiter in the water longer than the UAV can hover to observe the environment.

## 2.4 Control Theory

Three aspects of control theory are particularly relevant to the Waterbug and are used in the design of the algorithm to achieve neutral buoyancy. A brief overview of feed-forward, feedback, and precompensation, as well as some supporting aspects of control theory are given in this section [88, 89]. Open-loop control repre-

### Open Loop Control

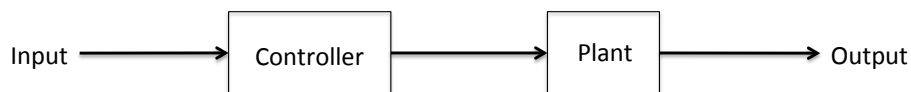


Figure 2.2: Block diagram of open loop control

sented by the block diagram in Figure 2.2 is one of the simplest forms of control. The plant is the process or mechanism being controlled, the input is the directive signal, the controller translates the input signal into a relevant form for the plant and the output is the plant's response. This type of control is relatively inexpensive and easy because it requires neither a system model nor any additional equipment to monitor the output of the plant. However, these advantages are also the disadvantages of the system. Without a system model the controller cannot make predictions about the output of the plant based on the input it gives and without feedback, the controller has no knowledge of disturbance in the system and therefore cannot account for it.

Feedback control is a type of closed loop control and is represented in Figure 2.3. It improves upon open loop control by adding the ability to account for disturbance in the system. The lower block takes the output of the plant, multi-



plies it by a gain  $H$  and feeds this signal back to the controller so that the plant is given a composite input commonly called the error signal that is made up of the input signal and the plant output. In an ideal world, the input signal would specify a plant condition and the plant would respond perfectly with no disturbance so that the output of the plant exactly matches the input signal. The feedback signal would exactly cancel the input signal to the controller and no additional input would be given to the plant because its desired output is already achieved. However, when disturbance is injected at any point in the system, the feedback and the input signal are not exactly matched and the controller translates this error signal into a plant input.

### Closed Loop Feedback Control

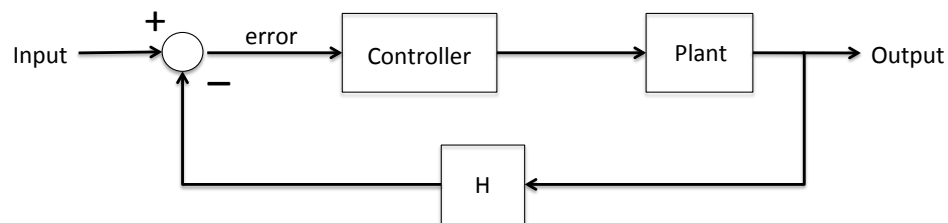


Figure 2.3: Block diagram of feedback control

Feedback control is not dependent on an accurate system model. By tuning the gains of the controller and feedback, the plant input can be scaled to an appropriate level so as to achieve stability in most situations. However, one situation where it is difficult to achieve stability with feedback control is when there is significant delay in the system or the dynamics of the plant are much much slower than the rate of control input and feedback. In this case, the controller gives the plant an input and then measures its output, which apparently did not respond

at all to the input. This information is fed back to the controller which then gives an even larger input to the plant to try and achieve the desired response. This process can happen over and over with the controller trying harder and harder to achieve the desired plant output when in reality, the plant is simply slow to respond to the input it is given. When the plant does respond, it overshoots the original desired output and often diverges. There is a significant body of work devoted to dealing with delay in feedback control for discrete system time delay [90], multivariable systems [91], PID tuning of controllers for systems with unstable processes [92], PID neural networks [93], an algorithm for stabilization for systems using fractional-order PID controllers [94], and frequency-domain design of PID controllers for stable and unstable systems [95]. The vast and varied approaches for attempting to achieve system stability using only feedback in systems with delay is a testament to the utility of not requiring a system model. However, developing a system model is the best approach for achieving stability in certain circumstances, despite its challenging nature.

Feed-forward control is a technique that takes advantage of a system model. It looks similar to simple open-loop control, but the controller has knowledge of the system model for the plant so it is capable of predicting the output based on its input to the plant, unlike simple open-loop control. It does not require tuning gains to achieve the desired output like feedback control. The major advantage of feed-forward control is due to its knowledge of how the system will respond to a given control input. Delay does not present the challenges that it does for feedback control, because even if the plant takes a significant amount of time to respond to the controller input, the system model can predict what the response will eventually be instead of continually making corrections based on measured error in the output. Pure feed-forward control does have the disadvantage of

not correcting for disturbances injected into the system. Also, if the model is inaccurate, the actual response will differ from the predicted response. In practice, using feed-forward allows the system itself to be less expensive, smaller, lighter, and use less energy. The reason behind this is because the model of the system allows the controller to put in only the control needed to achieve the desired output instead of having to potentially correct for large errors or overshoots.

Precompensation is a control technique used to scale the reference input to a system to an appropriate level to eliminate steady-state error. It bears similarity to feed-forward control because it requires some knowledge of the system and it does not handle disturbance because it is outside of feedback loops. Nevertheless, precompensation is a useful tool in the right circumstances.

## 2.5 Fire

Prescribed fires can reduce wildfire severity [96, 97, 98, 9], control invasive species [99, 100, 101], and improve rangelands for livestock and grazing [102]. However, igniting and containing the fire also puts ground crews at risk of injury or death. Firefighters igniting the interior of a burn unit are surrounded by unburned fuel, and a drip torch, the tool of choice for interior ignition, starts the fire dangerously close to the crew. Changes in wind can smother the personnel in smoke and transform a slow backburn into a fast-moving blaze, leaving little time to escape or deploy a fire shelter [103]. The problem is compounded if the burn unit is in difficult terrain. The firefighter could become injured during ingress or egress and unable to get themselves out of danger, and rescue would be difficult because of the terrain. In a conversation with a member of the National Parks Service who directs the Homestead National Monument, we were informed that



Figure 2.4: Interior ignition being conducted from an ATV

five firefighters were killed last year in these types of situations. Burning large acreages introduces additional difficulties. The fire line may be miles long and require personnel to enter ravines, or other difficult-to-escape terrain. In these cases, interior ignition is typically conducted using drip torches mounted on All-Terrain-Vehicles (see Figure 2.4). This introduces additional risks, as ATVs are prone to roll over. One firefighter died at a prescribed burn when he was pinned under his ATV after it overturned [104]. Eliminating the need to send a crew member on the ground into the middle of the fuel of the burn unit would significantly reduce the risk to personnel.

Aerial ignition removes the need to have personnel inside the burn area. The Premo Plastic Sphere Dispenser (PSD) [105] is a mechanism designed to be mounted on a helicopter that uses ignition spheres to ignite prescribed fires. It has the capacity to hold 450 spheres which it can drop at variable rate of 45 - 130 spheres per minute. Fully loaded the device weighs nearly 100lbs. These helicopter-mounted ignition systems [106] are too expensive for most private

landowners [107], and introduce the risk of crashing [108].

Additionally, there are ground based launchers that use the same type of ignition spheres [109, 110]. They have the capability to launch the spheres between 20 - 100m. Both types of launchers must be manually cocked, aimed, and fired for each sphere sent downrange. In conversations with the practitioners who use these types of tools, we were informed that they jam often and require extensive cleaning to remain operable and as a result, these practitioners rarely use them.

Firefighters need new tools that reduce risk, yet are low cost and easy to operate, to make them available to the majority of prescribed fire users.

Two different types of ignition spheres already exist for use in the PSD and ground based launchers, one produced by SEI Industries [111] and the other produced by Aerostat, Inc [112]. Both types contain approximately 3g of potassium permanganate and are manufactured to withstand high impact, which ensures the spheres stay intact when dropped from altitude, but it also means up to 115N is required to puncture the wall of the sphere. We used these spheres in our work because they are widely accepted in the firefighting domain and they are already mass produced.

One of the significant challenges we faced was designing a mechanism that could provide and withstand the force necessary to puncture the ball while remaining under the size and weight limitations. Our system takes the capabilities of the helicopter based system, shrinks it down to less than 500g, automates its function and provides a much higher accuracy than the ground-based launchers, while keeping personnel out of danger.

## Chapter 3

# UAV Sensing and Sampling

This chapter details the requirements (Section 3.2.1), design (Section 3.2.2), characterization (Section 3.2.3), and field testing (Section 3.2.4) of a peristaltic pump with the capability of pumping water samples to over 6m in altitude. It was designed for use on a UAV, and the length of tubing that can safely be flown by the UAV is the limiting factor for sample depth and height instead of the pump performance.

The next portion of the chapter discusses the motivation and requirements for a temperature sensor used on a UAV to provide mobile sensing in order to create three-dimensional thermal structure maps of water bodies (Section 3.3.1). The lab bench tests (Section 3.3.2) and field tests are subsequently discussed (Section 3.3.3).

### 3.1 UAV Platform

Before getting into details about the sensors and mechanisms designed to be mounted on the UAV, we will first give a few details about the UAV platform

used.

The aerial platform we chose to use for both the peristaltic pump and temperature sensors is an Ascending Technologies Firefly model. The Firefly is a hexacopter with a maximum payload of 600g [113], shown in Figure 3.1.



Figure 3.1: Ascending Technologies Firefly

It comes equipped with GPS (Global Positioning System), 3-axis accelerometers and gyroscopes, compass and an air pressure sensor.

The UAV is powered by a 3-cell 5000mAh lithium polymer battery. The battery ranges from 12.6V when fully charged to 10.5V when discharged. In addition, the UAV has an onboard 5V regulator and a power port where a separate regulator can be plugged in for other desired voltage outputs.

With a fully charged battery, the vehicle can fly for 15-20 minutes, which bounds the maximum mission distance at approximately 2km.

We chose this UAV because it is portable, certified by European aerial vehicle safety standards, includes extensively-tested control software, has enough payload capacity to carry the mechanism we designed, and in case of motor failure can still fly with only five of six motors functioning.

The Firefly navigates using a built-in GPS circuit and an air pressure altimeter. We utilize the GPS for navigation outdoors, as well as determining the location from which samples and data are collected.

The Firefly has configurable mounting points where a payload can be attached and plenty of space and height clearance to mount mechanisms beneath it. We

discovered that most often, the maximum payload weight was the limiting factor rather than the space available.

## 3.2 UAV Sensing and Sampling: Pumps

The design requirements for a peristaltic pump to be mounted on a UAV are given in Section 3.2.2, followed by the final design details (Section 3.2.2), characterization (Section 3.2.3), and field testing (Section 3.2.4).

### 3.2.1 Pump Requirements

**Weight:** As mentioned in Section 3.1, the maximum payload for the UAV is 600g, so the pump, tubing and any other peripherals had to remain under this limit, and the heavier the pump is, the shorter the vehicle flight time.

**Flow Rate:** Ideally, the pumping rate should be as high as possible but it is largely dependent on the size and power of motor used to drive the pump. Since the UAV platform has both weight capacity and power restrictions, we tried to find the most efficient combination of weight, power consumption, and pumping rate.

**Power Requirements:** As mentioned, the UAV has power restrictions and adding a separate power source consumes a significant portion of the payload, so we decided that the pump needed be powered directly from the UAV. The motor driving the pump needs to remain under the voltage and current limits of the auxiliary power supplies onboard. 5V is readily available on the UAV and any voltage under 10V is easy to achieve with a lightweight regulator.

**Head:** Head refers to the height of a column of water a pump can produce. The pump needs to be able to produce at least 1m of head. One property of the



peristaltic pump that is particularly useful for UAV-based water sample collection is a result of the vacuum pressure created by the roller pinching the flexible tube, which allows the pump to produce a significant amount of head. If the rollers of the peristaltic pump completely occlude the flexible tube so it is fully sealed, the maximum head the pump can produce is just over 10m, assuming standard atmospheric conditions, so this requirement was easily exceeded.

### 3.2.2 Pump Design

While the concept of using a peristaltic pump for pumping water is not unique, we did custom tailor a peristaltic pump we designed to fit the electrical capabilities, weight and size restrictions, and tubing used on the NIMBUS Lab's water sampling UAV. Figure 3.2 shows one of the final designs used in the UAV water sampling experiments. The driving motor for this version is a 50:1 ratio Pololu Micro-Metal Gearmotor rated to run at 6V with an output shaft no-load speed of 625RPM [114]. The other design was nearly identical except it used a larger Pololu gearmotor with 9.7:1 ratio, rated to run at 6V with an output shaft no-load speed of 990RPM [115]. The black tube retainer was a design feature added after experiments demonstrated that in practice, the tube tended to slowly slip around the circumference of the rotor in the direction of rotor rotation unless it was held in place. The tube is press fit into the groove running around the circumference of the the retainer and the friction from the press fit holds the tube in place. The open design of the pump makes changing tubes easy and very quick. Replacing a tube is as simple as slipping the old tube out and pressing the new tube in. The roller bearings compress the the tube against the inner wall of the outer housing but the tube used is quite flexible so only a small amount of force is needed to

squeeze it in place. After this, the tube retainer is snapped in place around the outer housing and the inlet side of the tube is pressed into the groove on the retainer.

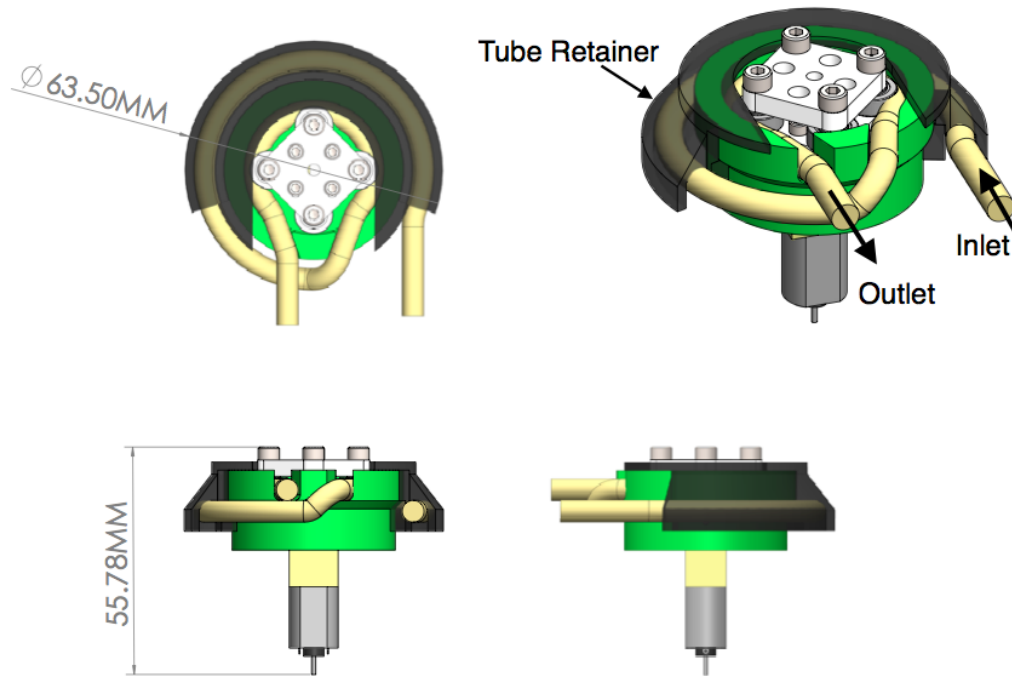


Figure 3.2: Final peristaltic pump design with small motor

In previous works, we used a TCS Micropump [116] to pump water up to the UAV. This pump weighs 10g and has an input voltage range of 2V to 4V. It uses an internal impeller driven by a small brushed DC motor and is capable of producing slightly more than 1m of head. Because it uses an internal impeller as its pumping mechanism, it must be primed in order to start pumping water. This means that in a UAV-based water sampling mechanism that it must be mounted at the bottom of the tube that runs up to the UAV and be submerged in the water while pumping. This pump is quite small and light weight but it requires running wires down the length of the tube to power it. It also requires an external filter to prevent clogging of the impeller mechanism. Using too fine of a filter

mesh restricts flow and reduces head, so a larger filter orifice is required, which occasionally results in the pump becoming clogged, though not as often as with no filter in place. Some of our research collaborators have expressed concern over contamination caused by the water touching the inside of this type of pump, so if there are experiments or sample collections that have strict contamination requirements, the pump and associated peripherals that come in contact with the water must be extensively cleaned.

### **3.2.3 Pump Bench Tests**

The peristaltic pumps were tested at 5V and 9V at five different altitudes between 1m and 3m to characterize and compare their performance. 1m was chosen as the lower bound, because in practice, we will not fly closer than this to the surface of the water and 3m was chosen as the upper bound because we will not fly with more than about 4m of tube hanging from the vehicle which allows the vehicle to fly 3m above the surface with the tube submerged up to a meter deep.

For each lab trial, the end of the tube connected to the pump was submerged in a bucket of water, which was placed on a flight of stairs. The pump was powered by a variable voltage power supply and emptied into a container sitting on a scale. The pump was allowed to prime and then a one minute timer was started when water began flowing out of the pump. The current draw as reported by the power supply was approximately constant and was recorded for later calculations. After one minute, the pump was stopped and the mass of water pumped was measured and the density of water was used to convert the mass to a volumetric measurement. The efficiency for each trial was calculated by dividing the energy consumed over the one minute and dividing the volume pumped by the energy

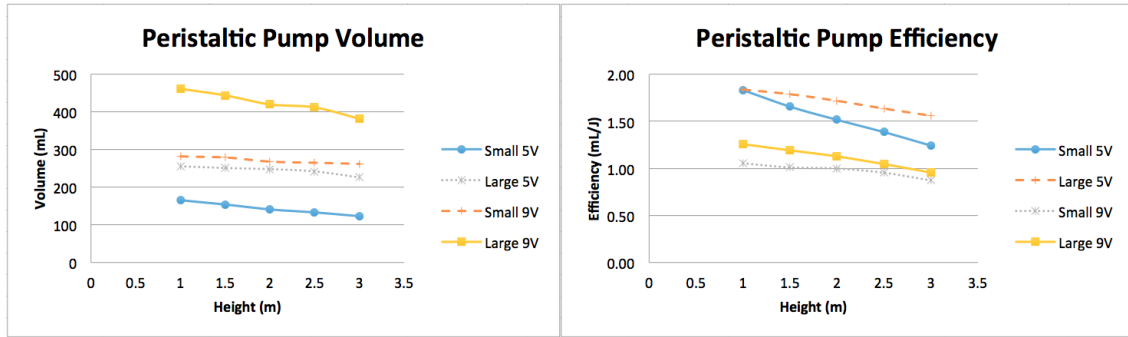


Figure 3.3: Peristaltic pump characterization and performance for different voltages and altitudes

consumed. Figure 3.3 shows the volume pumped and also the efficiency.

The pump with the larger motor pumped more volume and consumed more energy, as expected, but it also was more efficient than the pump with the smaller motor. Both pumps had decreased efficiency at higher voltage. The efficiency for both pumps also decreased at higher altitudes because of the larger amount of energy required to produce greater head. The pump with the larger motor weighs 130g and the pump with the smaller motor weighs 48g. On an Ascending Technologies Firefly hexacopter UAV, an additional 12W of power is required to hover when carrying the peristaltic pump with the large motor compared to the small motor. However, just the UAV alone requires around 200W to hover, so when considering the energy requirements to fly the UAV, the peristaltic pump with the larger motor is almost twice as efficient because of its higher pumping rate, even when considering that it is heavier and consumes more energy and can therefore shorten flight time. Table 3.1 summarizes the results of the power required to run the pumps at 9V and 2m height, as well as for the UAV to fly with the pump mounted on it. The flight time was computed assuming a 4900mAh battery with a nominal voltage of 12V. The efficiency shown is the volume pumped divided by the total energy consumed over the flight time by both the UAV and

Table 3.1: Summary of the power required to fly with the two peristaltic pumps and the overall efficiency

	Flight Power (W)	Pump Power (W)	Combined (W)	Flight Time (min)	Volume (mL)	Efficiency (mL/J)
Small Pump	216	4.14	220.14	14.8	3675	0.0174
Large Pump	228	6.21	234.21	13.9	5838	0.0276

pump.

The TCS Micropump was previously characterized by John-Paul Ore as part of earlier research with the water sampling UAV [117]. It is somewhat difficult to compare the performance of the Micropump to the peristaltic pumps because they run at different voltage ranges and the Micropump cannot pump the water nearly as high as the peristaltic pumps. Ore tested the pump at various voltage ranges and altitudes and found that the flow rate of the Micropump drops off very quickly after 1m when operating at the recommended voltage and stops pumping completely around 1.2m, even when operating slightly above the recommended voltage. Table 3.2 compares the performance of the three different pumps at 1m. As mentioned earlier, 1m is the closest the vehicle will come to the water so we didn't test the peristaltic pumps below this altitude. However, the Micropump was unable to pump any higher than 1m so we compared the three pumps at this altitude and then continued increasing altitude with the two peristaltic pumps to compare their performance just against each other.

Table 3.2: Comparison of the three pumps at 1m altitude

Micropump	Voltage: 3.5V				
	Height (m)	Current (A)	Energy (J)	Efficiency (mL/J)	Volume (mL)
	1	0.25	52.5	5.71	300
Small Peristaltic Pump	Voltage: 5V				
	Height (m)	Current (A)	Energy (J)	Efficiency (mL/J)	Volume (mL)
	1	0.3	90	1.83	165
Large Peristaltic Pump	Voltage: 5V				
	Height (m)	Current (A)	Energy (J)	Efficiency (mL/J)	Volume (mL)
	1	0.51	153	1.84	281

The Micropump has the highest efficiency and flow rate at 1m altitude for the given voltage. However, in practice, flying only 1m from the surface of the water can be dangerous for the vehicle and gives the backup pilot very little time to react in case of an emergency. Additionally, the impeller of the Micropump can clog in dirty water or when sampling near the bottom which requires disassembling the pump in the field and possibly losing the small internal pieces.

Even though our initial specification stated that we will not exceed a pumping height of 3m, we attempted to characterize the maximum height the peristaltic pump design could achieve. In theory, the pump should be able to achieve over 10m of head. In practice we found that at just over 6m, the pump still functioned well, but when priming, the tube began to collapse under the vacuum created by the pump. We considered this the maximum height since one of the benefits of the pump is that it is self-priming, and even though the pump could have pumped higher if it was pre-primed, this eliminates part of its functionality.

Both the peristaltic pumps and the Micropump have their respective benefits and drawbacks, so they will both likely continue to be used alternately when their individual strengths are of greater value.

### **3.2.4 Pump Field Tests**

The peristaltic pump design, shown mounted on the UAV in Figure 3.4, was tested on August 12th, 2015 at a lake near Offutt Air Force Base near Omaha, NE. The purpose of the test was to search for baby Zebra Mussels (veligers) by pumping water up to the UAV with the peristaltic pump and filtering the water through a 64 micron filter [118]. The lake is known to be infested with Zebra mussels and our water science collaborators informed us that summer is the most likely time

to find veligers.

For our tests, we flew approximately 1.5m above the water and powered the pumps from 9V, so we assume the flow rate was 251ml/min for the small and 444mL/min for the large peristaltic pump based on data from our bench tests. We tested both pumps to evaluate their performance in the field. The depth of the inlet of the tube was controlled by designing a 3D printed press-fit clamp and attaching a fishing bobber to it, shown in Figure 3.5(a). The tube ran from the water up to the peristaltic pump on the UAV.

At the outlet of the tube on the outlet side of the pump, the water was filtered by the 64 micron filter before dropping back into the lake. The filter was wrapped around a 3D printed cage that had internal threads designed into it. A 3D printed adapter with external threads was affixed to the outlet of the tube to allow the filter to quickly be replaced between flights. Figure 3.5(b) shows one filter threaded on the adapter, a spare filter, and a quarter-dollar coin for reference.

The locations we sampled were near the shore where concrete chunks had been dumped into the lake. Our ecologist and water science collaborators told us that the veligers breed there and then eventually attach to the rocks or concrete as they grow. We sampled in several locations that formed a line starting 5ft out from the shore until the water depth was greater than 15ft. The thick black lines in Figure 3.6 show the sample locations on a depth map of the lake. Since the test was for evaluation purposes, we measured the depth of the sampling locations by

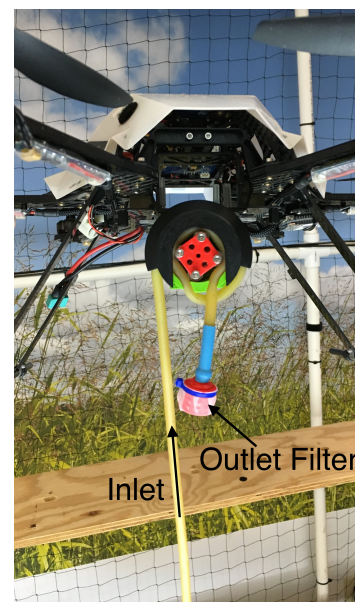
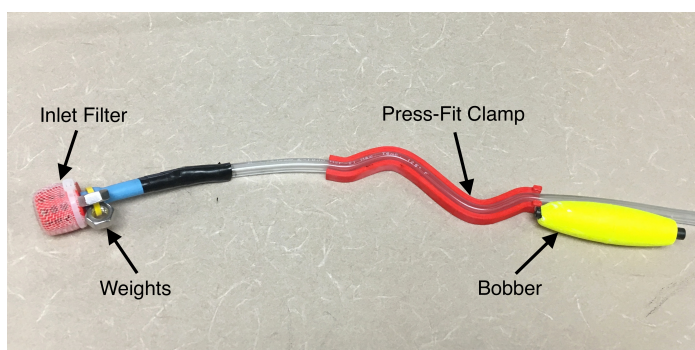
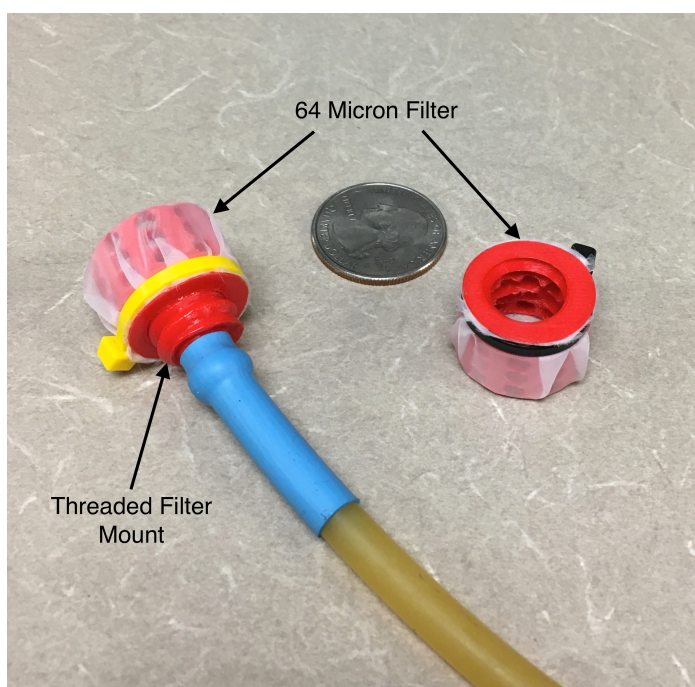


Figure 3.4: Peristaltic pump mounted on Astec Firefly





(a)



(b)

Figure 3.5: (a) Inlet side of tube and clamp/bobber float for controlling depth of sampling (b) Outlet side of tube with 64 micron filter and threaded adapter

hand so that we could set the fishing bobber at the correct location on the tube so that the end rested right at the depth of the concrete chunks. For completeness, we also took samples from higher in the water column. We flew from the bank of the lake over the sampling location, and lowered the tube into the water by descending the vehicle until the bobber was floating in the water. The pump



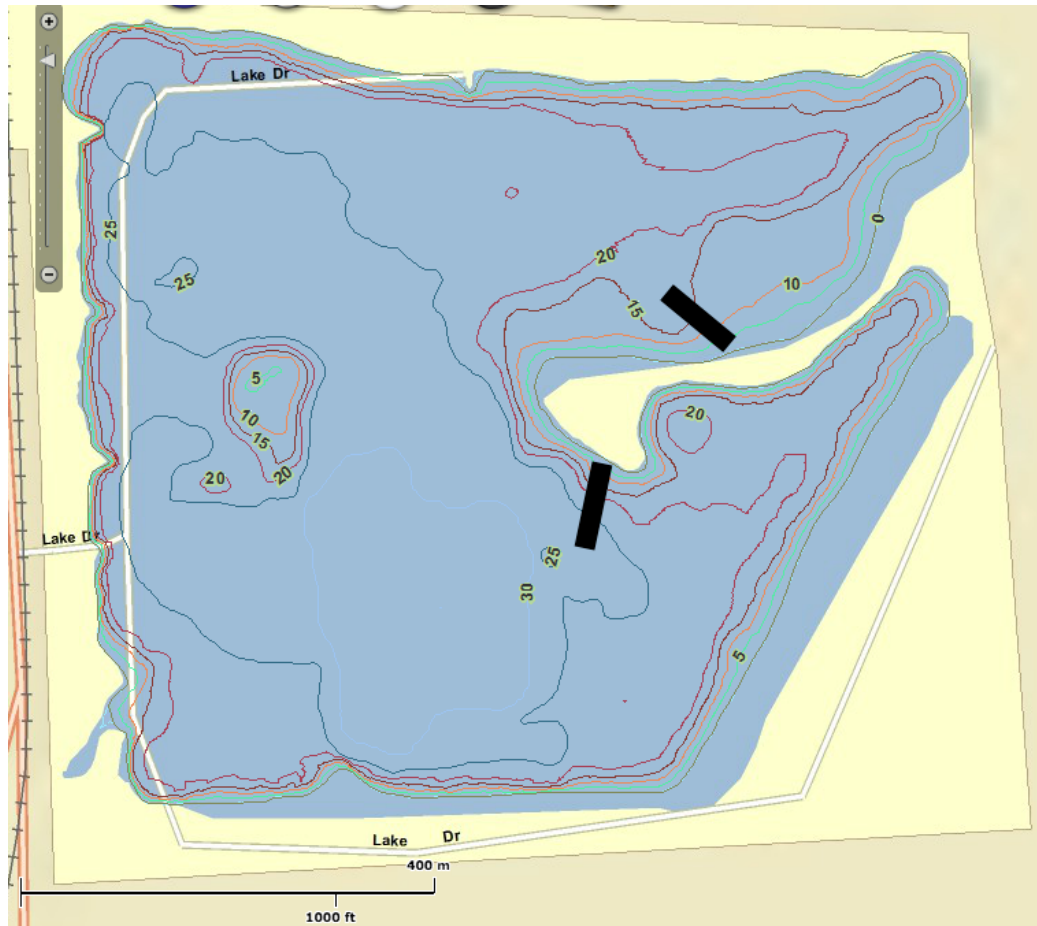


Figure 3.6: The black lines show the locations sampled for Zebra mussel veligers.

ran continually once powered, so water began running through the filter as soon as the tube was in the water and we continued to loiter the UAV at the sample location until the battery was depleted approximately 12min later, at which point, we flew back to shore. Loitering for 12min resulted in approximately 3.01L being pumped through the filter by the small peristaltic pump and 5.33L by the large peristaltic pump. After landing, we collected the used filter from the vehicle and immediately placed it in a sterile vial to be examined for veligers in a laboratory later. As a control, the traditional method of a researcher in waders casting a net and dragging it through the shallows was also employed to collect samples. The

net dragging typically filters around 60L of water per cast.

After all the sample filters were examined in a lab, it was determined that the veliger distribution was very sparse at the time of sampling. In June of 2015, the average density of veligers was nearly 200 specimens per test but by August, the average density had dropped to less than one specimen per test. As a consequence, no veligers were found in the filters used with either the large or small peristaltic pump. The conclusion was reached that the population was mostly dormant and sampling at a different time when the activity was higher may have yielded different results. Unfortunately, this did not allow us to make any determinations about what minimum flow rate is required to detect veligers. Future tests slated for summer of 2016 will hopefully help to make this determination.

The pump itself performed satisfactorily and we feel confident that it worked as designed. The filter at the inlet end of the tube that was near the bottom of the lake filtered out large particles, and even though it became partially clogged with debris, the peristaltic pump created enough head to continue pumping water with no discernible drop in the flow rate. After an hour of almost continuous operation, the portion of tube that was pinched by the rollers smelled warm and was visibly abraded on the surface, but this had no noticeable impact on the performance.

On June 9th, 2016, the field test was repeated to once again search for veligers. The flying conditions were less than ideal, with windspeeds exceeding 10m/s, so we only tested the large peristaltic pump to provide the best chance of capturing the specimens during the limited amount of flights we attempted. This time, the veliger activity was much higher and the UAV successfully captured veligers in its filter. Figure 3.7 shows the veligers captured in the sampling filter during one of the flights. Capturing the veligers in detectable quantities was a significant success for the peristaltic pump and UAV sampling techniques. It proved that the

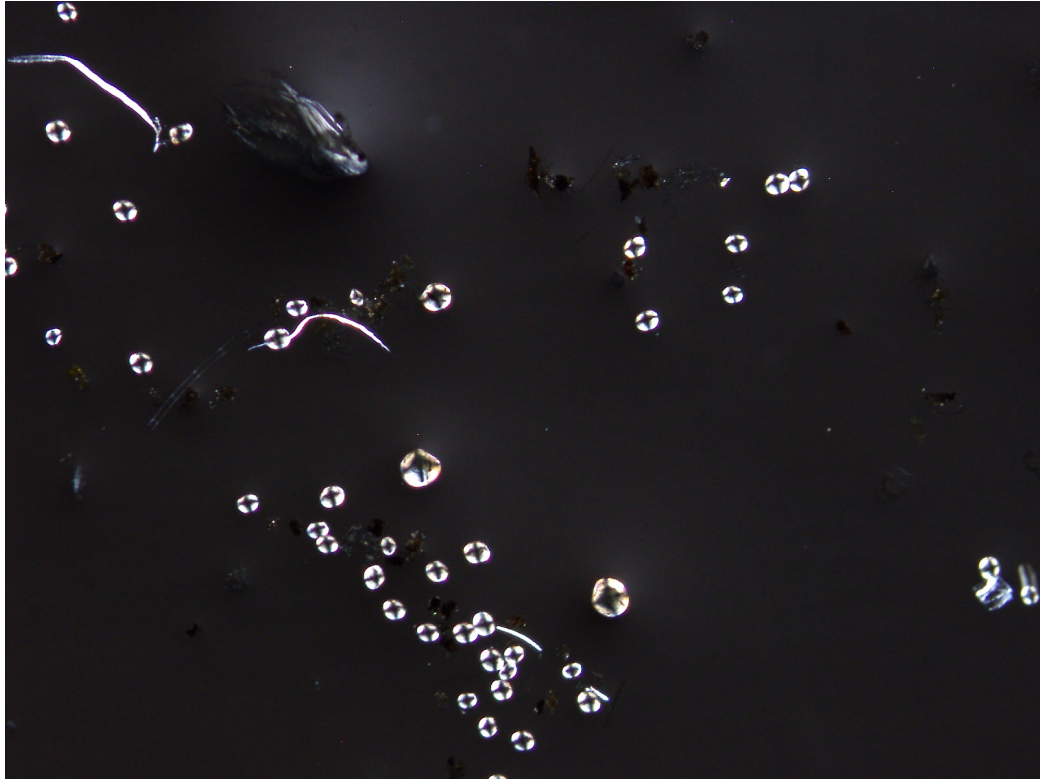


Figure 3.7: Zebra mussel veligers captured by the UAV water filtering system

system is a viable tool for this application and future work will look at how the advantages of a UAV, such as precision sampling and mobility can be leveraged to make invasive species management more effective.

### 3.2.5 Pump Summary and Contributions

In summary, we designed two versions of a peristaltic pump and compared it to a Micropump with an impeller that has been used in some of our earlier work. We overcame the challenges of designing a pump that was light enough for the UAV, while still providing a high enough flow rate and remaining within the power limitations available. Through lab testing, we characterized the pumps' efficiencies at various heights and operating voltages and determined the maxi-

mum functional pumping height for our particular setup is just over 6m. We field tested the pump in an experiment looking for Zebra mussel veligers, and while none were found due to a dormant population at the time of testing, we were satisfied that the pump performed as intended.

I was responsible for designing, prototyping and characterizing the peristaltic pumps and John-Paul Ore assisted me with the field tests.

### 3.3 UAV Sensing and Sampling: Temperature

#### Sensors

In addition to our UAV-based sampling work with the peristaltic pumps presented in Section 3.2, we introduce our work with UAV-based mobile sensing of temperature in this section.

#### 3.3.1 Temperature Sensor Motivation and Requirements

Accuracy and an appropriate amount of resolution are, of course required for a sensor used to measure temperature, but we determined that a very close following requirement for a UAV-based temperature sensor is a fast response time for multiple reasons. First, the UAV battery life is limited, which means that spending time hovering while waiting for a sensor to settle limits the amount of points that can be measured before needing to land and change batteries. Second, the UAV attempts to hold altitude, but if the wind is blowing, the vehicle will be buffeted up and down, causing the temperature sensor to change depths. If the water being measured is highly stratified and the sensor is too slow, the stratification will simply be averaged out as the sensor bobs up and down because of the UAV movement. However, the prior two issues can be resolved with a fast enough sensor.

The pressure sensor used to gauge the depth of the temperature sensor is very fast and if the temperature sensor could respond similarly quickly, the stratification of the water could be observed without requiring the temperature sensor to be held stationary. The temperature sensor should have a response time of less than one second to allow high resolution data to be captured faster than

the normal vehicle dynamics of bobbing up and down occur. A sensor this fast could be continuously lowered through the water vertically, dragged horizontally, or a combination of the two motions could be used to quickly build a large 3D temperature map of a water body.

The first sensor we designed and field tested (MS5803), the results of which are detailed in Section 3.3.3, had far too slow of a response time. The testing revealed the importance of having a fast sensor, which lead us to return to the design of a new temperature sensor which we will field test in future trials.

### 3.3.2 Temperature Sensor Bench Tests

The requirements for a UAV-mounted temperature sensor for the purpose of measuring water structures were partially driven by some of our early stage trials. We initially used the integrated temperature sensor on the MS5803 integrated circuit shown in Figure 3.8. Our main use for the MS5803 was to measure depth via pressure, but since it had a temperature sensor built in, it was convenient for a first attempt to use it for temperature measurements. The sensor was compared against a HOBO Pendant logger, which is an in-situ temperature sensor that our water science collaborators use. Table 3.3 gives the specifications for the two sensors.

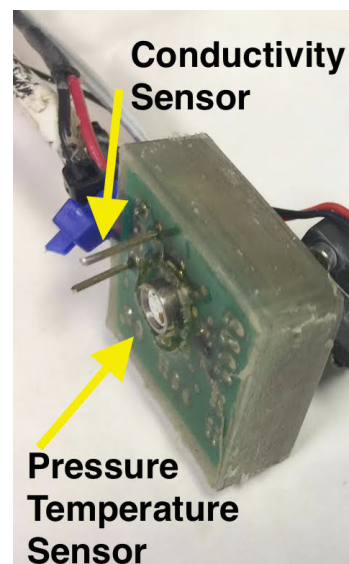


Figure 3.8: MS5803 IC on a custom circuit board

Figure 3.9 shows a plot of the MS5803 temperature sensor and HOBO pendant simultaneously submerged in ice water, then switched to room temperature water, and then plunged back into ice water. The temperature sensor on the MS5803

Table 3.3: Sensor specifications

Sensor	Specifications
In-situ temperature	Hobo Pendant Temperature/Light Data Logger Resolution: 0.14 °C at 25 °C Accuracy: $\pm 0.53$ °C Operating range: $-20$ °C to 50 °C
Pressure-temperature	Measurement Specialties MS5803 sensor Pressure resolution: 0.012 mbar Pressure accuracy: $\pm 2.5$ mbar Temperature resolution: 0.01 °C Water contact detector

compares fairly accurately against the HOBO after a correcting offset of  $-0.3$  °C is applied. Figure 3.9 also shows that the settling time to reach the final temperature is faster than the HOBO, but still quite slow. On average, the temperature sensor on the MS5803 took  $90s \pm 45s$  to converge to 90% of the final temperature and reaching the final temperature took considerably longer. In practice, it's difficult to keep the UAV stationary both vertically and laterally within our desired resolution for this length of time. Additionally, UAVs capable of vertical take off and landing (VTOL) have relatively short flight times, so spending 90s to get one reading is unacceptable.

Thermocouples can have response times that are less than one second [119] which would allow the capture of high spatio-temporal data when used on a UAV. The settling time for a thermocouple is determined by the junction diameter and shielding material and thickness. One other characteristic of a thermocouple that is usually advantageous is their extreme functional range. A K-type thermocouple can measure from 0 °C to 1250 °C. However, the huge range means that achieving high resolution is difficult. The temperature of water we will typically use the UAV temperature sensor to measure only ranges from 0 °C to 30 °C. We were

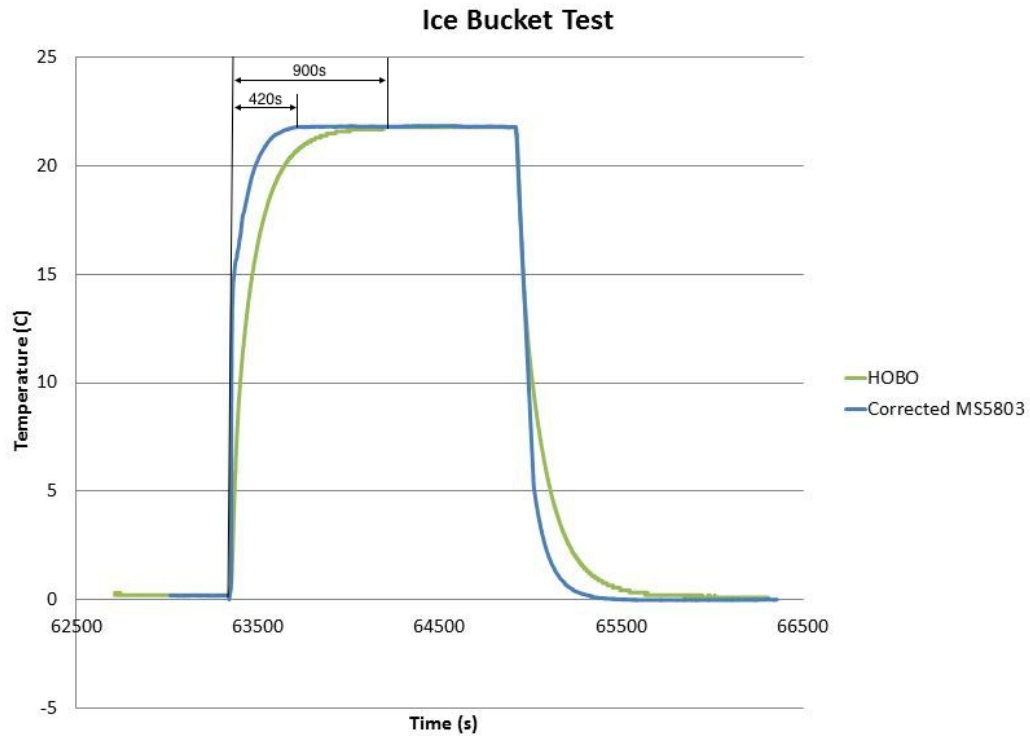


Figure 3.9: Comparison of HOBO and MS5803

unsure if a thermocouple would give high enough resolution for this relatively small range but the possibility of an extremely fast response time made it worth investigation.

Another type of sensor we chose to evaluate was a thermistor. A thermistor works by changing resistance based on temperature. Thermistors have a much smaller functional range but higher resolution and typically longer response time than thermocouples. The particular model of thermistor we selected is a GP103J4F 10k $\Omega$  Thermistor [120]. This sensor is rated for operation from  $-40^{\circ}\text{C}$  to  $300^{\circ}\text{C}$  but its nominal resistance changes from 33K Ohms to 8K Ohms over the range we will experience in the field so it gives good resolution, even when using an inexpensive 10-bit analog-to-digital converter (ADC). The diameter of the thermistor is less than 0.060in which helps keep the response time low. The data sheet states



a specification of 0.35s for one thermal time constant in stirred oil.

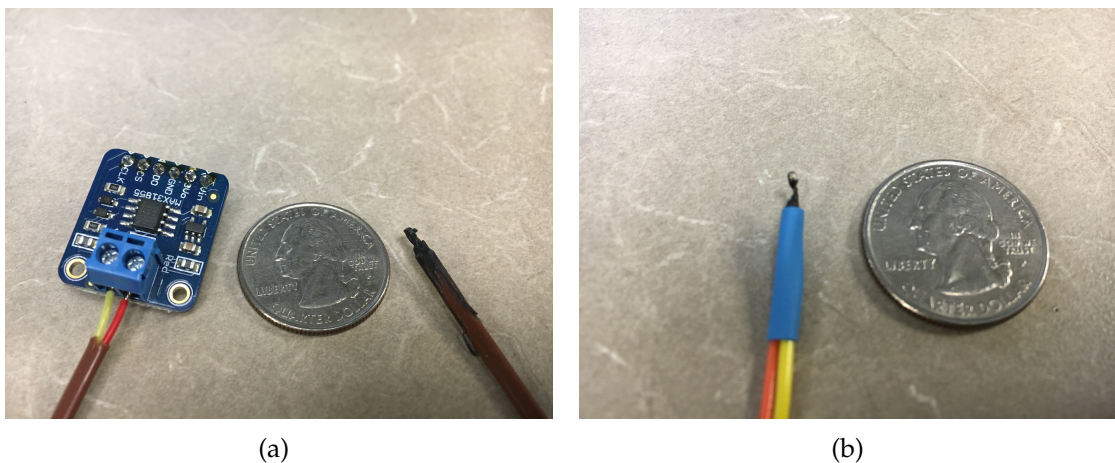


Figure 3.10: (a) Thermocouple constructed with accompanying circuitry (b) thermistor constructed

We performed bench tests on the thermocouple and thermistor shown in Figure 3.10 to compare their characteristics to the HOBO and MS5803 temperature sensor. We knew going into the tests that the HOBO and MS5803 were too slow, but the HOBO provided a good ground truth and it is what our collaborators use for their in-situ tests, and we had already used the MS5803 in some field trials, so we chose to include it in the tests to determine how much better a different sensor might perform. The bench tests were primarily to evaluate the performance of the thermocouple and thermistor and the other two sensors gave a baseline to compare against.

Figure 3.11 shows the response of the thermocouple and thermistor when plunged into ice water from warm water. This is the raw data without any filtering or offset. Table 3.4 provides a comparison of the important characteristics of the response.

The thermistor has a 90% settling time that is less than a second and an accuracy that was actually limited by the 10-bit ADC used to record the temperature.

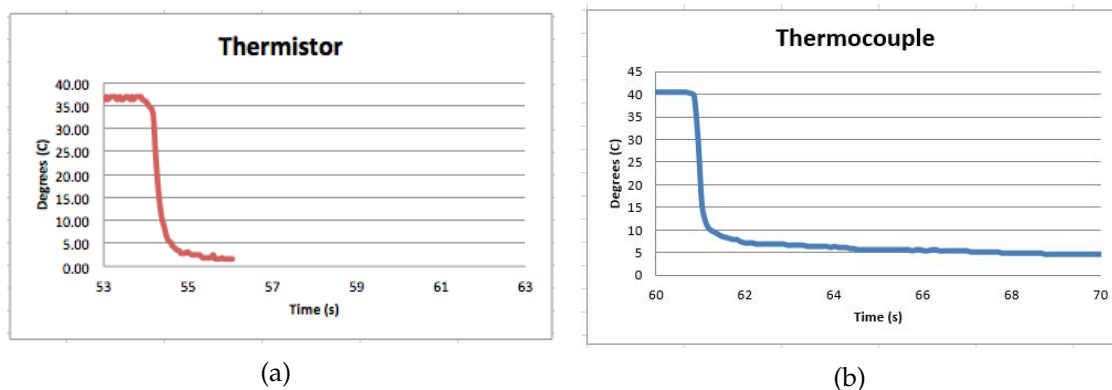


Figure 3.11: Temperature sensors' response when plunged into ice water

Table 3.4: Experimentally determined temperature sensor specifications

Sensor	90% settling time (s)	99.9% settling time (s)	accuracy ( $^{\circ}\text{C}$ )
Thermistor	0.759	2.784	$< 0.5$
Thermocouple	1.228	11.618	3.0

From the bench test performed, we can only know that the accuracy was less than  $0.5^{\circ}\text{C}$  and it may have been even better.

The thermocouple did not perform as well in our tests as the thermistor for several reasons. First, the thermocouple's accuracy looks poor in the bench tests we performed, but that is because the sensor is capable of measuring such a large range that  $3^{\circ}\text{C}$  is only 0.24% of its functional range, which is an acceptable accuracy. However, for our purposes, we need higher accuracy in the range we are interested in. The response time of the thermocouple is also slower than the thermistor, which is a result of our manufacturing process. The response time of a thermocouple is largely dependent on the junction diameter and insulation thickness if insulation is used. We hand manufactured the sensors by soldering the wires together and while we attempted to keep the junction as small as possible, arc welding the tips of the wires would have produced a smaller junction. Additionally, we insulated the wires with liquid electrical tape which resulted in

a relatively thick layer of insulating material. The insulation was necessary to electrically isolate the sensor since it is used in water, but finding a better, thinner material that is less thermally insulating would reduce the settling time for the thermocouple.

For the research applications that we want to apply a temperature sensor in the future, the thermistor looks like the best choice from the sensors we tested.

### 3.3.3 Temperature Sensor Field Tests

The following data was collected and analyzed cooperatively with our collaborators Sally Thompson, Michael Hamilton, and Michaela Chung from UC-Berkeley. The data were published in an article titled "Obtaining the Thermal Structure of Lakes from the Air" [17] in *Water*.

Currently, we have only field tested the MS5803 and HOBO sensors. Temperature sensing experiments were undertaken at Big Lake in Blue Oak Ranch Reserve (BORR), a 1330ha undeveloped ecological reserve managed as part of the University of California's Natural Reserve System. Two vertical arrays of HOBO sensors spaced 6.5m apart were installed 10m from the shoreline in 1.3m deep water on the western boundary of the lake.

Figure 3.12 shows the location of the two arrays in Big Lake and also the location where vertical profile measurements were taken. The HOBO sensors were used as the ground truth measurement for the temperature of the water at different depths. The MS5803 was suspended below the UAV and was lowered into the water as the vehicle descended. For the first experiment, the thermal sensor was lowered through the water column near (0.5m radius) one of the vertical arrays of HOBO sensors. Temperatures were recorded at 4 Hz for 30s at five points through

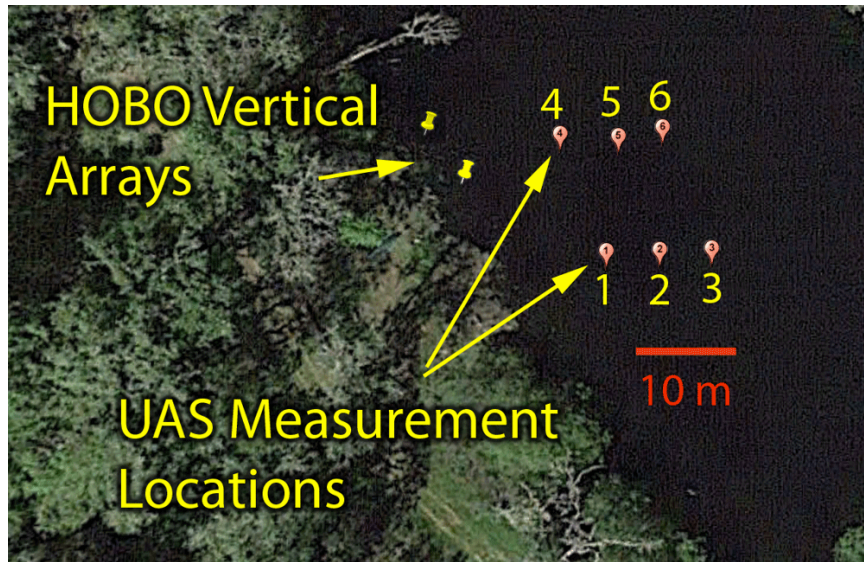


Figure 3.12: Location of the HOBO arrays and sample locations for one experiment set

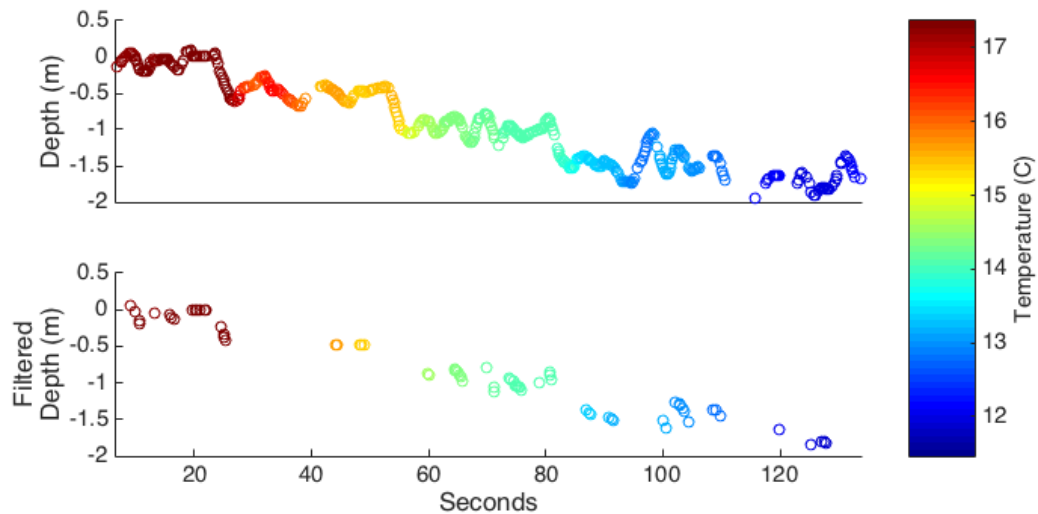


Figure 3.13: Raw and filtered temperature data from UAV-mounted sensor. The filtering removed data when either temperature or depth were rapidly changing.

the water column, at 0.2m depth intervals from 0.2m deep to the bed of the lake.

We filtered the temperature data for two reasons. First, the UAV altitude drifted up and down during flight, which caused the temperature sensor depth to vary by up to 25cm when it was supposed to be maintaining depth. Without

filtering, this would have caused multiple temperature readings to be associated with a given target depth. Additionally, the long settling time of the temperature sensor on the MS5803 meant that the actual temperature of the water was not accurately reported until the sensor had been at the target depth for a long enough period of time. For these two reasons, we filtered the data if either the rate of depth change or rate of temperature change was high.

Specifically, we excluded temperature readings when the rates exceeded the following:  $|\frac{\partial T}{\partial t}| \geq 0.04 \text{ } ^\circ\text{C/s}$  or  $|\frac{\partial m}{\partial t}| \geq 0.35 \text{ m/s}$ . These thresholds were determined by visually inspecting plots of temperature and depth rates of change and observing that during periods of minimal change, nearly all values are bounded by these thresholds. Figure 3.13 shows that this filtering method retained 15% of the original readings, and discarded most readings from the descent periods between the five measurement points in the water column.

After filtering the data from the MS5803, we compared the readings with the HOBO sensors. The temperatures measured from the UAS were consistently higher than the in-situ array-recorded temperatures, even following calibration. The magnitude of the temperature bias varied with depth in the water column and was highest in deeper areas of the water column. Figure 3.14 shows box plots of the bias associated with each temperature measurement made by the UAS over four flights, binned by depth in the water column. The bias is on the order of  $0.5 \text{ } ^\circ\text{C}$  in the surface  $0.5 \text{ m}$  of the water column and increases to  $1 \text{ } ^\circ\text{C}$  at greater depths below the thermocline.

These deviations in temperature are comparable to those made by other methods (e.g. TIR [56]; fiber optics [121, 122]). However, the deviations are much greater than previously seen in mobile sensing systems [62]. The depth-dependence in the magnitude of the bias suggests that a physical mechanism may be respon-

sible. We hypothesized that several mechanisms could explain the bias: thermal lag effects when the sensor was first introduced into the water column from the air, or entrainment of cold water from depth to surface layers as the sensor was raised from the lake bed to the surface. As a preliminary means to distinguish between these hypotheses, we explored whether the magnitude of the thermal bias at the surface varied between the first shallow readings and the final readings made during a flight.

Figure 3.14 shows that the UAV sensor temperatures remain higher than the in-situ sensor temperatures near the surface, but the bias is decreased in the first readings during a flight. The direction of the bias switches for the final shallow readings during a flight, with temperatures measured from the UAS being lower than the in-situ array-recorded temperatures. We suggest that these observations are more consistent with entrainment of cold water as the tube and sensor were moved up through the water column at the end of a flight, than with the effect of thermal lag. Thermal lag in the onboard UAS sensor would be expected to have led to large positive biases in temperature upon initial entry into the water column. Despite the temperature bias between the UAV and in-situ sensors, the UAV sensor's temperature resolution of  $0.01\text{ }^{\circ}\text{C}$  is sufficient to capture fine-scale thermal changes in the water column.

To remove systematic bias from the temperature sensors during the field trials and consider only relative variations in temperature, we also compared estimates of the local thermal gradient from each of the sensing platforms, shown in Figure 3.14. Below the water surface, both platforms produced comparable trends in the thermal gradient, again within  $1\text{ }^{\circ}\text{C}/\text{m}$  of each other. Both the peak in the thermal gradient associated with the thermocline, at a depth of approximately  $0.6\text{ m}$ , and increased thermal stability with depth were identified by both sensor plat-



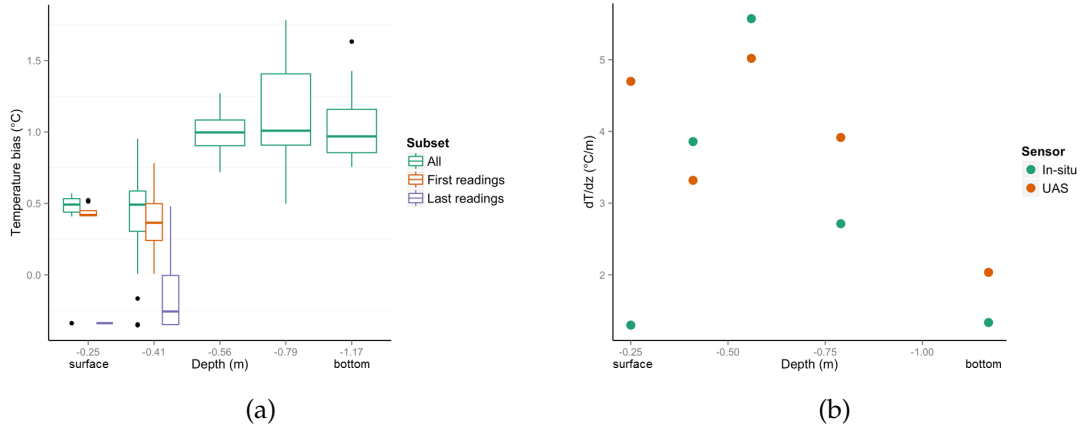


Figure 3.14: Comparison of UAS-borne and in-situ temperature sensors, including logged data and detected thermal gradient. (a) Bias in temperature measured at each depth (b) Comparison of derived temperature gradient at each depth

forms. Significant disagreement between the measurements was only observed in the top 0.25m of the water column, when the UAS measurements indicate a peak in thermal gradient comparable to that at the thermocline, while the in-situ sensors indicate fairly consistent temperature change with depth. The source of this high temperature gradient sensed by the UAV is likely associated with lack of elevation stability, which caused the sensor to be suddenly pulled out of the water when at the surface and undergo rapid temperature change.

After the experiment to compare the MS5803 temperature sensor to the HOBO sensors, we performed a second experiment with the MS5803 taking vertical temperature profile measurements mentioned earlier at the locations shown in Figure 3.12. At each of the six locations, we descended in 0.5m increments from the surface and held altitude for 30s at each increment. From this data and some interpolation, we constructed a three-dimensional temperature map of a  $10 \times 10 \times 2.5$  m region of Big Lake shown in Figure 3.15. The data were collected over two

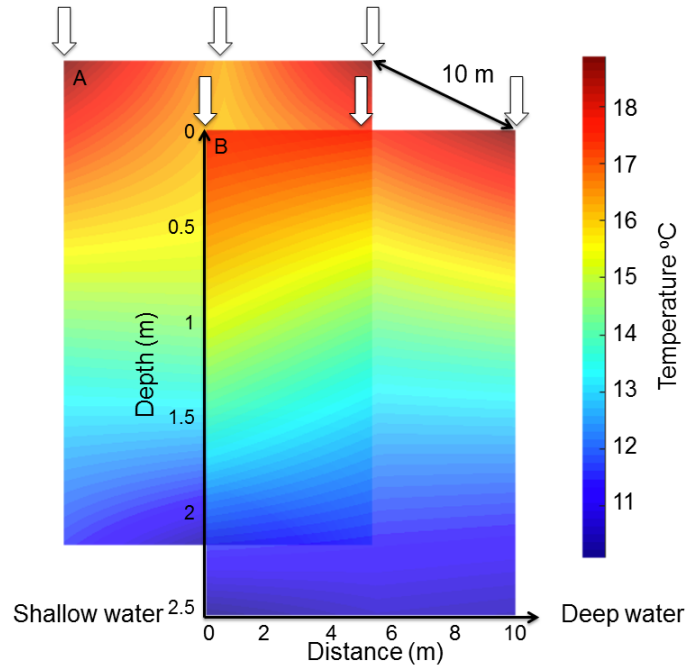


Figure 3.15: Thermal structure of a  $10 \times 10 \times 2.5\text{m}$  grid, interpolated and reconstructed from two UAS flights. White arrows indicate UAS's sampling locations, depth measurements were made throughout the water column at these sites.

flights totaling 26.5min of flight time.

In future work, we could construct a much larger temperature map in the same amount of flight time if we incorporate the thermistor that has a much faster response time than the MS5803. To achieve the same resolution as we did in our previous experiments, we could descend with a constant speed of  $0.65\text{m/s}$  and fly horizontally with a speed of  $6.6\text{m/s}$ , which allows enough time for the sensor to settle to 90% of the true value. Flying in a grid pattern at this speed would result in a map of a  $130 \times 130 \times 2.5\text{m}$  to be constructed. Alternatively, a smaller map of much higher resolution without the interpolation used in our previous tests could be constructed by flying slower.



### 3.3.4 Temperature Sensor Summary and Contributions

We constructed and lab tested 3 types of temperature sensor for use in creating 3D thermal structure maps of bodies of water using a UAV. We successfully field tested one of these sensors, the MS5803 and created a  $10 \times 10 \times 2.5$  m temperature map of Big Lake at BORR in California which resulted in a journal article titled "Obtaining the Thermal Structure of Lakes from the Air" [17] in *Water*. We overcame the challenges of capturing temperature data with a slow sensor and then lab tested a new sensor with a much faster response time to be field tested in the future.

I was responsible for the lab characterization and comparison of all sensors and John-Paul Ore of the NIMBUS Lab and our collaborators Sally Thompson, Michael Hamilton, and Michaela Chung from UC-Berkeley assisted me with the field experiment and with writing the journal article.

## Chapter 4

# The Waterbug

The Waterbug is a sub-surface sampling and data collection robot designed to operate at deeper depths than the water sampling UAV can reach. Additionally, a system model in Section 4.5 and an algorithm in Section 4.7 are developed which allow the Waterbug to become neutrally buoyant to monitor conditions at a specific location in the water column.

### 4.1 System Requirements

This section presents the high level system requirements for the Waterbug that were developed with our water science collaborators. These requirements drove the mechanical, electrical, and software design of the system.

**Size:** The system must be small enough for a scientist to carry several nodes in a backpack or for a UAV to carry and deploy a node. A Firefly hexcopter by Ascending Technologies is chosen as the reference platform [113]. The payload capacity of this UAV limits the total weight of the Waterbug and water sample to 600g or less. The design of the UAV attachment and deployment is outside the

scope of this work, and we only consider the weight limits of the node.

**Sample Size:** A minimum of 15mL of water is needed for ex-situ analysis by limnologists [123]. The device needs to be capable of collecting and storing this amount of water. Collecting more water is beneficial, since multiple tests can then be run on each sample, or excess water can be stored for later tests.

**Collection Depth:** The Waterbug must be capable of descending to water depths of 10m, collecting a sample, and returning to the water's surface. This depth is sufficient for analyzing many freshwater rivers, lakes, and ponds, and represents a significant improvement over prior collection methods [8]. The ambient pressure at this depth is approximately 14.2PSIG, so the mechanical design must be robust enough to operate at this pressure, and the sensors must function at this depth.

**Neutral Buoyancy:** The metric used for characterizing a successful neutral buoyancy actuation was based on a temperature sensor response time and spatial resolution. In order to get an accurate temperature reading, the node needs to hold depth for long enough that the temperature sensor has time to settle to the environment temperature. Areas of particular temperature or high temperature gradient are of interest to limnologists [17] so the ability to stop descending and observe the environment based on temperature is a significant functionality for the node. The tighter the control over depth, the higher the resolution of the gathered data. Using a temperature sensor with a response time of 5s or less [124] as the reference for the required loiter time and a vertical resolution of approximately one length of the Waterbug yielded a functional requirement of remaining within 200mm of the target location for at least 5s.

**Field Operation:** This device will be used in remote environments by minimally trained field researchers. Therefore, the system needs to be low complexity,

and not require any tools to field service. This requires the collection mechanism to be easily reset and not rely on many consumable resources so that it can be used in multiple experiments.

**Cost:** Inevitably, some nodes will be lost. The limited sensing radius of the nodes also means many will be deployed to cover an area. These factors make it important to keep the unit costs low.

## 4.2 Previous Iterations

The Waterbug evolved through several design iterations. David Anthony of the NIMBUS Lab collaborated with me on the early stage designs. Figure 4.1 shows several iterations and a brief overview of the design details is as follows.

All design iterations prior to the current model used a non-submersible pressure sensor which required a completely sealed chamber for the electronics. Several of the design iterations used a latex cover to seal the electronics compartment. The latex chamber provided a simple method of measuring water depth, reducing cost and protecting the electronic components. Because latex is very compliant, it deforms under pressure with very little resistance. Since the latex chamber was sealed before it was dropped into the water, the pressure inside the chamber was in equilibrium with atmospheric pressure or 0m depth. As the sample node descended, the external pressure exerted by the water increased, which deformed the latex chamber until the air inside the chamber was compressed so the inner air pressure matched the external water pressure. Since latex has effectively no structural rigidity, it provided no resistance to the compressing force of the external pressure which assured the inner air pressure and outer water pressure were equal. The latex also provided a convenient way of sealing off the electronics from

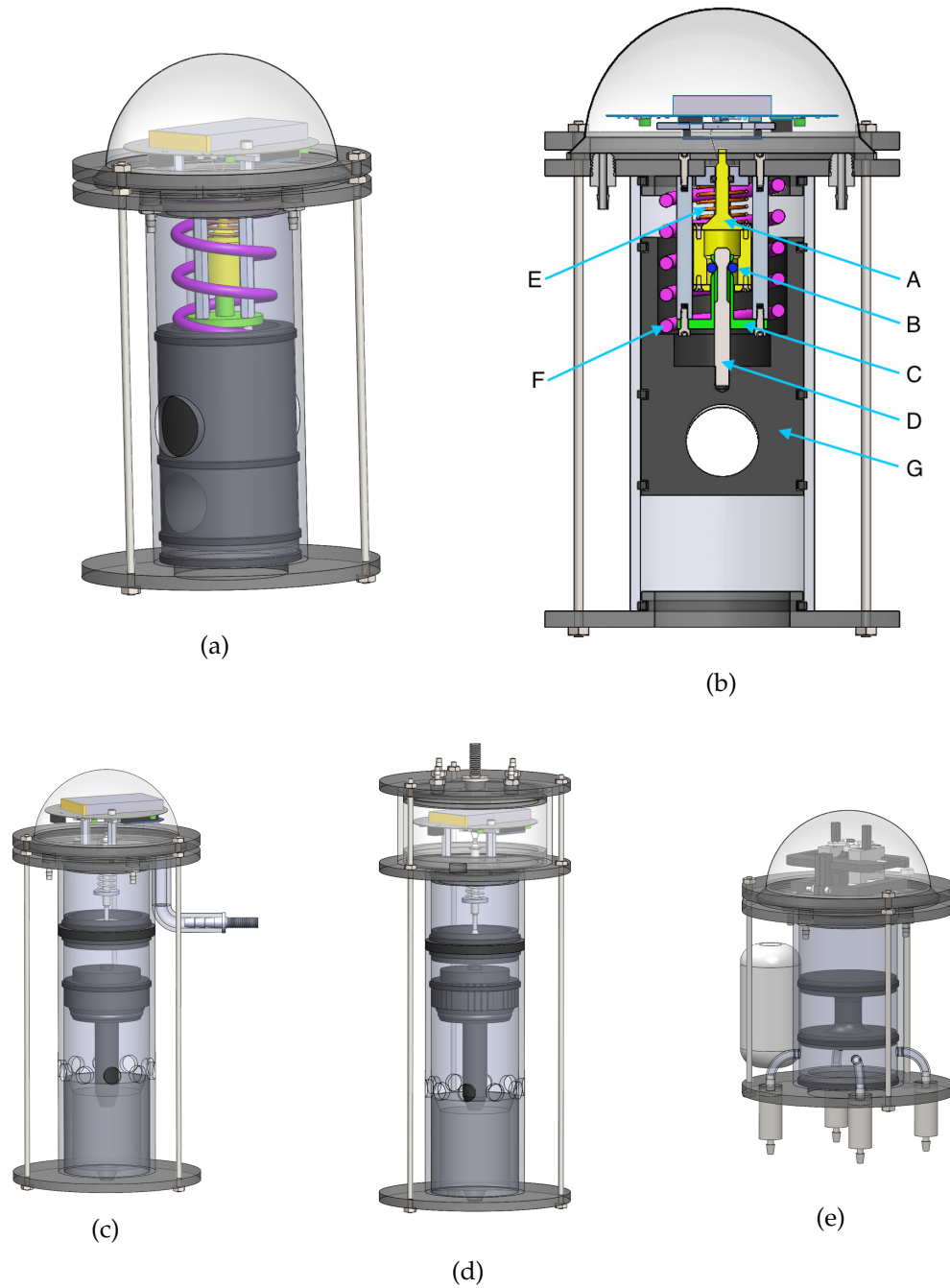


Figure 4.1: (a) Waterbug Revision 1.1 (b) Section view of Revision 1.1 (c) Waterbug Revision 1.2 (d) Waterbug Revision 1.3 (e) Waterbug Revision 1.4

the water.

A piston mechanism was used in early designs to simultaneously collect a

water sample and expand the internal volume of the sample node. This was an effective way of collecting and sealing the sample from the desired depth and changing the buoyancy of the sample node so that it ascended to the surface. While conceptually simple, the majority of the challenges with the mechanical design stemmed from the actual implementation of driving the piston down the cylinder against the opposing force of the water pressure. In revision 1.1 shown in Figure 4.1(a), fishing wire was going to be used to retain a compressed spring until the desired depth was reached, at which point, a heated nichrome wire would have been used to cut the fishing line, releasing the spring and driving the piston down the cylinder.

In order to have enough force to fully seal off the sample chamber and sufficiently change the internal volume so the sample node would ascend, the required spring exerted 170lbf when fully compressed. In order to use fishing wire to retain the spring, a two stage triggering mechanism was required (see Figure 4.1(b)). The yellow assembly (A) has a stepped internal diameter and is shown in the top position. In the top position, it jams the blue ball bearings (B) between the internal wall and the grey rod (D) that connects to the black piston assembly (G). The green cylindrical brace (C) holds everything in place by jamming against the blue ball bearings. The yellow assembly is held in place initially by the fishing wire. When the fishing wire is cut, the orange spring (E) forces the yellow assembly down which lets the blue ball bearings slide radially out, allowing the grey rod to slide down the axis of the green brace which is forced by the purple main spring (F). The main spring forces the piston down to its final position, collecting the sample and expanding the internal volume.

While mechanically robust and viable, this design required several machined parts made of Delrin and aluminum. After receiving the machinist's quote for

\$791.86 for just the machined parts, this design was revised to try and make it simpler and less costly.

Design revisions 1.2 and 1.3 shown in Figure 4.1(c) and Figure 4.1(d) still used the piston concept for sample collection and buoyancy control but instead of using a spring for providing the necessary force, part of the cylinder was filled with compressed air. The nichrome wire was still used to cut the fishing line, releasing a much smaller spring than in revision 1.1, which opened a valve to release the compressed air and drive the piston down, collecting a sample and increasing buoyancy. These two revisions were an improvement over the first from the perspective of requiring fewer machined parts, but they were still not as simple as desired. The spring required was much less formidable than the first revision but both spring actuation and pneumatic actuation were required which went against the goal of making the design as simple as possible.

In design revision 1.4 shown in Figure 4.1(e), the spring was completely eliminated which also eliminated the nichrome wire and associated electronics. The latex chamber was still utilized for protecting the electronics and facilitating pressure measurements. The actuation force was driven solely by pneumatic force which simplified the design compared to the previous two iterations. A small servo motor was used to trigger mechanical valves to control the flow of compressed air in the system. Check valves were used to control the flow of water into the sample chamber which initially started above the check valves and contained air at atmospheric pressure when dropped in the water. Once the node reached the trigger depth, compressed air was released into the upper part of the cylinder which forced the sample collection chamber down below the outlet of the check valves. At this point, the imbalance of pressure between the inside of the sample chamber and the outside water caused water to flow into the sample

chamber until the pressure equalized and the check valves closed and sealed the water in the sample chamber.

This design required the fewest amount of machined components yet and worked relatively well during evaluation experiments. However, there were several issues that caused problems with the design. The diameter of the acrylic tube used to form the wall of the cylinder was non-uniform. This made achieving an airtight seal difficult. An airtight seal was critical because of the use of compressed air for actuation. Even a small leak was enough to cause failure in the desired actuation. Additionally, the pneumatic switches began leaking at only 45psi which necessitated a large volume of compressed air to complete the desired actuation. Even with some successful tests validating the performance of revision 1.4, we were still not satisfied with the outcome, so we decided to completely overhaul the design to address the issues of the previous designs.

### 4.3 Final Mechanical Design

The finalized model and completed prototype are shown in Figure 4.2. The 6in ruler in the left frame gives a sense of scale. The three main components of the mechanical system are shown in Figure 4.3 with the electronics pod on top removed for clarity. The pneumatic system is shown in Figure 4.3(a), Figure 4.3(b) shows the sample collection system and Figure 4.3(c) shows the buoyancy system. These systems are described in the subsequent sections. The total cost to make a single node is \$120, which is significantly less than other actuated sensor nodes and even slightly less than passive sensor nodes of similar size [72, 73]. The solenoid valves used to control the pneumatic system are the most expensive component, costing \$26 each. The low overall cost makes it feasible to deploy many nodes for high



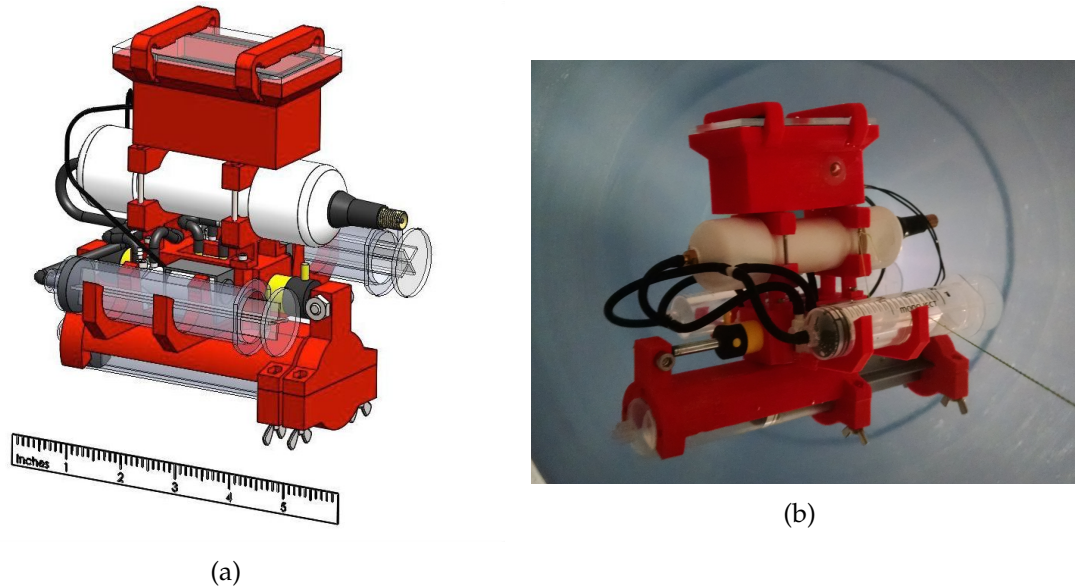


Figure 4.2: (a) Rendering of final model (b) Completed prototype in water during testing

resolution data collection, especially when considering the decrease in unit price for a larger production run. The overall length of the Waterbug is approximately 200mm at its greatest dimension which is important because making the node as small as possible allows better sensing of the significant vertical spatial structure in bodies of water [75]. A larger sensor or vehicle tends to have an averaging effect on these vertical structures.

#### 4.3.1 Pneumatic System

The actuation system on the waterbug is driven by pneumatic force. The compressed air storage tank is made from 0.75in schedule 40 PVC pipe rated to withstand 480PSIG at 73.4° F and is capped with a PVC pipe cap at both ends. The internal volume of the compressed air tank is approximately  $35\text{cm}^3$ . On one end of the compressed air storage tank, a standard Schrader valve was inserted to allow

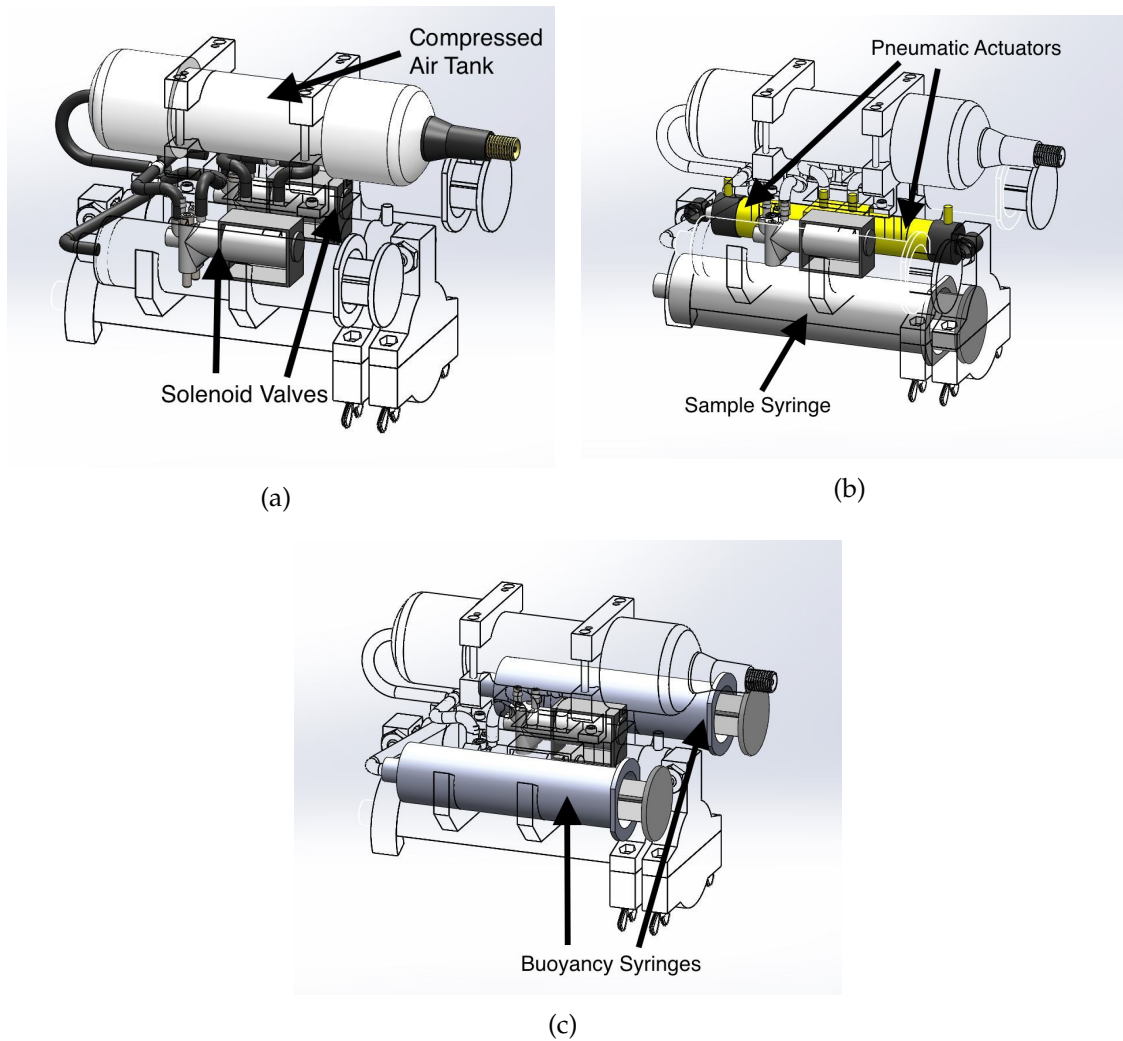


Figure 4.3: (a) Pneumatic system (b) Sample collection system (c) Buoyancy control system

charging with a standard bicycle pump or air compressor. On the other end of the tank, a barbed brass fitting was added for connecting an air line that is split with a Y-connection to run compressed air to the two solenoid valves. One solenoid valve is responsible for controlling air flow to the sample collection pneumatic piston actuators and the other solenoid valve controls air flow to the syringes used for buoyancy control. The solenoids used are ASCO™ RHB206H50B miniature two-way solenoids rated to operate at 12V and a maximum pressure of 70PSI

[125]. The solenoids draw approximately 160mA at 12V in order to open.

### 4.3.2 Sample Collection System

The sample collection system uses a 35mL plastic syringe to collect and store the sample. Syringes have been used by water sampling devices in multiple research applications [126, 127, 86]. The syringes are very inexpensive which means they can be discarded after use instead of requiring time to clean for reuse. The sample collection syringe is connected to two LEGO<sup>®</sup> pneumatic actuators mounted in series. Each actuator has a stroke of 28.4mm, giving a total draw length of 56.8mm on the syringe plunger which results in 25mL of fluid collected in the syringe. The sample collection system is robust because it is completely sealed to the environment except for the inlet to the syringe where the sample is collected. This improves on other water samplers with valves open to the environment that have issues with clogging in dirty water [128].

The sample syringe is easily replaceable without tools to allow redeployment in the field. Loosening four thumb screws releases the syringe from the two pneumatic actuators and then it snaps out of place to allow a new syringe to be snapped in place and secured to the actuators.

### 4.3.3 Buoyancy Control System

The Waterbug uses two 20mL syringes for one-way buoyancy control. Initially, the two buoyancy syringes are depressed so they have minimum internal volume. In this configuration, the Waterbug has a specific gravity greater than 1.0 so it sinks. After reaching the target depth or other condition, the buoyancy control solenoid is triggered to release compressed air into the two buoyancy syringes

so their internal volume expands, resulting in the specific gravity of the Waterbug decreasing to less than 1.0 and it ascends to the surface for retrieval. The maximum target depth for collecting samples is 10m where the pressure is 14.2PSIG. In order for the buoyancy syringes to fully expand, the internal pressure of every component connected to the pneumatic system must be greater than the external pressure. Assuming the compressed air tank starts at 60PSIG, the pneumatic system will have a final pressure of 17PSIG after actuating the pneumatic pistons for collecting a sample and expanding the buoyancy syringes. This provides a margin of safety to account for friction in the syringes, overshooting the target depth or the compressed air tank initially having less than 60PSIG pressure. The buoyancy syringes can also be partially expanded to achieve neutral buoyancy so that the Waterbug stops descending and maintains depth to monitor environmental conditions before collecting a sample and then fully expanding the buoyancy syringes to ascend back to the surface.

#### **4.3.4 3D Printed Parts**

The majority of the body is made from 3D printed ABS components designed using Solidworks and printed on an Ultimaker2 [129]. 3D printed parts help reduce custom part cost and since ABS can be dissolved with acetone, it is possible to make the parts waterproof by briefly dipping them in acetone to fuse the outer surface.

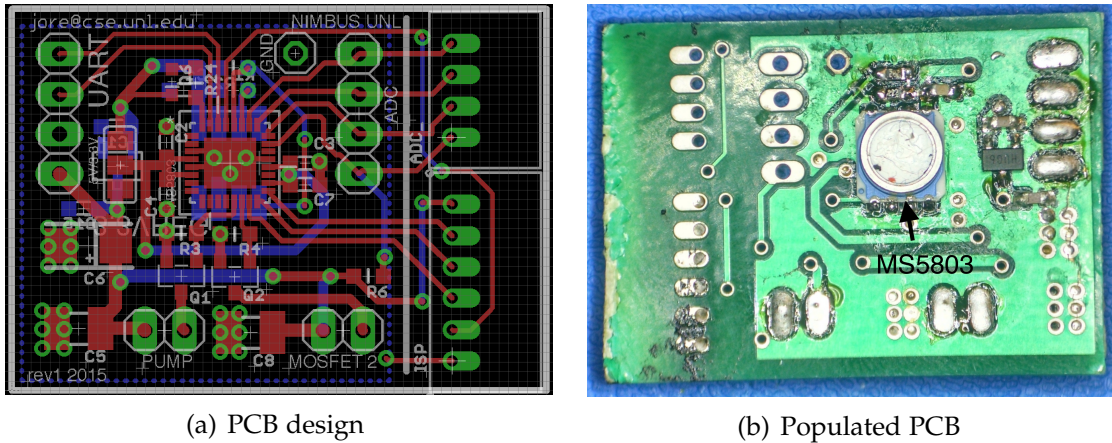


Figure 4.4: Electrical hardware design courtesy of John-Paul Ore

## 4.4 Electrical and Software Design

### 4.4.1 Microcontroller

The device uses an ATmega328P microcontroller [130] that has 2kB of RAM, 1024bytes of EEPROM storage, 32kB of flash program memory, 8 10-bit ADCs, and 23 GPIO lines. The active power consumption is less than 12mA at the maximum clock speed, which allows the device to conservatively operate for over 48 hours with the battery used.

### 4.4.2 Communications

The Waterbug's main mode of communication is a 2.4GHz XBee radio module [131] that has been configured to allow remote programming of target depths. The XBee is not intended for transmitting data while the Waterbug is submerged. Rather, it provides the convenience of interfacing with the on-board electronics and software without requiring physical access when the node is at the surface or onshore.

### 4.4.3 Sensors

The Waterbug currently has two main sensors on board with the capability to integrate more in the future. The sensors currently are an absolute pressure sensor and a temperature sensor.

The pressure sensor is the most critical sensor during a deployment. This sensor enables the Waterbug to estimate its depth in the water column. The particular sensor used in the Waterbug is a Measurement Specialties MS5803-05BA [132]. This sensor is designed for submersion and is capable of measuring from 0 – 72PSIA. The measuring end of the sensor needs to be exposed to the water but the other end of the sensor needs to be soldered to the PCB which is sealed inside the waterproof housing. A watertight seal was designed around the housing of the sensor to expose the measuring portion of the sensor while protecting the rest of the electronics from the water. Figure 4.4(b) shows the pressure sensor on the back side of the PCB.

The MS5803 has a temperature sensor integrated into it but it has a rather slow response time (90s on average for still water [17]) and it currently is not used. In the future, it would be possible to have events triggered by temperature readings or to have other functionality or data collection based on temperature sensor readings.

### 4.4.4 Mechanical Actuation

Two SSM3K329R.LF N-channel MOSFETs [133] control the state of the solenoids that control the pneumatic actuators. The MOSFETs are rated for 3.5 amps at 30 volts which is more than sufficient for the system, which keeps them running cool despite their small footprint. The gate of each MOSFET is connected to a separate

GPIO pin on the ATmega328p for independent control.

#### 4.4.5 Power

**Power:** The system is powered by a custom battery pack made from three 3.7V 750mAh single cell lithium polymer batteries connected in series [134].

#### 4.4.6 Software

The software for the Waterbug is written in C using SeamOS [135]. SeamOS is a lightweight codebase that is highly portable and encourages code reuse. SeamOS has an existing serial communication library, which makes interfacing to the XBee trivial. The Atmega328P has existing PWM and ADC implementations in SeamOS, which made it simple to use these components in this project as well.

For lab testing and debugging, the Waterbug can transmit data to an external receiver using the XBee radio. Currently, the sensors are polled at 80Hz for on-board calculations and data is transmitted every twentieth reading. In addition to live data transfer and flashing firmware in the lab, the XBee is used to reset the electro-mechanical components and could be used to offload data between field deployments.

When the Waterbug transmits data over the XBee, a Robot Operating System (ROS) node listening to the serial port on an external computer receives the XBee packets and decodes them [136]. The data are published in a single ROS topic containing a custom message type that includes each reading or piece of information. This ROS node can easily be integrated into a larger ROS system, and it also makes it easier to record the data for later analysis.

## 4.5 Waterbug Control

In this section, we develop the system model and feed-forward based controller used by the algorithm the Waterbug utilizes to achieve neutral buoyancy with only uni-directional buoyancy control.

### 4.5.1 Challenges, Goals and Assumptions

One of the first challenges with this system is that the node is slow to respond to input. It takes time for the buoyancy syringes to expand after being given an input of compressed air and it takes even more time for the node to reach a new steady state velocity after the syringes have finished expanding. This causes challenges with feedback control because system state measurements and correction attempts can be made significantly faster than the system responds which leads to overshooting and the node returning to the surface before reaching the target depth. Another challenge with feedback control stems from the mechanical nature of the syringes. Once they begin expanding, they slide quite easily, but overcoming the initial static friction takes considerably more force. Using feedback to make small corrections causes pressure to build up slowly in the buoyancy syringes and then a large jump in buoyancy when the syringes finally overcome static friction and over-expand. Feedback control has the advantage of being capable of dealing with disturbance in the system but for this particular system, pure feedback is not enough to achieve the design goal.

Feed-forward control has the distinct advantage, in this case, of being capable of predicting model performance in spite of delay, but the disadvantages of requiring an accurate system model and not correcting for disturbance. For a device intended to be used in the area of field robotics, it is all but guaranteed that there



will be disturbance in the system, so this must be accounted for.

The goal of the controller designed for the Waterbug is to use a two stage feed-forward controller with precompensation and intermediate feedback. The precompensation and intermediate feedback adjust the controller for the possible disturbances that are measurable with the onboard sensors and that can be corrected for. The precompensation accounts for differences in the Waterbug's initial volume displacement, which can be caused by entrapped air bubbles or the buoyancy syringes not being completely depressed initially. A higher initial volume has the effect of causing the node to sink slower than expected. The second and most probable cause of deviation from the ideal model is having the starting pressure in the compressed air storage tank differ from the expected 60PSIG. The intermediate feedback accounts for this variation and is discussed in more detail in Section 4.7.

An important assumption was made about the pressure in the syringes that would cause the mathematical model of the system to be underdetermined if not made. The pressure in the syringes is assumed to be equal to the external pressure from depth as long as the syringes haven't fully expanded. Once the syringes have fully extended and reached their stops, the internal pressure will increase beyond the external pressure, but at this point, additional input from the controller yields no increase in buoyancy, so it is outside the region governed by the controller. The assumption is reasonable because the syringes slide quite easily once they begin to expand so the plunger will continue expanding until the internal compressed air pressure approximately equals the external water pressure. The friction has a damping effect that contributes to the delay in the system but the magnitude of the force is negligible when compared to the force from pressure at depth.

### 4.5.2 Computational Fluid Dynamics (CFD) Analysis

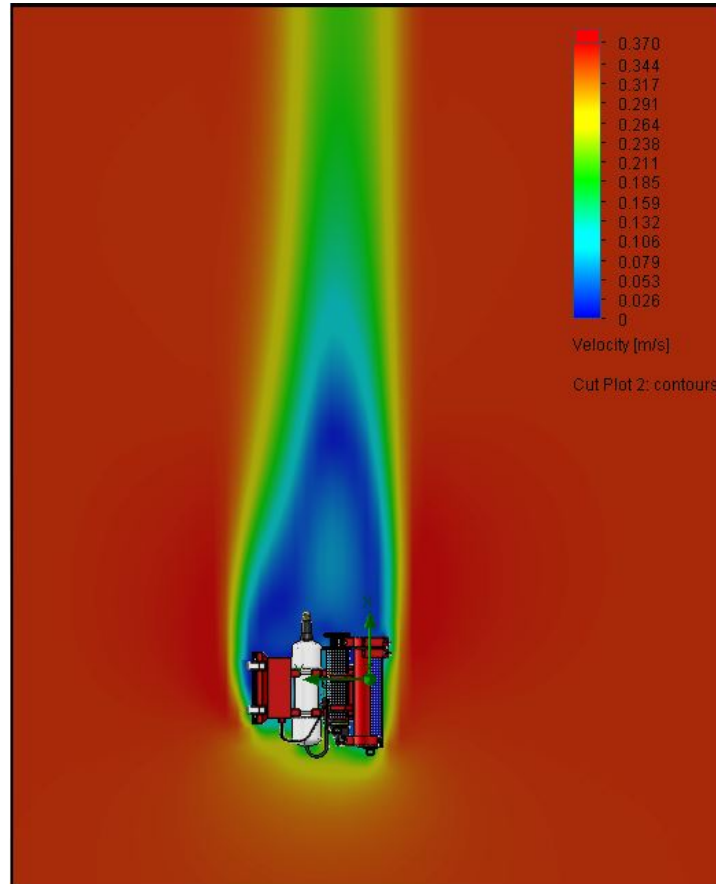


Figure 4.5: Section view of CFD analysis

The Solidworks Flow Simulation package was used to estimate the steady state drag force on the Waterbug during descent. This information was needed to help design the feed-forward control. The simplest way to conceptualize an external fluid flow analysis is to fix the object being analyzed and specify a rate of fluid flowing past it. This is the opposite of reality, where the fluid is quiescent and the object is moving through the fluid, but mathematically, the two situations are identical. The CFD analysis used a computational domain greater than 5 times the characteristic length of the Waterbug (assumed to be approximately the width) upstream and downstream to capture the complete boundary layer that

forms upstream and enough of the downstream disturbance to characterize the drag well.

Figure 4.5 shows the velocity profile of water flowing around the Waterbug, the boundary layer that develops ahead and the wake that forms behind. The areas of lowest velocity correspond to the highest drag. The analysis computed the total drag force on the Waterbug for a given input velocity. The force was computed for descent rates increasing by 0.05 m/s increments starting from 0 m/s. These data were used to generate the graph shown in Figure 4.6 which shows the steady state drag force as a function of descent velocity. Physical validation tests

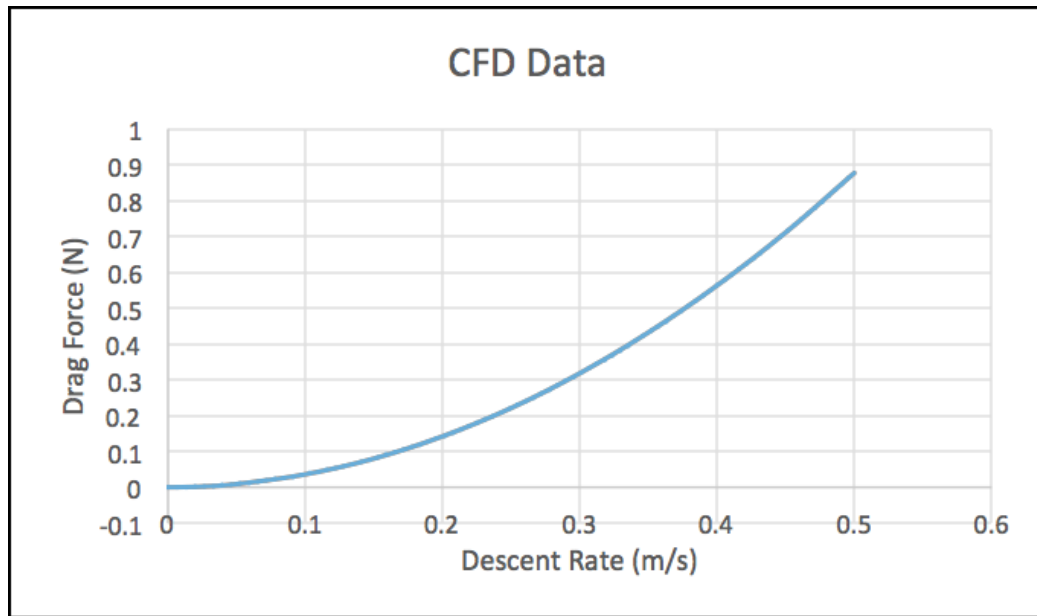


Figure 4.6: Drag force vs. velocity curve for CFD data combined with validation tests

were performed and the CFD and physical sets of data were compared to yield the equation,

$$F_d = 7.4498v^2 - 0.0926v - 0.0027 \quad (4.1)$$

where  $F_d$  is the drag force and  $v$  is the descent rate. Using the calculated descent rate and the previous function, the steady state drag force can be calculated during an actual descent. Since the drag force is equal to difference between weight and buoyancy once steady state conditions have been reached, the previous relationship between descent rate and drag force allows direct correlation between descent rate and buoyancy conditions. This allows a mathematical model to be developed from knowledge of the descent rate.

### 4.5.3 Mathematical Model

The goal of the model is to find the required time necessary to open the solenoid valve in order to achieve a desired descent velocity.

The buoyancy force is given by the equation:

$$B_F = V_{wb}\rho_w g - m_{wb}g \quad (4.2)$$

where  $B_F$  is the buoyancy force,  $m_{wb}$  is the mass of the Waterbug,  $V_{wb}$  is the volume displaced by the Waterbug,  $\rho_w$  is the density of water and  $g$  is the acceleration due to gravity. The mass of the Waterbug, the density of water and the acceleration due to gravity are all known quantities. Since the steady state drag force can be calculated from the descent rate using equation (4.1), the only unknown remaining in equation (4.2) is the time varying volume of the Waterbug.

Applying Boyle's law [137] yields the equation:

$$P_{t1}V_t = P_tV_t + P_{syr}V_{syr} \quad (4.3)$$

where  $P_{t1}$  is the initial pressure in the compressed air storage tank and  $V_t$  is the fixed volume of the compressed air storage tank.  $P_t$  is the time varying pressure in the compressed air storage tank.  $P_{syr}$  and  $V_{syr}$  are the pressure and volume in the buoyancy control syringes. The product on the left hand side of equation (4.3) is a constant and the pressure in the syringes is approximately equal to the pressure from depth during the times considered which is given by the following equation

$$P_{syr} = \rho_w g h + P_{atm} \quad (4.4)$$

where  $h$  is the depth below the surface of the water and  $P_{atm}$  is the atmospheric pressure.

The volume in the syringes is given by the equation

$$V_{syr} = Q_m t_{open} \quad (4.5)$$

where  $Q_m$  is the flow rate through the valve in cubic feet per minute (CFM) and  $t_{open}$  is the cumulative time the solenoid valve has been open. The flow rate,  $Q_m$  can be simplified so that it has two possible functions that describe its behavior. If the absolute pressure at the inlet of the valve is greater than double the absolute pressure at the outlet, the flow through the valve is considered choked and if

not, the flow is considered sub-critical. The sound barrier prevents flow from exceeding Mach 1 which is why the flow behavior is bounded by the choked equation. When considering the pressures that will exist during the majority of the time the controller is operating on the Waterbug, the flow will be choked so the flow rate through the buoyancy syringe will be governed by the equation

$$Q_m = 13.61 * P_i C_v \sqrt{\frac{1}{(S_g T)}} \quad (4.6)$$

where  $P_i$  is the pressure at the inlet of the valve in PSIA,  $C_v$  is the unitless flow coefficient for the valve,  $S_g$  is the unitless specific gravity with respect to air,  $T$  is the temperature in Rankine and the scalar constant is to account for converting units [138]. The inlet pressure in equation (4.6) is the pressure in the compressed air tank,  $P_t$ .

Going back to equation (4.3) and taking the first derivative with respect to time before making any of the substitutions derived in equations (4.4)-(4.6) yields

$$0 = \frac{dP_t}{dt} * V_t + P_{syr} * \frac{dV_{syr}}{dt} + \frac{dP_{syr}}{dt} * V_{syr} \quad (4.7)$$

Rearranging and substituting equations (4.4)-(4.6) into (4.7) gives the pressure in the tank,

$$P_t = \frac{-P_{syr} Q_m t_{open} \frac{dP_t}{dt} [W t_{open} + \rho_w g \frac{dh}{dt}] - \frac{dP_t}{dt} V_t}{W P_{syr}} \quad (4.8)$$

where,

$$W = 13.61 * C_v \sqrt{\frac{1}{s_g T}} \quad (4.9)$$

Equation (4.8) shows that the pressure in the tank depends on every other system variable considered as well as its own first time derivative, but it is essentially a first order ODE.

$$P_t = Ae^{-Bt_{open}} + P_f \quad (4.10)$$

The constant  $P_f$  at the end of equation (4.10) is the final pressure in the tank as time goes to infinity. Using initial conditions and internal volumes,  $A$  can be solved for:  $A = 0.532 * P_{t1}$ . Rearranging equation (4.3) with the new form for  $P_t$  and solving for the total node volume yields,

$$V_{wb} = V_c + \frac{P_{t1}V_t - V_t(0.532 * P_{t1}e^{-Bt_{open}} + P_f)}{P_{syr}(t)} \quad (4.11)$$

where  $V_c$  is the volume of the Waterbug when the buoyancy syringes are compressed and  $t_{open}$  refers to the amount of time the buoyancy solenoid valve has been open. The compressed volume of the Waterbug is approximately  $450cm^3$ . Substituting equation (4.11) into equation (4.2) and solving for  $t_{open}$  gives:

$$t_{open} = \frac{\ln \left( \frac{0.532 - \left( \frac{m_{wb}g - (7.4498v^2 - 0.0926v - 0.0027)}{\rho_w g} - V_c \right) \frac{P_{syr}}{P_{t1} V_{t1}}}{0.532} \right)}{-B} \quad (4.12)$$

which is a fully parametric equation solving for the time the solenoid valve needs to open for a given pressure in the compressed air tank, target descent velocity, depth, node volume, mass and appropriate coefficient  $B$ . Under the assumptions that the compressed air tank starts at a known pressure, the Waterbug volume and mass are known and the pressure, i.e. depth, can be measured using the onboard pressure sensor, the only unknown in equation (4.12) is the coefficient,  $B$ . The appropriate value for  $B$  was empirically solved for by carefully controlling the starting pressure in the tank so that the only variable in the model was  $B$  and then performing iterative trials with different values until the mathematical model corresponded with the physical tests. For a pure feed-forward controller, equation (4.12) is all that is required because it takes an input velocity, translates it into a length of time to open the solenoid valve which is the input to the plant and this would theoretically result in the Waterbug slowing to the desired velocity. However, as noted in section 2.4, this approach would not account for model inaccuracy or system disturbance. The effects of this are discussed in section 4.6.

## 4.6 System Sensitivity

The control algorithm's sensitivity to inconsistencies in input or environmental factors will have a significant impact on how successful it is out in the field. After



analyzing the different variables such as descent velocity and depth estimate most have very little impact for reasonable variations with the exception of one. If the assumed starting pressure in the compressed air storage tank,  $P_{t1}$ , varies by more than 1PSIG from the assumed starting pressure of 60PSIG, the Waterbug will not achieve the neutral buoyancy criteria. Figure 4.7 shows simulations of the system starting at the correct assumed pressure, 1PSIG under the assumed pressure, and 1PSIG over the assumed pressure. Even with such a small variation, the Waterbug's volume after triggering has enough error to result in a steady state descent or ascent that would cause it to pass in or out of the target window before 5s has elapsed.

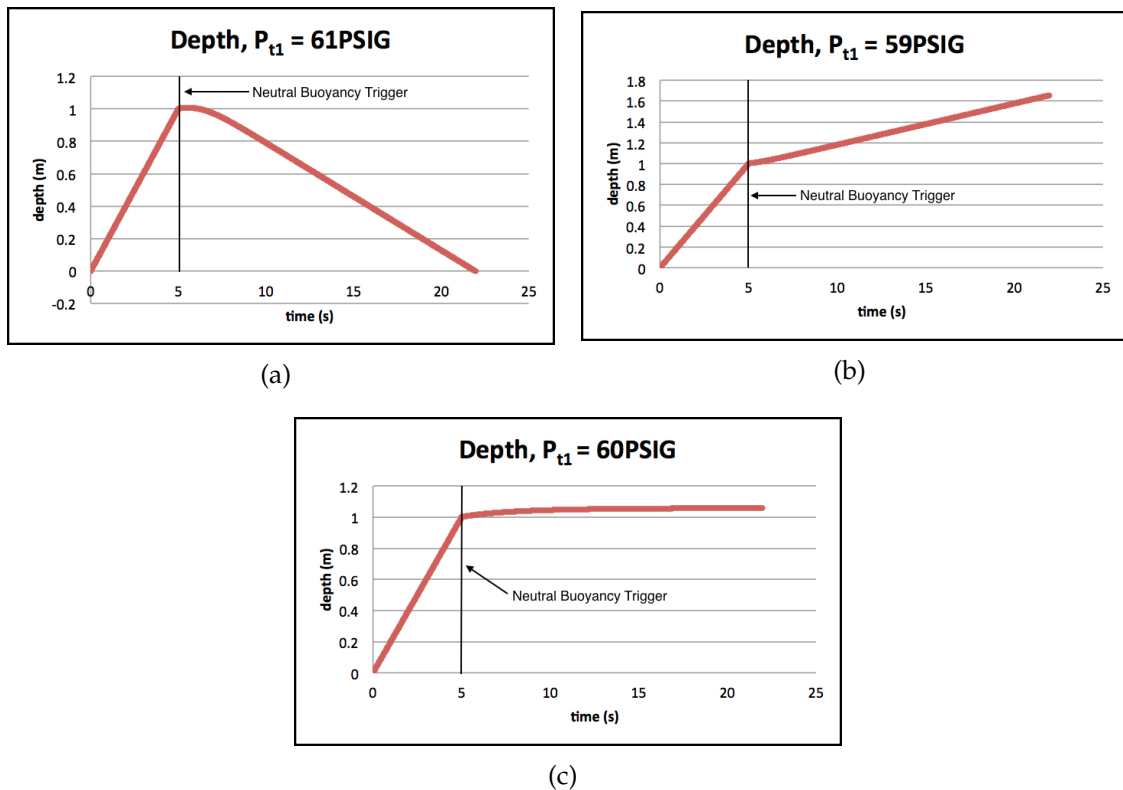


Figure 4.7: (a) Simulated depth for correct initial pressure (b) Simulated depth for under-pressurized tank (c) Simulated depth for over-pressurized tank

Consistently achieving a starting pressure of exactly 60PSIG is unrealistic for

several reasons. The pressure regulators in common air compressors are inexpensive and not necessarily reliable to the degree required to achieve less than 1PSIG accuracy repeatably. They also use analog gauges with low resolution so setting the pressure would still be difficult even if the regulator was perfectly accurate. In addition, when charging the pneumatic system with the Schrader valve, there is occasionally some leakage as the air fitting is pulled off the valve. The total volume leaked is likely small, but since the total volume in the compressed air storage tank is not large, the pressure change in the tank could be significant from this small leakage.

In light of the previous sensitivity analysis, using the mathematical model of equation (4.12) developed in section 4.5 with a blindly assumed starting pressure of 60PSIG in the compressed air storage tank would cause poor results. Therefore, a more robust neutral buoyancy control algorithm was developed to account for environmental and system variances.

## 4.7 Neutral Buoyancy Algorithm

Algorithm 1 shows an overview of the flow of the control algorithm. After the node is released at the surface, the descent rate is measured in line 3 after reaching a steady state and the model is precompensated to account for the true starting volume, which cascades through the algorithm. Steady state velocity must be achieved first so that the drag force is equal to the buoyancy force which allows equation (4.1) to be substituted into equation (4.2) and the actual Waterbug volume to be calculated based on the measured descent velocity.

$$V_c = \frac{(7.4498v^2 - 0.0926v - 0.0027) + m_{wb}g}{\rho_w g} \quad (4.13)$$

The next stage of the controller is feed-forward for the purpose of calibration. Equation (4.12) is utilized in line 7 to find the required time to open the solenoid valve, with an assumed starting pressure of 60PSIG in the tank, in order to slow to a target descent velocity of 50mm/s, which is one quarter the terminal velocity of the fully compressed node. The actual descent velocity of the Waterbug is measured in line 10 after pulsing the solenoid for the calculated time and waiting until the new steady state velocity is achieved. The projected target velocity of 50mm/s is based on an assumed starting pressure in the tank. The actual measured velocity is used to correct the assumption and back calculate the true initial pressure by rearranging equation (4.12) and solving for  $P_{t1}$ .

$$P_{t1} = \frac{\left( \frac{m_{wb}g - (7.4498v^2 - 0.0926v - 0.0027)}{\rho_w g} - V_c \right) P_{syr}}{V_t(0.532 - 0.532e^{-Bt_{open}})} \quad (4.14)$$

If the true pressure is not sufficient to expand the syringes at the target depth, the node can abort and return to the surface. Once the true starting pressure is calculated and determined sufficient, the variances that can be accounted for in the model are known and the new values can be used to calculate the total time necessary to open the solenoid valve to achieve zero velocity at the target depth shown in line 17. Once this depth is reached, the solenoid valve is opened for the calculated time minus the time already opened during the calibration stage. The Waterbug delays at least 5 seconds, then collects a sample and returns to the surface as shown in lines 19 – 21.

```

1: procedure NEUTRALBUOYANCY&SAMPLING()
2:   if steady state velocity achieved then
3:     measureVelocity()
4:     //use true volume to precompensate controller
5:     calcTrueVolume()                                ▷ use equation 4.13
6:     //target v=50mm/s
7:     calibPulse()                                    ▷ use equation 4.12
8:   end if
9:   if new steady state velocity achieved then
10:    measureVelocity()
11:    //back calculate true starting pressure
12:    calcTruePressure()                                ▷ use equation 4.14
13:  end if
14:  //wait until target depth is achieved
15:  if target depth achieved then
16:    //target v=0mm/s
17:    calcOpenTime()                                    ▷ use equation 4.12
18:    solenoidOn = calcOpenTime – calibPulse
19:    delay(5s+)
20:    collectSample()
21:    returnToSurface()
22:  end if
23: end procedure

```

Algorithm 1: Neutral Buoyancy and Sampling Algorithm

## 4.8 Evaluation

A series of tests evaluated the mechanical and electrical performance of the system. These tests reveal the capabilities of the system, and point towards future improvements to be made so that the device is field operable.

### 4.8.1 Maximum Depth

In order to test the maximum functional depth of the Waterbug, a pressure vessel was used to simulate the pressure that would be experienced. This allowed easy visibility and recovery when the maximum functional depth was exceeded.

Initially, 10m depth was simulated by pressurizing the vessel to 14.2PSIG with the node inside and triggering a sample sequence. The Waterbug performed a complete cycle that would have resulted in a full sample being collected and then ascending to the surface which verified that the node achieved its design parameter. For the sake of completeness, subsequent tests were performed to determine how deep the Waterbug could go and still be able to ascend to the surface.

At a simulated depth of 11.2m in the pressure vessel, the Waterbug just barely collected a full sample and fully expanded the buoyancy syringes. However, the buoyancy syringes required 10s to expand and since the node will continue to descend until the syringes have almost fully expanded, it likely would not have completed the expansion as pressure continued to increase with depth in a real scenario. Therefore, 11m is considered the cutoff depth for being capable of returning to the surface.

#### **4.8.2 Neutral Buoyancy**

A test apparatus shown in Figure 4.8 was constructed from a 10ft long, 12in diameter clear PVC tube stood on end and filled with water. This allowed for moderate depth tests while being able to maintain good visibility of the node for evaluation, which is not possible in a pool or lake. As stated earlier, the minimum criteria for a successful neutral buoyancy actuation is maintaining depth within one body length, i.e. 200mm, of the target location for at least 5s to allow settling time for a temperature sensor to get an accurate reading. 35 successive trials were performed to evaluate the performance of the system and control algorithm over three ranges of initial conditions shown in Table 4.1. Over the 35 trials, the Waterbug had an overall success rate of 80% for maintaining depth within 200mm

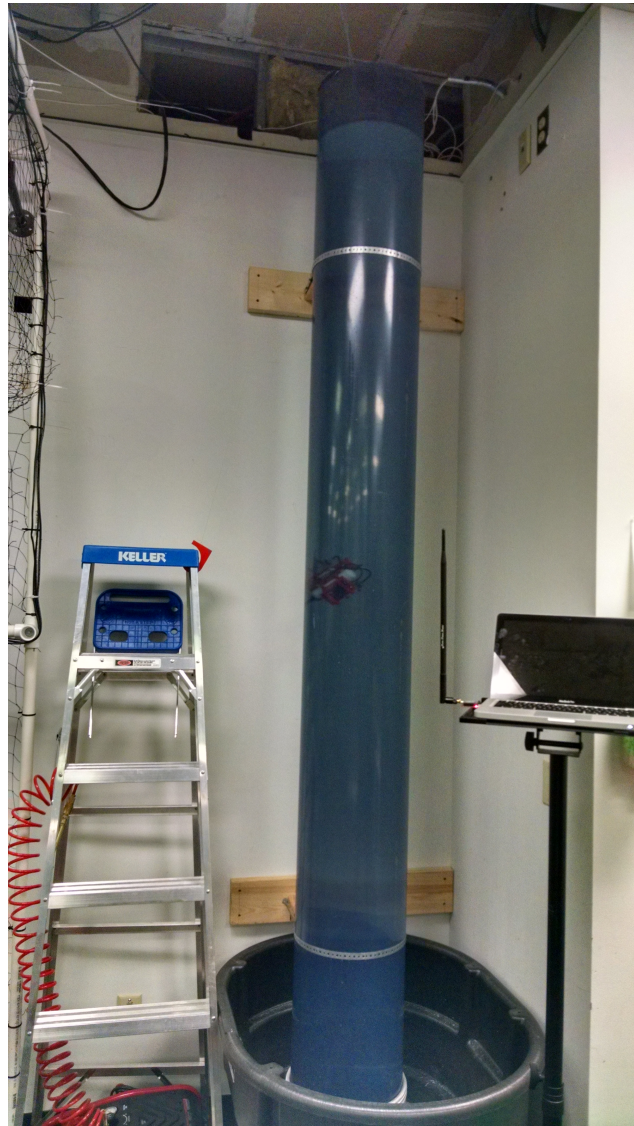


Figure 4.8: 10ft vertical water column for in-water lab testing

of the target location for at least 5s. Of the trials that failed to achieve neutral buoyancy, 5 trials overshot the buoyancy point and 2 undershot. The trials that undershot the buoyancy point did not slow their descent enough to stay in the target zone for the required time and the trials that overshot became too buoyant and ascended out of the target zone before 5s elapsed. Figure 4.9 shows a plot of the depth and descent rate for one of the successful trial experiments. When

Table 4.1: Results of neutral buoyancy attempts

Starting Pressure (PSI)	Trials	Success (%)	Mean Dwell (s)
55-59	10	90	16.6
60-64	15	73	15.3
65-70	10	80	10.8

the Waterbug reaches a depth of 600mm, the calibration stage is triggered, which slows the node to just over 70mm/s. This means that the true starting pressure in the tank was under the assumed 60PSIG. At the target depth of 1500mm, the second stage triggers and the node becomes neutrally buoyant and settles around 1630mm. Mechanical inconsistencies and initial conditions too far outside the

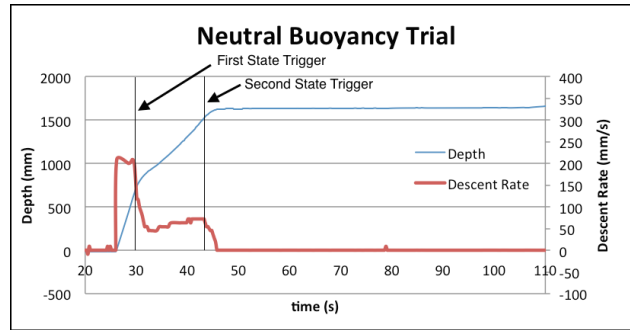


Figure 4.9: Depth and descent rate data for a neutral buoyancy trial

working envelope were the cause of the Waterbug failing to remain within 200mm of the target location for at least 5s after a neutral buoyancy attempt. At a starting pressure of 75PSIG in the compressed air tank, the first calibration stage of the control algorithm intended to only slow the descent caused the Waterbug to actually become positively buoyant and return to the surface before the rest of the algorithm could even run. Therefore, this bounded the upper limit for the initial conditions. The lower limit is bounded by the required pressure to return to the surface from a given depth.

The trials within the functional bounds that failed were caused by the buoy-

ancy syringes expanding an inconsistent amount. Even when given identical input, the expansion output would occasionally differ from the expected amount. The suspected cause of this problem is inconsistent friction in the buoyancy syringes. This problem is difficult to mitigate because the system model cannot account for this disturbance. Using feedback to correct for it is also challenging because the delay between input correction and output change is large and overshooting produces immediate failure because the controller only has unidirectional control.

## 4.9 Waterbug Summary and Contributions

In conclusion, we developed the Waterbug, a sub-surface sampling robot that is inexpensive, and small enough to be deployed and retrieved by a UAV. It is capable of autonomously descending up to 10m depth, collecting a sample and data, then returning to the surface. We also developed an algorithm that allowed the Waterbug to achieve neutral buoyancy in 80% of our trials while only utilizing one way buoyancy control. The algorithm overcomes challenges associated with variances in initial conditions, such as starting pressure and volume, from the expected values to provide robust functionality.

I was responsible for the mechanical design, algorithm development, testing, and evaluation of the Waterbug. John-Paul Ore allowed me to use a PCB he designed for the embedded system. David Anthony worked with me on early revision of the Waterbug and he also helped me with electronics prototyping.



## Chapter 5

### Prescribed Fire and the UAS-FF



Figure 5.1: Autonomous aerial fire ignition system during a field trial

This chapter is about a UAV-mounted device for performing aerial fire ignitions shown in Figure 5.1. While this is quite unrelated to water science, the same core challenges of designing light-weight systems that allow greater interaction

with the environment remain, and it constituted a significant portion of my research while a member of the NIMBUS Lab.

## 5.1 System Requirements

For the UAS-FF to be successful, the technical capabilities must align with the requirements of the fire-ignition domain for which they were designed. This context is defined by target areas covering hundreds to thousands of acres, teams of firefighters performing different roles and operating a variety of vehicles, all working under a burn plan and a set of regulations and common practices, and operating in specific ignition situations that make firefighters especially vulnerable. This context and our early studies with fire ecologists, land managers, and firefighters defined an initial set of parameters that have influenced the design of the UAS-FF:

**Size:** The entire system must be small and light enough to be carried by a single firefighter.

**Field Operation:** The system must be easily deployable and operable in a hostile environment that could include wind gusts, smoke, high temperatures, and difficult terrain such as canyons, gullies, and obstructions.

**Safety:** The use of the UAS-FF for igniting fires must not increase the potential for uncontrolled fires.

**Regulations:** Operation must align with the large body of procedures and regulations on how such fires must be conducted.

These requirements drove the design of the mechanism prototype built on a micro-UAS platform that can navigate, deliver an ignition payload with enough precision to remain within a specified region, and that replicates an accepted form

of fire-ignition delivery in a miniaturized and automated manner without placing personnel in danger.

**Ignition Payload:** The payload is a 1.25in plastic ignition sphere that is commercially available and currently is used in large quantities by helicopter based aerial ignitions. Two different types of ignition spheres were used, one produced by SEI Industries [111] and the other produced by Aerostat, Inc [112]. Both types contain approximately 3g of potassium permanganate and are manufactured to withstand high impact, which ensures the spheres stay intact when dropped from altitude, but it also means up to 115N is required to puncture the wall of the sphere.

**Mechanics and Actuation:** The device needs to perform four basic functions: Carry extra spheres during deployment, position and release spheres, puncture the sphere wall, and inject anti-freeze into the sphere. The puncturing actuation is the most challenging aspect because of the significant force necessary to pierce the impact rated wall.

## 5.2 Mechanical Design

The purpose of the mechanism on the UAS-FF responsible for actually igniting the fire is to start an exothermic chemical reaction that eventually results in a flame. The plastic ignition spheres are filled with potassium permanganate powder and when the spheres are injected with ethylene glycol (the main ingredient in common antifreeze), an exothermic reaction starts that shortly bursts into flames. One of our major design goals was to require no preparatory work from firefighters to use the system. We wanted our system to seamlessly integrate with the commercially available ignition spheres and antifreeze so a firefighter could simply

drop in the spheres and antifreeze and use the system just like a larger manned helicopter except without the cost and danger. This means that we had to take the technology used in aerial ignition helicopters and shrink it to a fraction of the size and weight while performing the same function. The mechanism on the UAS-FF requires four functional subsystems to perform the task of igniting a sphere. The four subsystems are a hopper container, a loading/releasing mechanism, a piercing mechanism, and an injection mechanism.

The mechanical design of the mechanism for igniting the fires has gone through two major iterations. Version 1.0 was developed over 1.5 years and version 2.0 was developed in less than a month after field trials of the initial version exposed weaknesses that had to be quickly overcome before the next set of trials. Section 5.2.1 details the design of version 1.0 and Section 5.2.2 similarly explores the design of version 2.0.

### 5.2.1 Version 1.0

Version 1.0 underwent many minor changes during its development, was lab tested, and even successfully tested in the field. The major differences of versions 1.0.1 – 1.0.3 centered around mounting mechanisms and the hopper mechanism. There were many more subtle design changes resulting from insight gained through testing that were incorporated through the development process. We will first begin with a description of the core mechanism and its functions that remained largely unchanged and then give details about the distinctions between versions 1.0.1 – 1.0.3.

**Subsystems:** Figure 5.2 shows the subsystems from V1.0.3 mentioned earlier that make up the fire ignition system of the UAS-FF.

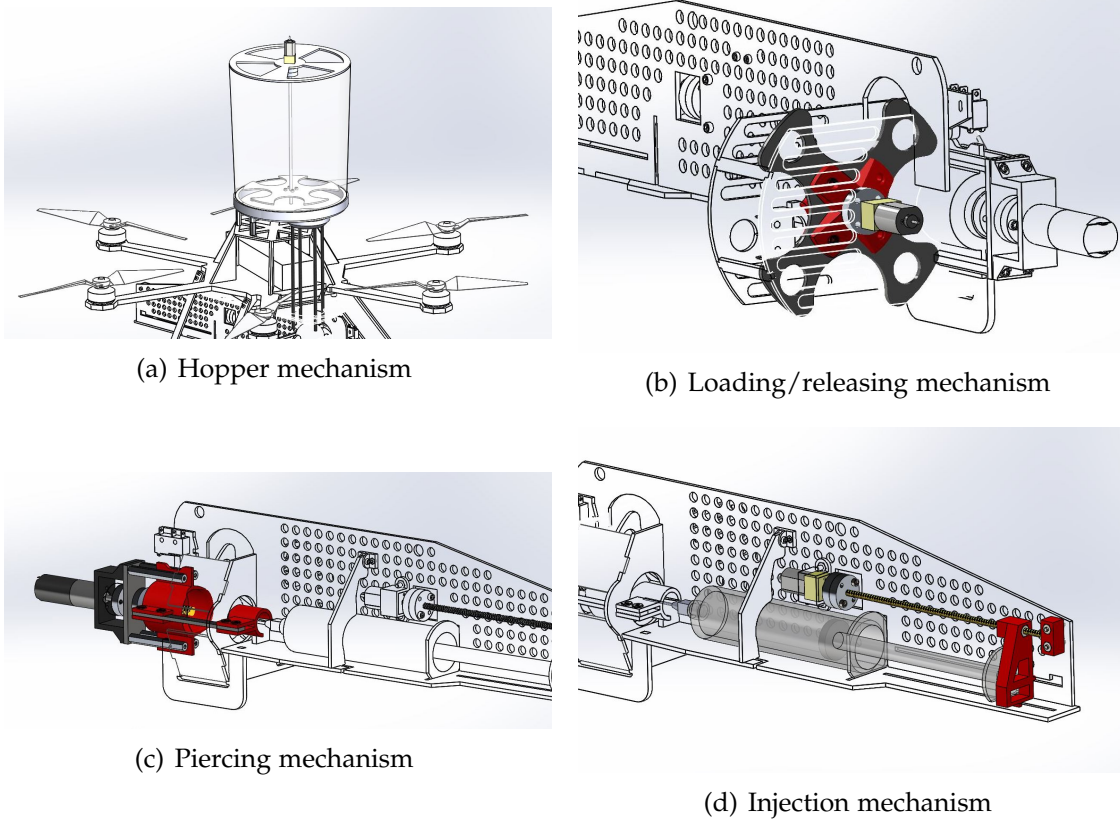


Figure 5.2: The four subsystems that make up V1.0.3 of the fire ignition mechanism of the UAS-FF

**Positioning Process:** The sphere drops into the loading/releasing mechanism from the hopper, shown in Figure 5.3, where it is ready to begin the process of being injected with ethylene glycol to start the chemical reaction. The loading/releasing mechanism positions each sphere to be punctured as well as ferries the spheres from the top loading position to the bottom releasing position. The mechanism is composed of an acrylic plate with slots cut in it to fit the spheres and 3D printed components that have an integrated rotary cam for tripping a limit switch for position feedback. The mechanism is driven by a 10g brushed gearmotor with a relatively high gear ratio of 298 : 1 [139] so that it has enough torque to force a partially jammed sphere out of the mechanism if it ever occurs.

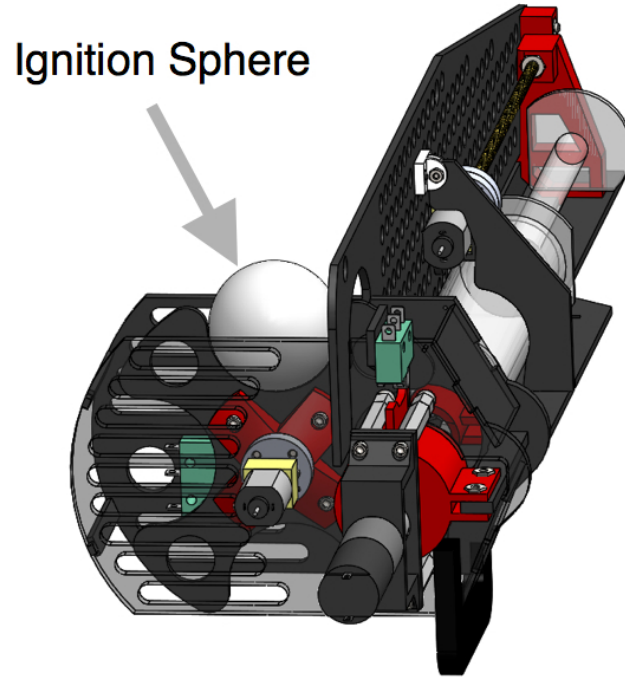


Figure 5.3: Ignition sphere in loading/releasing mechanism, ready to be processed through the ignition procedure

**Piercing Process:** After the sphere drops into the loading/releasing mechanism, it rotates 90° to position the sphere in place for the pierce mechanism to puncture the ball. Figure 5.4(a) shows a section view that details the pierce ram, the pierce lead screw and driving motor that forces the ram forward, puncturing the sphere onto the needle. The motor was sized using equation (5.1).

$$F_a = \frac{2\pi}{16} * T * P * E \quad (5.1)$$

where  $F_a$  is the axial force in lbf, the constant accounts for units and translates rotational motion to linear motion,  $T$  is the motor torque in oz-in,  $P$  is the pitch in threads-per-inch of the lead screw connected to the driving motor, and  $E$  is

the efficiency of the lead screw. To be conservative, we assumed the efficiency of the lead screw to be only 30% because we are using a standard triangular thread form.

The driving motor chosen is a Faulhaber 1524B012SR+15A 14 : 1 gear motor which is a 1524SR series motor with an integrated 15A series plastic gear planetary gearbox and an encoder. The entire assembly weighs 26g, has a stall torque of 8.5oz-in, and a no-load speed of 700RPM at 12V. The lead screw we attached to this motor has a nominal diameter of 5mm with a lead of 0.8mm. According to equation (5.1), the motor/lead screw combination should be able to produce 142N of axial force. The ram travels 15.25mm which takes approximately 1.5s with the combination of gearbox, lead screw and voltage powering the motor.

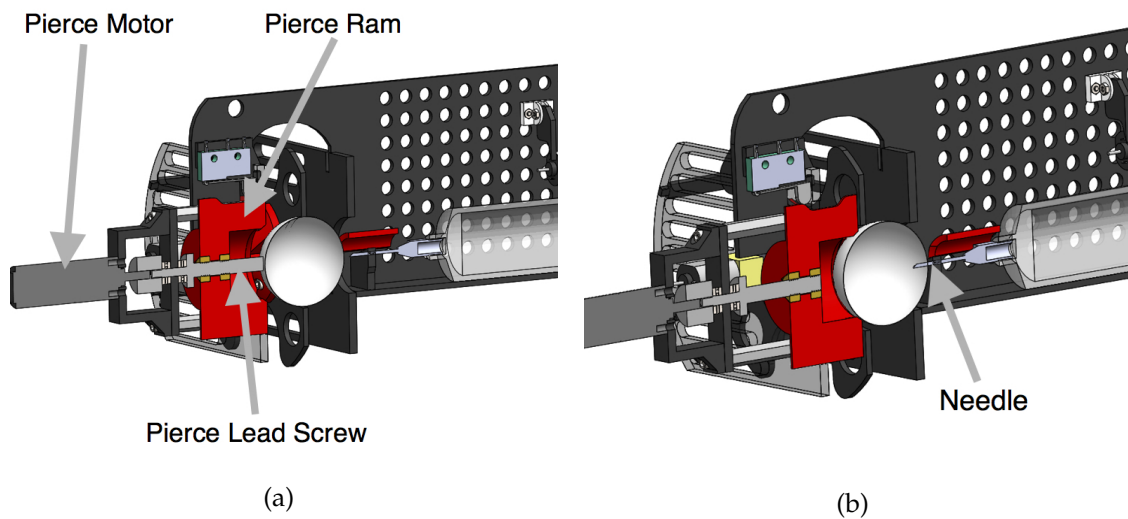


Figure 5.4: Section View: Ignition sphere punctured onto needle by piercing mechanism

**Injecting Process:** The ram pierces the sphere onto the needle shown as a section view in Figure 5.4(b). After the sphere is pierced on the needle, the injection mechanism, shown in Figure 5.5 injects 0.5mL of antifreeze into it. The injection



mechanism is driven by a 50 : 1 gear ratio gearmotor [114] which connects to a lead screw with a nominal diameter of 3mm and lead of 0.5mm. The lead screw drives the plunger ram which depresses the syringe plunger to inject antifreeze into the ball through the needle. Using a gear motor and lead screw results in a large reduction which allows a high degree of precision in the amount of fluid injected into the sphere because each milliliter injected corresponds with several thousand encoder increments.

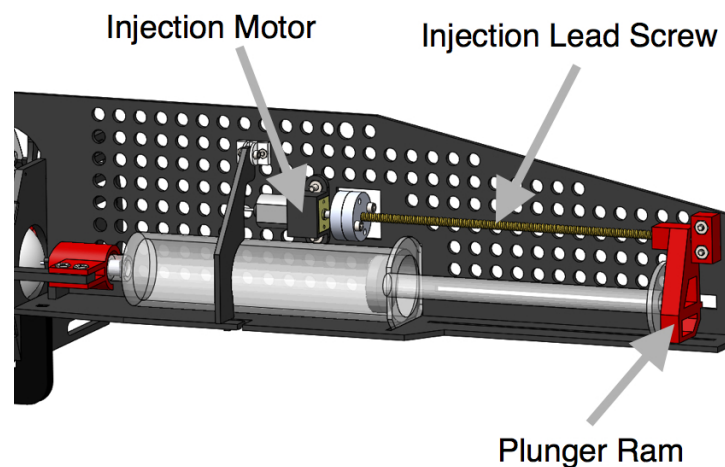


Figure 5.5: Injection system squirts a small amount of fluid from syringe into ignition sphere

**Releasing Process:** After the sphere has been injected with antifreeze, it is primed and will ignite in less than 60s. The pierce mechanism runs in reverse to retract the sphere off the needle and the loading/releasing mechanism rotates another 90° so that the sphere is rotated to the bottom of the mechanism as shown in Figure 5.6 where it drops out of the mechanism, falls to the ground, and the entire process repeats for the next sphere.

The UAS-FF design remained stable in the previously described configuration during a significant amount of lab and field testing.



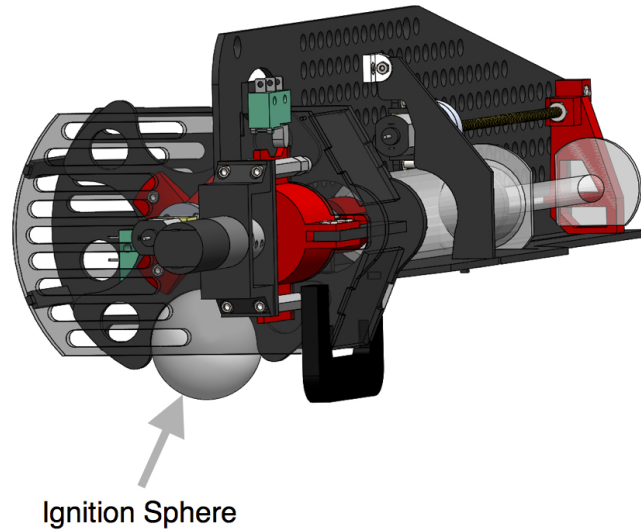


Figure 5.6: Loading/releasing mechanism rotates again to move the ignition sphere to the bottom of the mechanism where it drops out of the UAS-FF

**Previous Iterations:** Two iterations were developed and tested prior to version

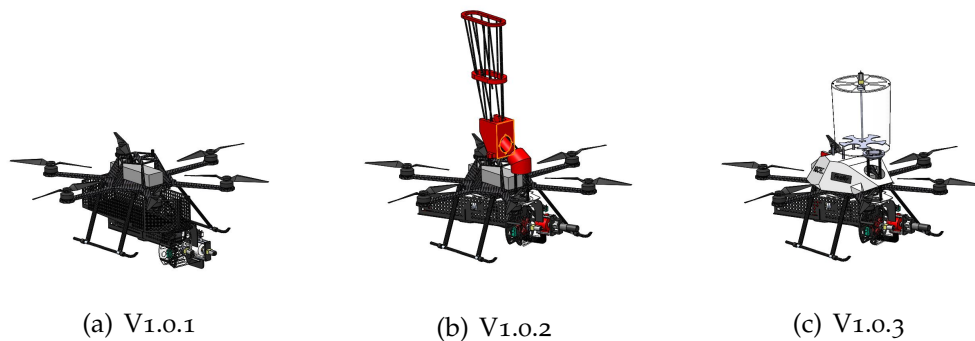


Figure 5.7: (a) Version 1.0.1 with under-mounted hopper (b) Version 1.0.2 with over-mounted gravity fed hopper (c) Version 1.0.3 with agitated hopper

1.0.3. The three iterations are shown in Figure 5.7. Version 1.0.1 was the first complete prototype produced and it was secured to the vehicle via fishing line. The fishing line mount was used so that if an ignition sphere caught fire in the mechanism, it would burn through the line and the mechanism would drop away, preventing the vehicle from being destroyed. In practice, the fishing line was

relatively difficult and time consuming to attach. The hopper was a basket like structure that was attached directly to the rest of the mechanism and the entire device mounted below the vehicle. The ignition spheres had a tendency to jam in the hopper so that no more ignition spheres could be cycled through the device. The height of the hopper and mechanism was taller than the landing gear so the UAV had to be hand launched and landed, which is less than ideal. This prototype left much to be desired but it proved the viability of the concept by successfully flying and igniting spheres during a field test inside a rodeo arena.

Version 1.0.2 improved on V1.0.1 by redesigning the attachment and hopper mechanisms. The hopper was designed to mount above the vehicle and drop spheres down a chute to the ignition mechanism mounted below the vehicle. The hopper jammed less easily than the previous design but would still occasionally jam, especially if the spheres got dirty or damp, which tended to make their outer surface tacky. Moving the hopper on top of the UAV also reduced the height of the components mounted under the vehicle so that it could be launched and landed from its landing gear. The mechanism mount was designed to have one mounting plate attached to the vehicle and a second mounting plate that attached to the ignition mechanism with fishing line. This retained the design feature of a break away mechanism in case of fire while allowing the two mounting plates to Velcro together for much faster mounting on the UAV. Version 1.0.2 was a significant improvement over the previous version but the hopper jamming issue needed to be addressed.

Version 1.0.3 retained the mounting mechanism from the previous version but a completely new hopper was designed that utilizes a motor to agitate the spheres in the hopper to prevent the jamming issues that occurred with the purely gravity fed versions previously. The hopper is a cylindrical shaped polycarbonate

structure and the agitator is an acrylic plate with five slots cut in it that attaches to a drive shaft driven by a motor mounted on top of the hopper.

This hopper is capable of holding over 50 ignition spheres. The agitator delivers spheres to a chute made of 3mm carbon fiber rods that transfers the spheres from the hopper above the UAV to the mechanism below the UAV.

**Lessons Learned:** The original design specification limited the weight to 250g for the ignition mechanism to allow 50 ignition spheres to be carried while remaining under 500g total for the vehicle payload. This was an extremely restrictive specification and forced compromises to be made in the areas of structural strength and actuator size which basically meant that both the load bearing materials and motors were operating near and sometimes over their maximum capacity. This resulted in the mechanism breaking or actuators failing.

Another downfall of version 1.0 was that it required very fine adjustments that had to be set carefully in order to function properly. If these adjustments were not set properly or one of the ignition spheres was manufactured poorly, at best, the mechanism didn't work, it broke in a less fortunate case, and it lit itself on fire in the worst case (this only happened once). The instance when the mechanism set itself on fire was a result of the mechanism jamming due to one of the adjustments being out of tolerance and poor alignment during the piercing procedure. As a result, the sphere got caught after it was primed with antifreeze and could not be ejected from the mechanism. The error was recognized by the software and it alerted the operators who quickly landed the vehicle and manually removed the mechanism from the UAV and then the flaming sphere from the mechanism before significant damage occurred. A more detailed evaluation of version 1.0 is given in Section 5.3.

All in all, version 1.0 taught us many valuable lessons and helped us think about creating designs that are tolerant of errors both in adjustment and manufacturing which led us to developing version 2.0.

### 5.2.2 Version 2.0

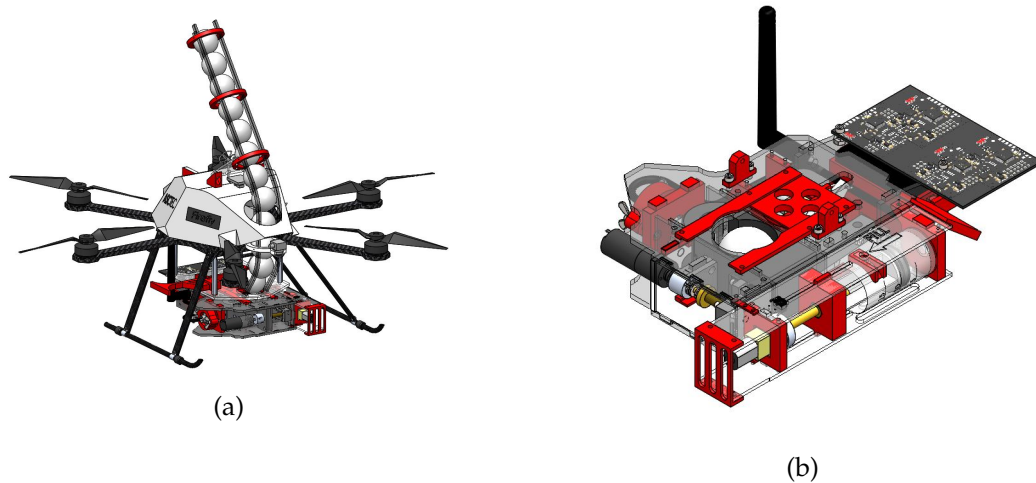


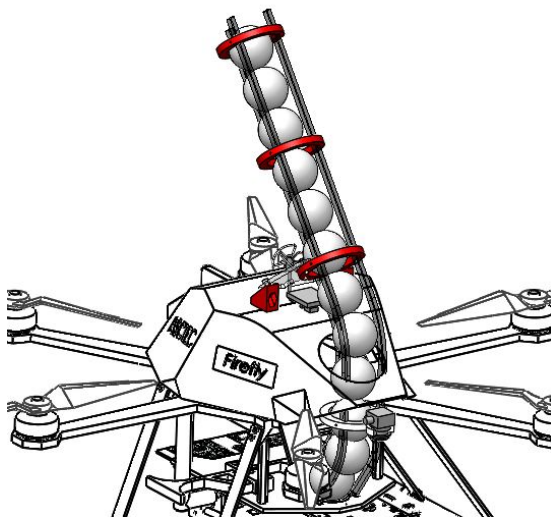
Figure 5.8: (a) Version 2.0.1 on the UAV with new mounting mechanism and hopper (b) Version 2.0.1 mechanism

The lessons we learned from version 1.0 helped us develop version 2.0 in a much shorter time frame. The fact that we only had a few weeks between starting the design and its debut in a field trial that involved the National Parks Service, the Department of Interior, the Federal Aviation Administration (FAA), the Bureau of Alcohol, Tobacco and Firearms (ATF) and a significant amount of media also encouraged us to complete the design in an expeditious manner. The ATF was involved because initially, the ignition spheres were considered live munitions, so they had to review our usage.

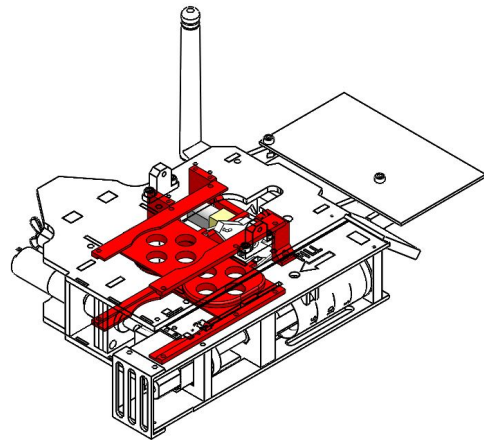
Version 2.0 is shown in Figure 5.8 and is a complete redesign. We incorporated the lessons we learned from V1.0, as well some new ideas. One other important change for V2.0 was that we decided to carry a maximum of 13 ignition spheres per deployment. This increased the allowable weight for the ignition mechanism to 425g which allowed us to make the mechanism stronger than in V1.0. V2.0

is also more compact which allows us to use thicker material and reduce the moment arms in high stress areas.

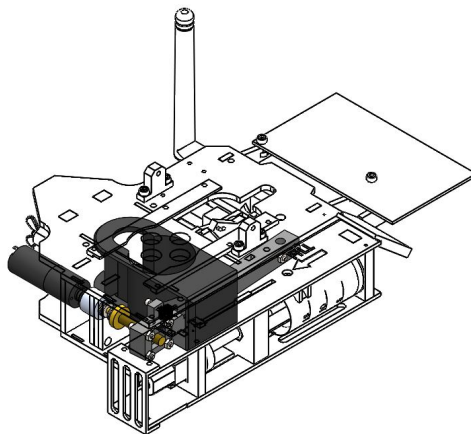
**Subsystems:** Each subsystem was completely redesigned, but the same four subsystems (hopper, loading/releasing, piercing, injection) are present as in V1.0.



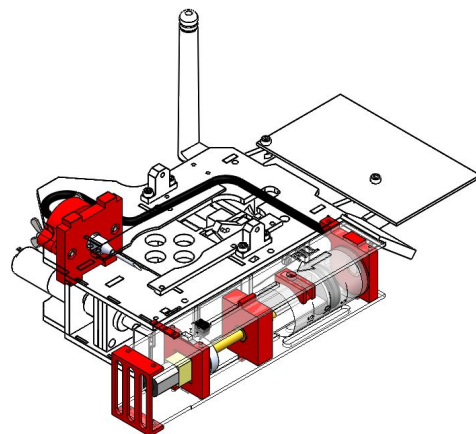
(a) V2.0 hopper mechanism



(b) V2.0 loading/releasing mechanism



(c) V2.0 piercing mechanism



(d) V2.0 injection mechanism

Figure 5.9: The four subsystems that make up version 2.0 of the fire ignition mechanism of the UAS-FF

Figure 5.9 shows the four subsystems of version 2.0.

**Hopper Mechanism:** By reducing the number of spheres carried per deployment in the hopper, the necessary complexity of the hopper was also reduced. We returned to a purely gravity fed design, but we were able to align the spheres single file in a column. This configuration did not require any active agitation while still being able to operate without jamming. The hopper forms a “C” shape as shown in Figure 5.10. The top half of the hopper chute angles backwards to fit more spheres without it being excessively tall, and it also distributes the mass about the UAV Center of Gravity (CG).

The bottom half of the hopper chute moves the ignition mechanism, which is relatively front heavy, towards the back of the UAV, which helps to centralize mass in the sagittal plane. The CG of the UAV is shown in blue and the CG for the ignition mechanism is shown in green.

**Loading Process:** After the spheres are loaded into the hopper chute, the mechanism is ready to begin priming the spheres with antifreeze and dropping them to ignite a fire. The loading/releasing mechanism is comprised of a 10g gearmotor that drives a rocker arm connected to two hatch doors by pushrod linkages. One hatch door is above the piercing ram chamber and one is below.

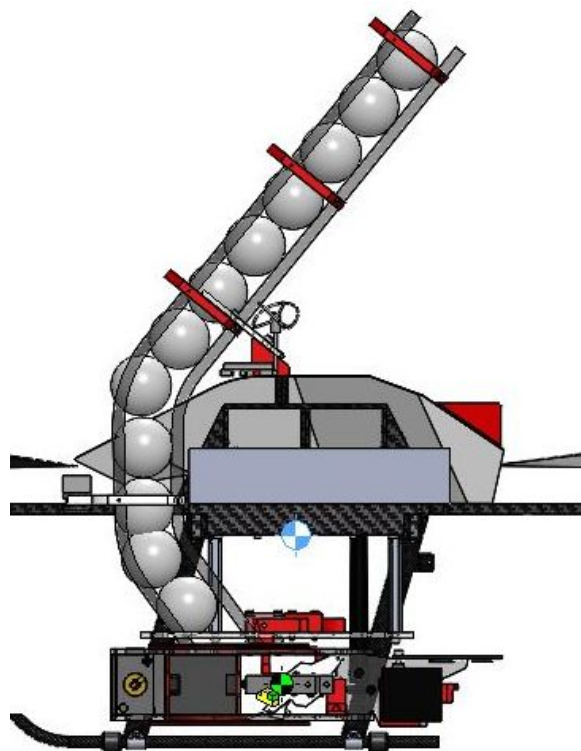


Figure 5.10: Section View: “C” shaped hopper chute to help keep design compact and align center of mass with UAV center

The top hatch door opens to allow a sphere to drop into the piercing ram chamber from the hopper chute, shown in Figure 5.11 with some of the frame components removed for clarity.

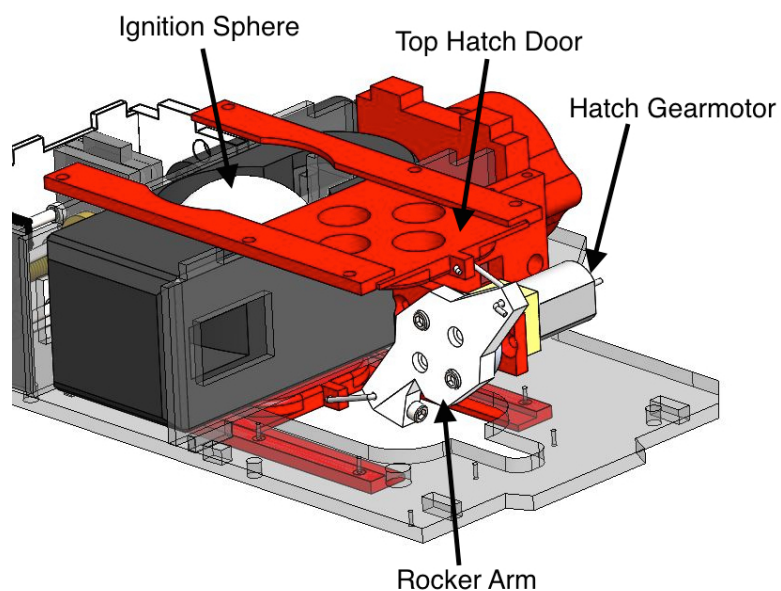


Figure 5.11: Loading/releasing mechanism positioning a sphere in preparation for puncturing

**Piercing Process:** Once a sphere has been loaded into the piercing ram, the Faulhaber motor turns the lead screw which actuates the lever that runs through an arched channel in the piercing ram which punctures the ball on the needle. Figure 5.12 shows a section view with components removed for clarity where the lever is fully actuated and a sphere is punctured on the needle. The piercing mechanism on V2.0 was much more reliable than the piercing mechanism of V1.0, which used a direct drive system where the lead screw that actuated the pierce ram was fixed to the motor on one end but was floating on the other end. This caused deflection of the pierce ram if the sphere was misaligned and caused problems ranging from a bent needle to failure to pierce the sphere wall. It also resulted in inefficient operation because friction losses increased signifi-



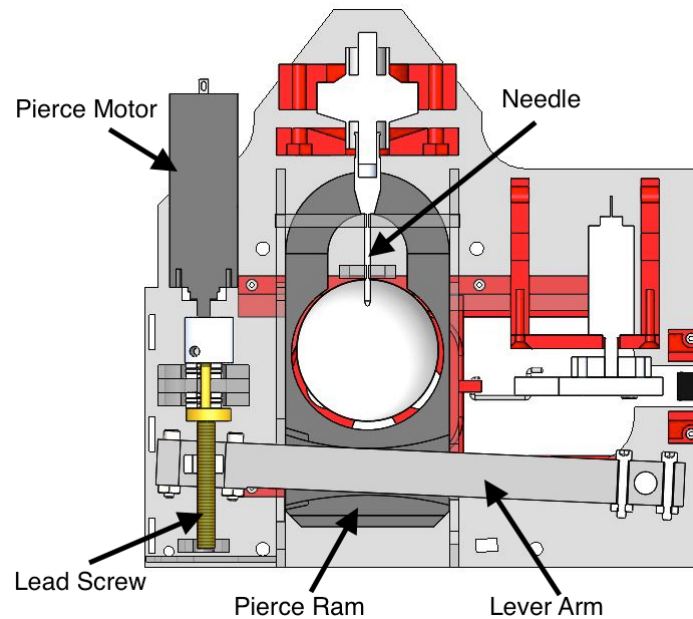


Figure 5.12: Section View: Piercing mechanism punctures a sphere for injection

cantly when the ram deflected. V2.0 abandoned the direct drive concept for the pierce mechanism to improve performance at the cost of slightly more complexity and being larger. For V2.0, the pierce lead screw is fixed radially on one end to the motor and on the other end by a bushing to eliminate deflection and wobbling for more efficient torque transmission. The lead screw is also supported by dual thrust bearings to protect the motor from axial force. The lead screw drives a lever which transmits its force to the pierce ram approximately 75% of the lever length from the lever fulcrum. This increases the axial force produced by the motor/lead-screw combination but reduces linear travel speed. We felt it was an acceptable trade-off to increase cycle time slightly to gain the extra force to ensure we could puncture through any part of the ignition sphere no matter how thick. The pierce ram on V2.0 is tightly constrained by an acrylic plate on all four sides to ensure that it can only travel directly in line with the needle, which has helped ensure all force coming from the motor is directed to puncturing the

sphere. Additionally, the tighter constraint has prevented bending any needles.

**Injection Process:** After the sphere has been punctured on the needle, the injection system is ready to inject antifreeze into the spheres. Figure 5.13 shows the components of the injection mechanism. A 10g gearmotor drives a lead screw, which pushes the injection ram connected to the plunger of a syringe. The syringe is connected to a tube which transfers the antifreeze around the entire mechanism to the back of the needle that the ball is punctured on. Separating the needle from being directly connected to the syringe was significant improvement over V1.0 because it allowed us to make the mechanism much more compact. Making the lead screw directly inline with the syringe also made this mechanism more compact and because the movement of the syringe plunger is tightly constrained, the inline drive system is not plagued by the same issues of the inline drive of the pierce mechanism from version 1.0.

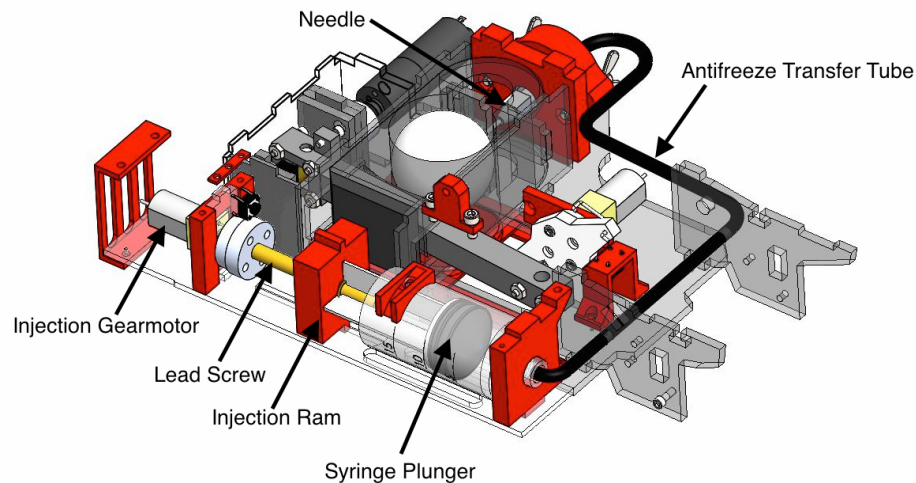


Figure 5.13: Injection mechanism primes the sphere with antifreeze

**Releasing Process:** After the ball is primed with antifreeze, the loading releasing mechanism opens the bottom hatch, which simultaneously closes the top hatch to prevent any of the spheres in the hopper chute from dropping through

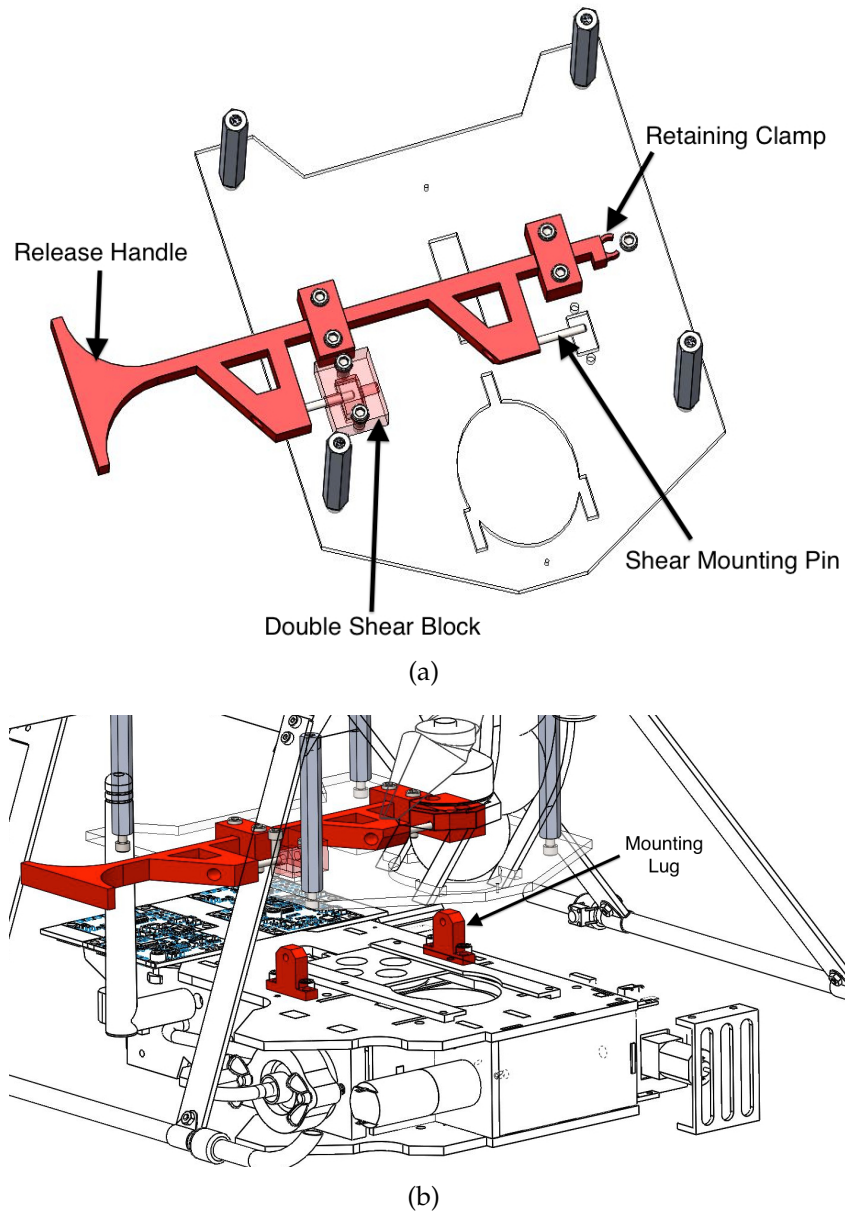


Figure 5.14: Version 2.0 mounting mechanism that securely holds but quickly releases the mechanism

the mechanism. Once the bottom hatch is open, the piercing mechanism runs backwards and the lead screw pushes the lever back which pushes the piercing ram backwards, pulling the ball off the needle and over the open hole in the bottom frame plate and the sphere falls free of the mechanism. The loading/re-

leasing mechanism again opens the top hatch, which closes the bottom hatch. Another sphere drops into the piercing ram and the whole process repeats.

**Mounting Mechanism:** The final mechanism that was redesigned for version 2.0 is the mounting mechanism. Figure 5.14 shows the designed mechanism both individually and on the UAV. Figure 5.14(a) shows some of the features including the quick release handle that slides the shear mounting pin in and out of the double shear block, as well as the retaining clamp that fits around the head of the socket head cap screw to keep the release handle in place. Figure 5.14(b) shows the mounting mechanism mounted on the vehicle with the ignition device below it ready to be mounted. The mounting lug on top of the ignition device slides into the double shear block on the mounting mechanism and then the release handle is pushed in to slide the shear mounting pin through to secure the ignition device to the UAV.

### 5.3 Evaluation

Throughout development we performed a series of tests that ranged from simulation to outdoor tests. The hardware simulation tests mainly helped assess the stability of the vehicle when equipped with the dropper, and identify the points of major mechanical stress while puncturing a sphere. Additionally, we learned that minor modifications can have significant impact on the performance of the hardware. Because of weight restrictions, our hardware components were sized to operate near their functional limits. Adding a small amount of lubricant or trimming a component's size to allow a



Figure 5.15: UAS-FF Version 1.0.3 in flight

slightly looser fit sometimes means the difference between success and failure. On the software end, we tested the response of the system to motor stalls and encoder failures both before injection, and in the critical moment after injection to ensure that the system takes the best steps to remove an injected sphere. Indoor controlled ignition tests were key in helping us understand the factors that affect the ignition process, and assess the reliability of critical steps like the injection and dropping sequence, which integrates software and hardware components. For example, this let us learn about the unexpected variability of the piercing duration depending on whether the needle hits a seam in the sphere. In this setting we also assessed the precision of the path planners and checked the emergency procedures. The outdoor tests without ignition helped us assess the communication and control components, and to understand the effect of wind on the vehicle and the spheres. For example, at 200m we were able to receive 100% of the commands sent, and with winds under 5m/s (close to the recommended limit for performing prescribed burns) the maximum horizontal sphere deflection was within 25% of the dropping altitude. Non-flying outdoor tests were also used to evaluate and refine the dropper.

Last and perhaps more compelling, we recently completed two outdoor tests in realistic yet controlled contexts.

### **5.3.1 Version 1.0.3 Evaluation**

The first test was with Version 1.0.3 (Version 2.0 had not yet been designed) in the Loess Canyon region, in southwestern Nebraska shown in Figure 5.16. It required coordination with the fire council of the area (that includes the land owners) and the Federal Aviation Administration. Under the guidance of the burn boss, we

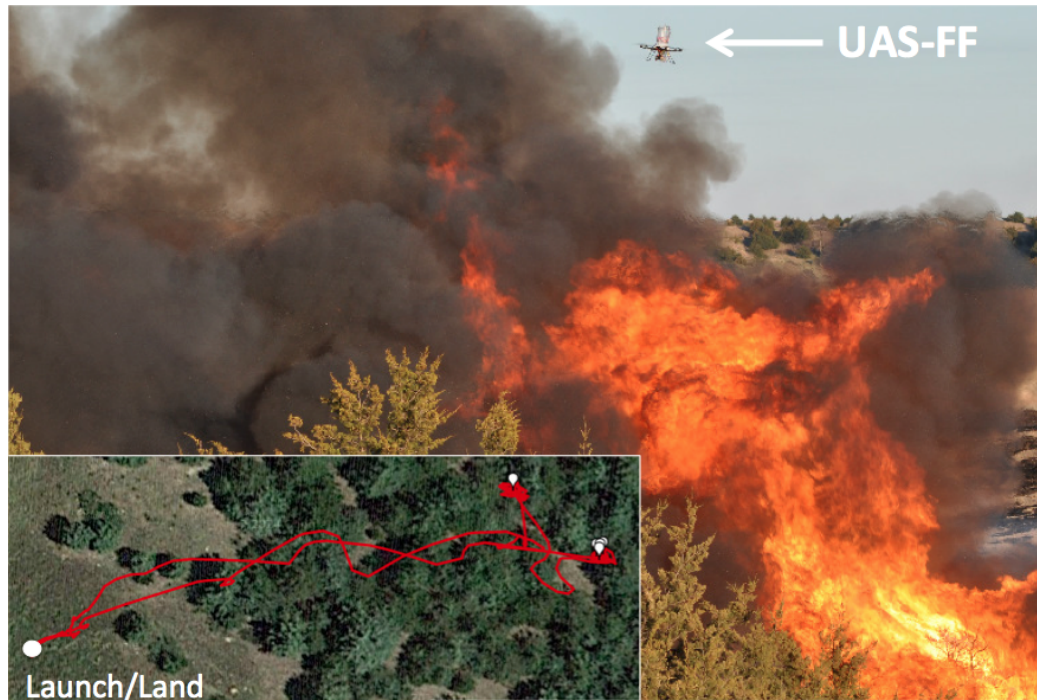


Figure 5.16: UAS-FF returning from a sortie, flying 10 meters over ignited trees. In-picture shows trajectory on a 50m by 35m area, white markers indicate spheres dropped.

targeted an area of approximately 150 acres, within a larger effort to ignite over 2000 acres that involved about 60 firefighters for a full day. We performed 5 sorties over 3 canyons, each over 400m in length and 100m wide, filled with a mix of dry and green cedar (an invasive species in this area). The picture within Figure 5.16 shows one of these sorties, lasting approximately 5 minutes, with the red line capturing the vehicle path and the white markers showing the locations where fire ignition spheres were dropped. In the end, we dropped approximately 80 delayed ignition spheres over a period of 75 minutes and were able to safely ignite large portions of two of the three canyons. We had to halt the process on the third canyon as the injection mechanism got stuck and we did not deem it safe to relaunch the vehicle within the time available as the day was ending.

The feedback we have received from the ultimate users of the technology is



extremely encouraging, with a mix of enthusiasm, valid concerns, and uncertainty, but hope about the potential of the system. We realized that UAS-FF could replace extremely risky ignition operations over canyons or uneven terrain, like Loess Canyon, that is being performed by firefighters on foot or on ATVs. These operations typically require a reach of a few hundred meters and the ability to exit very quickly. At the same time, when observing the firefighters it was evident that the system must be able to tolerate sparse operator attention as they are consuming a lot of information through their own senses and are often on the move. One final critical conclusion we came to after the Loess Canyon burn was that we needed to make some changes to the design of the mechanism (Version 1.0.3). This mechanism had been tested extensively, both in the lab and outdoors, and as parts wore, its performance had started to decrease and problematic design features were causing failures more frequently. The Loess Canyon burn showed us that the UAS-FF system needed to be more reliable and not require adjustment or tuning in the field because there is no time for this when it is called upon to perform its function. We examined the design of Version 1.0.3 and determined that it was worth the extra work to do a complete redesign, even with our second field test only weeks away.

### **5.3.2 Version 2.0.1 Evaluation**

The second test was at Homestead National Monument near Beatrice in southeast Nebraska. Between the two tests, we rapidly developed Version 2.0.1 of the UAS-FF in preparation to ignite a 26 acre burn unit slated for a prescribed burn. On April 22nd, 2016, the wind direction and speed were ideal to burn the unit and test out the very recently completed UAS-FF V2.0.

Firefighters backburned the perimeter of the field and the UAS-FF flew five sorties over the interior of the unburned fuel in the unit, dropping ignition spheres along the flight paths shown in Figure 5.18.

We experimented with multiple ignition patterns as directed by the burn boss to evaluate their effectiveness.

The wind was blowing from the north so most of our ignition lines were perpendicular to the wind direction because this was assumed to be most effective, but we also tried one line parallel with the wind direction and one burn pattern that was more concentrated but that combined both perpendicular and parallel lines with respect to the wind direction.

Version 2.0 of the UAS-FF performed extremely well and without failure to the best of our knowledge. We successfully injected and dropped 60 ignition spheres and burned roughly 20 of the 26 acres before the burn boss made the decision that the ground crew needed to help finish off the unit before the wind had the opportunity to change direction. Figure 5.19 shows a series of images taken from a live video feed from the UAS-FF recorded at a ground station and stitched together in post-processing.

The left locations were ignited first and it appears that all 12 ignition spheres dropped successfully ignited, although the last dropped locations on the right have not progressed far.

One lesson we learned from the test at Homestead National Monument was that the process of redeploying the UAS-FF needs to be improved. It took us a



Figure 5.17: UAS-FF Version 2.0.1 outfitted for deployment



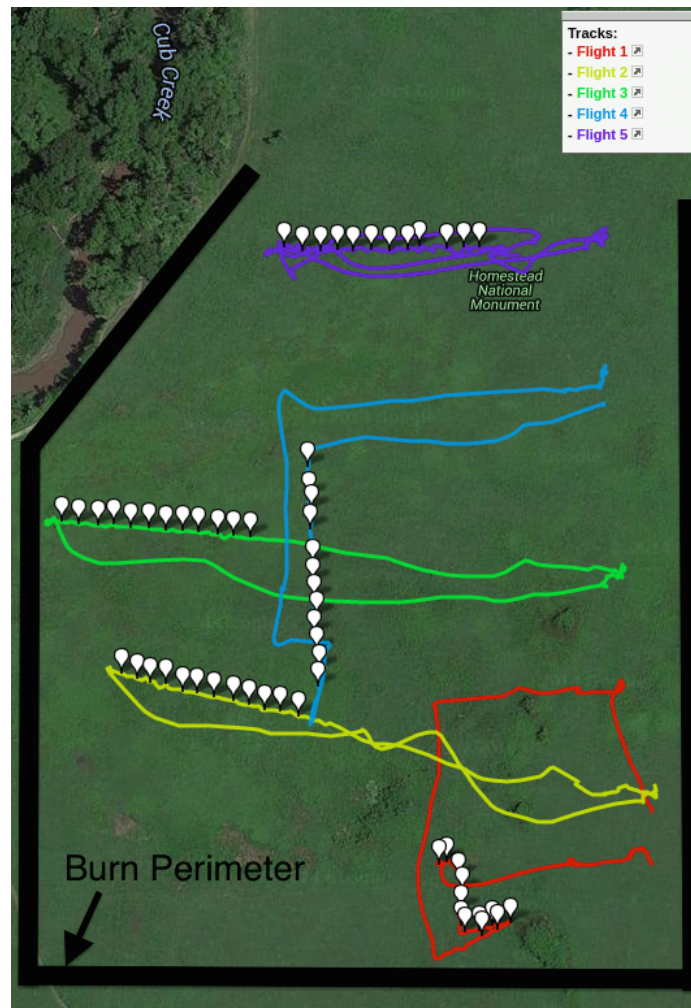


Figure 5.18: Burn unit with flight paths flown by UAS-FF and burn perimeter started from the ground marked

minimum of approximately seven minutes from the time we landed until we were ready to redeploy. While on the ground, we replaced the UAV battery, removed the mechanism to refill the antifreeze reservoir, reloaded the hopper chute with spheres, saved data, reset the ground station and prepared for the next flight. For true field use, the data collection will not be a factor and the ground station will be more compact and streamlined but the process of replacing the consumable components needs to be addressed to make it faster and less involved.



Figure 5.19: Locations of dropped ignition spheres as seen from the UAS-FF's perspective

## 5.4 Conclusion and Contributions

We successfully designed, prototyped, and field tested two versions of the UAS-FF. Version 1.0 successfully burned 150 acres of the Loess Canyon area in southwest Nebraska and version 2.0 successfully burned a 26 acre burn unit at Homestead National Monument in southeast Nebraska. Version 2.0 improved upon version 1.0 by being smaller, stronger, and more reliable. We overcame the challenges of designing a mechanism that is small enough to fit on a UAV, yet still works with industry standard ignition spheres, which require significant force to puncture. Through tightly integrating the mechanical, electrical, and software design with the UAV, we created a system capable of highly accurate, autonomous aerial ignitions. We believe this is the first autonomous robot system that has been designed for and used to ignite prescribed fires. This system has the potential and has shown significant promise to keep firefighters out of danger during interior ignitions and to make aerial ignition safe, affordable, and accessible for fire crews of any size.

- Christian Laney was responsible for designing the PCB and populating the PCB. He also did much of the electrical integration with the mechanism.

- Evan Beachly and Christian Laney designed the software and Christian performed the testing for the early revisions and Evan did so for the later revisions.
- I was responsible for the design, prototyping and physical tests of the mechanical device.
- I was responsible for maintaining, fixing and modifying the mechanisms when they required revisions to increase their strength and durability after field tests exposed weak components.

## Chapter 6

# Conclusion and Future Work

Interaction with the environment will be a key utility of the next generation of UAVs. In this thesis we developed a number of electro-mechanical systems that augment existing UAVs or work alongside them to enable environmental interactions. Key to all of these systems was the development of light-weight and robust mechanical designs that meet the requirements of the scientists and practitioners that use them.

### 6.1 UAV Sensing and Sampling

We designed two versions of a peristaltic pump and compared it to a Micropump with an impeller that has been used in some of our earlier work. The main challenge was designing a pump that was light enough for the UAV, while still providing a high enough flow rate and remaining within the power limitations available. Through lab testing, we characterized the pumps' efficiencies at various heights and operating voltages and determined the maximum functional pumping height for our particular setup is just over 6m. We field tested the pump in

an experiment looking for Zebra mussel veligers, and while none were found due to a dormant population at the time of testing, we were satisfied that the pump performed as intended. Future work will include more tests for invasive species, like Zebra mussels and using the peristaltic pumps in more sampling field experiments.

We constructed and lab tested three types of temperature sensor for use in creating 3D thermal structure maps of bodies of water using a UAV. We successfully field tested one of these sensors, the MS5803, and created a  $10 \times 10 \times 2.5$  m temperature map of Big Lake at BORR in California which resulted in a journal article titled "Obtaining the Thermal Structure of Lakes from the Air" [17] in *Water*. The biggest challenges were capturing temperature data with a slow sensor and then designing a new sensor with a much faster response time to be field tested in the future. Future work will include using this faster sensor that we characterized after the tests at BORR to allow us to map larger areas faster.

## 6.2 Waterbug

In conclusion, the Waterbug satisfies its design goals of being inexpensive, small in size, light enough to be carried by a UAV, and being capable of descending to 10m, collecting a sample and ascending to the surface. It also successfully achieved neutral buoyancy 80% of the time over a range of parameters simulating field conditions. We demonstrated the effectiveness of developing an accurate system model and combining the advantages of feed-forward, feedback and pre-compensation to develop an algorithm that is successful despite using very inexpensive hardware, which was the main challenge. We showed that it is possible to reduce cost and complexity by using only uni-directional control and still achieve

similar results as other, more complex systems utilizing bi-directional control.

The main source of failure in the neutral buoyancy algorithm stemmed from mechanical inconsistency of the buoyancy syringes. Finding a suitable lubricant to grease the seals on the syringe may help by reducing the friction between the seal and body to provide more consistent results. It is also possible that such an inexpensively manufactured component could have slight dimensional or surface finish variations and one syringe may perform better than another. Selectively taking the best syringes from a sample set may improve the success rate of the neutral buoyancy algorithm. In summary, more investigation needs to be performed to find a suitable solution for this particular issue.

In addition, we plan to conduct field tests, because inevitably, nature finds ways of exposing weaknesses in design that the lab environment never can. The Waterbug will be used to collect actual water samples and these samples will need to be compared to samples collected through traditional means to make sure the Waterbug does not ruin the fidelity of the samples.

A paper on the design, testing, and evaluation of the Waterbug was accepted at IROS 2016.

## **6.3 UAS-FF**

We successfully designed, prototyped and field tested two versions of the UAS-FF. Version 1.0 successfully burned a portion of the Loess Canyon in southwest Nebraska and version 2.0 successfully burned a 26 acre burn unit at Homestead National Monument in southeast Nebraska. Version 2.0 improved upon version 1.0 by being smaller, stronger, and more reliable. We overcame the challenges

of designing a mechanism that is small enough to fit on a UAV, yet still works with industry standard ignition spheres, which require significant force to puncture. Through tightly integrating the mechanical, electrical, and software design with the UAV, we created a system capable of highly accurate, autonomous aerial ignitions. We believe this is the first autonomous robot system that has been designed for and used to ignite prescribed fires. This system has the potential and has shown significant promise to keep firefighters out of danger and make aerial ignition safe, affordable and accessible for fire crews of any size. Future work will include the continued development of the ground station, software, and integration of the UAS-FF with the methods and procedures of fire crews.

## 6.4 Contributions

- The peristaltic pump allows water to be pumped to greater heights and from greater depths while being more resilient to clogging and more sterile than previous work with the water sampling UAV. I was responsible for designing, building and testing the peristaltic pump. The water sampling UAV was part of previous works by John-Paul Ore and other members of the NIMBUS Lab [7] [8]. Prior to my involvement, the Water Sampler could autonomously collect surface samples up to 12in deep using a miniature impeller pump. The new design has been tested at 3m depth and at a height of over 6m from the water.
- The temperature sensors make it possible for a UAV to quickly collect the data to construct three-dimensional thermal structure maps. We successfully mapped a  $10 \times 10 \times 2.5\text{m}$  area during field trials using one of the temperature sensors. John-Paul Ore was responsible for designing the PCB for the

MS5803 pressure/temperature sensor and I characterized its performance in the lab setting and we jointly performed the field tests with the assistance of Michaela Chung and Sally Thompson from UC-Berkeley. The data was published in an article titled “Obtaining the Thermal Structure of Lakes from the Air” [17] in *Water*. I was responsible for constructing the thermocouples and the characterization of all the temperature sensors in the lab setting.

- The Waterbug sub-surface sampler seeks to fill the needs of water sampling that the UAV cannot satisfy. It is capable of retrieving data and water samples from depths up to 10m and is small and light enough to be deployed and retrieved via UAV. Additionally, an algorithm was developed that allows the Waterbug to achieve neutral buoyancy to monitor a specific point of interest in the water column despite only using uni-directional buoyancy control. The development of this robot resulted in a conference paper titled “The Waterbug Sub-Surface Sampler: Design, Control and Analysis” accepted at the International Conference on Intelligent Robots and Systems 2016 [18]. I was responsible for designing and prototyping the Waterbug. David Anthony worked with me on the first couple revisions and John-Paul Ore allowed me to use the MS5803 PCB for the embedded system running the control software that I wrote. Dave and John-Paul both helped me construct the electronics and trouble-shoot software and communication bugs.
- The UAS-FF is an unmanned aerial system capable of autonomously igniting prescribed fires and has the potential to significantly reduce the danger to firefighters performing interior ignitions for controlled burns. It is small, light, and inexpensive enough that it is accessible to a crew of any size.



The system successfully ignited over 150 acres over two field tests. Christian Laney was responsible for designing the PCB and populating the PCB. He also did much of the electrical integration with the mechanism. Evan Beachly and Christian Laney designed the software. Christian performed the testing for the early revisions and Evan did so for the later revisions. I was responsible for the design, prototyping and physical tests of the mechanical device as well as for maintaining, fixing and modifying the mechanisms when they required revisions to increase their strength and durability after field tests exposed weak components.

# Bibliography

- [1] W. K. Dodds, W. W. Bouska, J. L. Eitzmann, T. J. Pilger, K. L. Pitts, A. J. Riley, J. T. Schloesser, and D. J. Thornbrugh, "Eutrophication of us freshwaters: analysis of potential economic damages," *Environmental Science & Technology*, vol. 43, no. 1, pp. 12–19, 2008. [1.1](#)
- [2] E. Corcoran, *Sick water?: the central role of wastewater management in sustainable development: a rapid response assessment*. UNEP/Earthprint, 2010. [1.1](#)
- [3] F. Wilde, D. Radtke, J. Gibbs, and R. Iwatsubo, "National field manual for the collection of water-quality data," *US Geological Survey Techniques of Water-Resources Investigations, Book*, vol. 9, 1998. [1.2](#)
- [4] A. J. Erickson, P. T. Weiss, and J. S. Gulliver, "Water sampling methods," in *Optimizing Stormwater Treatment Practices*, pp. 163–192, Springer, 2013. [1.2](#)
- [5] M. Dunbabin, A. Grinham, and J. Udy, "An autonomous surface vehicle for water quality monitoring," in *Australasian Conference on Robotics and Automation (ACRA)*, pp. 2–4, 2009. [1.2](#)
- [6] N. A. Cruz and A. C. Matos, "The mares auv, a modular autonomous robot for environment sampling," in *OCEANS 2008*, pp. 1–6, IEEE, 2008. [1.2](#)

- [7] J.-P. Ore, S. Elbaum, A. Burgin, B. Zhao, and C. Detweiler, "Towards autonomous aerial water sampling," in *Robotic Science And Systems (RSS) - Workshop on Robotics for Environmental Monitoring, Berlin, Germany*, p. TBA, 2013. [1.2](#), [1.4](#), [2.3](#), [6.4](#)
- [8] J.-P. Ore, S. Elbaum, A. Burgin, B. Zhao, and C. Detweiler, "Autonomous aerial water sampling," in *Proc. of The 9th Intl. Conf. on Field and Service Robots (FSR). Brisbane, Australia*, vol. 5, 2013. [1.2](#), [1.4](#), [2.3](#), [4.1](#), [6.4](#)
- [9] D. A. Dellasala, J. E. Williams, C. D. Williams, and J. F. Franklin, "Beyond smoke and mirrors: a synthesis of fire policy and science," *Conservation Biology*, vol. 18, no. 4, pp. 976–986, 2004. [1.3](#), [2.5](#)
- [10] T. J. Hawbaker, V. C. Radeloff, S. I. Stewart, R. B. Hammer, N. S. Keuler, and M. K. Clayton, "Human and biophysical influences on fire occurrence in the united states," *Ecological applications*, vol. 23, no. 3, pp. 565–582, 2013. [1.3](#)
- [11] F. H. Johnston, S. B. Henderson, Y. Chen, J. T. Randerson, M. Marlier, R. S. DeFries, P. Kinney, D. M. Bowman, and M. Brauer, "Estimated global mortality attributable to smoke from landscape fires," *Environmental health perspectives*, vol. 120, no. 5, 2012. [1.3](#)
- [12] V. Ambrosia, S. Wegener, T. Zajkowski, D. Sullivan, S. Buechel, F. Enomoto, B. Lobitz, S. Johan, J. Brass, and E. Hinkley, "The ikhona unmanned airborne system (uas) western states fire imaging missions: from concept to reality (2006–2010)," *Geocarto International*, vol. 26, no. 2, pp. 85–101, 2011. [1.3](#)
- [13] L. Merino, F. Caballero, J. R. Martínez-de Dios, I. Maza, and A. Ollero, "An unmanned aircraft system for automatic forest fire monitoring and mea-

- surement," *Journal of Intelligent & Robotic Systems*, vol. 65, no. 1-4, pp. 533–548, 2012. [1.3](#)
- [14] L. Merino, J. R. Martínez-de Dios, and A. Ollero, "Cooperative unmanned aerial systems for fire detection, monitoring, and extinguishing," in *Handbook of Unmanned Aerial Vehicles*, pp. 2693–2722, Springer, 2015. [1.3](#)
- [15] D. W. Casbeer, R. W. Beard, T. W. McLain, S.-M. Li, and R. K. Mehra, "Forest fire monitoring with multiple small uavs," in *American Control Conference, 2005. Proceedings of the 2005*, pp. 3530–3535, IEEE, 2005. [1.3](#)
- [16] R. C. Skeelee and G. A. Hollinger, "Aerial vehicle path planning for monitoring wildfire frontiers," in *Field and Service Robotics*, pp. 455–467, Springer, 2016. [1.3](#)
- [17] M. Chung, C. Detweiler, M. Hamilton, J. Higgins, J.-P. Ore, and S. Thompson, "Obtaining the thermal structure of lakes from the air," *Water*, vol. 7, no. 11, p. 6467, 2015. [1.4](#), [3.3.3](#), [3.3.4](#), [4.1](#), [4.4.3](#), [6.1](#), [6.4](#)
- [18] J. Higgins and C. Detweiler, "The waterbug sub-surface sampler: Design, control and analysis," in *2016 IEEE/RSJ International Conference on Intelligent Robots and Systems, 2016. (IROS 2016). Proceedings*, p. TBA, 2016. [1.4](#), [6.4](#)
- [19] E. Allen, "Instrument for transfusion of blood," Nov. 8 1881. US Patent 249,285. [2.1](#)
- [20] L. Cao, S. Mantell, and D. Polla, "Design and simulation of an implantable medical drug delivery system using microelectromechanical systems technology," *Sensors and Actuators A: Physical*, vol. 94, no. 1, pp. 117–125, 2001. [2.1](#)

- [21] M. M. Teymoori and E. Abbaspour-Sani, "Design and simulation of a novel electrostatic peristaltic micromachined pump for drug delivery applications," *Sensors and Actuators A: Physical*, vol. 117, no. 2, pp. 222–229, 2005. [2.1](#)
- [22] W. Jackman, W. Loughheed, E. Marliss, B. Zinman, and A. Albisser, "For insulin infusion: a miniature precision peristaltic pump and silicone rubber reservoir," *Diabetes Care*, vol. 3, no. 2, pp. 322–331, 1980. [2.1](#)
- [23] M. Hu, H. Du, and S. Ling, "A digital miniature pump for medical applications," *Mechatronics, IEEE/ASME Transactions on*, vol. 7, no. 4, pp. 519–523, 2002. [2.1](#)
- [24] K. Nakahara, M. Yamamoto, Y. Okayama, K. Yoshimura, K. Fukagata, and N. Miki, "A peristaltic micropump using traveling waves on a polymer membrane," *Journal of Micromechanics and Microengineering*, vol. 23, no. 8, p. 085024, 2013. [2.1](#)
- [25] S. Dirven, W. Xu, L. K. Cheng, and J. Bronlund, *Robot Intelligence Technology and Applications 2: Results from the 2nd International Conference on Robot Intelligence Technology and Applications*, ch. Soft-Robotic Peristaltic Pumping Inspired by Esophageal Swallowing in Man, pp. 473–482. Cham: Springer International Publishing, 2014. [2.1](#)
- [26] *Bartendro Cocktail Mixing Robot*. [2.1](#)
- [27] S. Kingsley, "Pump suitable for moving sludges and the like," Apr. 5 1949. US Patent 2,466,618. [2.1](#)

- [28] C. Brown, "Apparatus and method for the treatment of liquid/solid mixtures," Dec. 13 2011. US Patent 8,074,809. [2.1](#)
- [29] "Linear hose pump for conveying and metering powder," Sept. 12 2012. CN Patent App. CN 201,210,131,992. [2.1](#)
- [30] T. Eisemon, "Peristaltic pumps waste less water in wastewater treatment," March 2010. [pumpsandsystems.com](#) [Online; posted March-2010]. [2.1](#)
- [31] P. Dale, "Peristaltic pumps handle abrasive chemicals in water and wastewater treatment," November 2014. [pumpsandsystems.com](#) [Online; posted November-2014]. [2.1](#)
- [32] T. O'Donnell, "Peristaltic pumps offer protection in mining operations," February 2016. [pumpsandsystems.com](#) [Online; posted February-2016]. [2.1](#)
- [33] T. Loudin, "Rolling design peristaltic pumps increase equipment longevity," November 2015. [\[Online; posted November-2015\]](#). [2.1](#)
- [34] D. Caissie, "The thermal regime of rivers: a review," *Freshwater Biology*, vol. 51, no. 8, pp. 1389–1406, 2006. [2.2](#)
- [35] J. S. Alabaster and R. S. Lloyd, *Water quality criteria for freshwater fish*. No. 3117, Elsevier, 2013. [2.2](#)
- [36] T. Jankowski, D. M. Livingstone, H. Bührer, R. Forster, and P. Niederhauser, "Consequences of the 2003 european heat wave for lake temperature profiles, thermal stability, and hypolimnetic oxygen depletion: Implications for a warmer world," *Limnology and Oceanography*, vol. 51, no. 2, pp. 815–819, 2006. [2.2](#)

- [37] W. M. Mooji, S. Hulsmann, L. N. De Senerpont Domis, B. A. Nolet, P. L. E. Bodelier, P. C. M. Boers, D. P. L. M., H. J. Gons, B. W. Ibelines, R. Noordhuis, R. Portielje, K. Wolfstein, and E. H. R. R. Lammens, "The impact of climate change on lakes in the netherlands: a review," *Aquatic Ecology*, vol. 39, pp. 381–400, 2005. [2.2](#)
- [38] D. E. Bowler, R. Mant, H. Orr, D. M. Hannah, and A. S. Pullin, "What are the effects of wooded riparian zones on stream temperature?," *Environmental Evidence*, vol. 1, pp. 1–9, 2012. [2.2](#)
- [39] R. L. Vannote and B. W. Sweeney, "Geographic analysis of thermal equilibria: a conceptual model for evaluating the effect of natural and modified thermal regimes on aquatic insect communities," *The American Naturalist*, vol. 115, no. 5, pp. 667–695, 1980. [2.2](#)
- [40] J. V. Ward and J. A. Stanford, "Thermal responses in the evolutionary ecology of aquatic insects," *Annual Review of Entomology*, vol. 27, pp. 97–117, 1992. [2.2](#)
- [41] R. L. Wilby, H. Orr, G. Watts, R. W. Battarbee, P. M. Berry, R. Chadd, S. J. Dugdale, M. J. Dunbar, J. A. Elliott, C. Extence, D. M. Hannah, N. Holmes, A. C. Johnson, B. Knights, N. J. Milner, S. J. Ormerod, D. Solomon, R. Timlett, P. J. Whitehead, and P. J. Wood, "Evidence needed to manage freshwater ecosystems in a changing climate: Turning adaptation principles into practice," *Science of the Total Environment*, vol. 408, no. 19, pp. 4150–4164, 2010. [2.2](#)

- [42] D. Tonolla, V. Acuna, U. Uehlinger, T. Frank, and K. Tockner, "Thermal heterogeneity in river floodplains," *Ecosystems*, vol. 13, no. 5, pp. 727–740, 2010. [2.2](#)
- [43] Q. W. Lewis and B. L. Rhoads, "Rates and patterns of thermal mixing at a small stream confluence under variable incoming flow conditions," *Hydrological Processes*, vol. 29, no. 20, pp. 4442–4456, 2015. [2.2](#)
- [44] S. P. Rice, P. Kiffney, C. Greene, and G. R. Pess, "The ecological importance of tributaries and confluences," in *River confluences, tributaries and the fluvial network* (S. Rice, A. Roy, and B. Rhoads, eds.), Chichester, UK: John Wiley & Sons, 2008. [2.2](#)
- [45] J. L. Ebersole, W. J. Liss, and C. A. Frissell, "Cold water patches in warm streams: Physicochemical characteristics and the influence of shading," *JAWRA Journal of the American Water Resources Association*, vol. 39, no. 2, pp. 355–368, 2003. [2.2](#)
- [46] L. B. Holtby, "Effects of logging on stream temperatures in carnation creek, british columbia, and associated impacts on the coho salmon (*Oncorhynchus kisutch*)," *Canadian Journal of Fisheries and Aquatic Sciences*, vol. 45, no. 3, pp. 502–515, 1988. [2.2](#)
- [47] C. E. Torgersen, D. M. Price, H. W. Li, and B. A. McIntosh, "Multiscale thermal refugia and stream habitat associations of chinook salmon in northeastern oregon," *Ecological Applications*, vol. 9, no. 1, pp. 301–319, 1999. [2.2](#)
- [48] A. S. Ruesch, C. E. Torgersen, J. J. Lawler, J. D. Olden, E. E. Peterson, C. J. Volk, and D. J. Lawrence, "Projected climate-induced habitat loss for



- salmonids in the john day river network, oregon, usa," *Conservation Biology*, vol. 26, no. 5, pp. 873–882, 2012. [2.2](#)
- [49] A. Wüest and A. Lorke, "Small-scale hydrodynamics in lakes," *Annual Review of Fluid Mechanics*, vol. 35, no. 1, pp. 373–412, 2003. [2.2](#)
- [50] J. R. Romero and G. W. Kling, "Spatial-temporal variability in surface layer deepening and lateral advection in an embayment of lake victoria, east africa," *Limnology and Oceanography*, vol. 47, no. 3, pp. 656–671, 2002. [2.2](#)
- [51] C. E. Oldham and J. J. Sturman, "The effect of emergent vegetation on convective flushing in shallow wetlands: Scaling and experiments," *Limnology and Oceanography*, vol. 46, no. 6, pp. 1486–1493, 2001. [2.2](#)
- [52] G. Horsch and H. Stefan, "Convective circulation in littoral water due to surface cooling," *Limnology and Oceanography*, vol. 33, no. 5, pp. 1068–1083, 1988. [2.2](#)
- [53] C. Michael and F. John, "The radiatively driven natural convection beneath a floating plant layer," *Limnology and Oceanography*, vol. 39, no. 5, pp. 1186–1194, 1994. [2.2](#)
- [54] R. D. Moore, D. Spittlehouse, and A. Story, "Riparian microclimate and stream temperature response to forest harvesting: A review<sup>1</sup>," *Journal of the American Water Resources Association*, vol. 41, no. 4, p. 813, 2005. [2.2](#)
- [55] J. S. Selker, L. Thevenaz, H. Huwald, A. Mallet, W. Luxemburg, N. Van De Giesen, M. Stejskal, J. Zeman, M. Westhoff, and M. B. Parlange, "Distributed fiber-optic temperature sensing for hydrologic systems," *Water Resources Research*, vol. 42, no. 12, 2006. [2.2](#)

- [56] C. E. Torgerson, R. N. Faux, B. A. McIntosh, N. J. Poage, and D. J. Norton, "Airborne thermal remote sensing for water temperature assessment in rivers and streams," *Remote Sensing of Environment*, vol. 76, pp. 386–398, 2001. [2.2](#), [3.3.3](#)
- [57] R. N. Handcock, A. R. Gillespie, K. A. Cherkauer, J. E. Kay, S. J. Burges, and S. K. Kampf, "Accuracy and uncertainty of thermal-infrared remote sensing of stream temperatures at multiple spatial scales," *Remote Sensing of Environment*, vol. 100, no. 4, pp. 427–440, 2006. [2.2](#)
- [58] A. M. Jensen, B. T. Neilson, M. McKee, and Y. Chen, "Thermal remote sensing with an autonomous unmanned aerial remote sensing platform for surface stream temperatures," pp. 5049–5052. [2.2](#)
- [59] T. J. Schmugge, W. P. Kustas, J. C. Ritchie, T. J. Jackson, and A. Rango, "Remote sensing in hydrology," *Advances in Water Resources*, vol. 25, pp. 1367–1385, 2002. [2.2](#)
- [60] J. E. Kay, S. K. Kampf, R. N. Handcock, K. A. Cherkauer, A. R. Gillespie, and S. J. Burges, "Accuracy of lake and stream temperatures estimated from thermal infrared images," *Journal of the American Water Resources Association*, vol. 41, no. 5, pp. 1161–1175, 2005. [2.2](#)
- [61] M. Dunbabin, A. Grinham, and J. Udy, "An autonomous surface vehicle for water quality monitoring," pp. 2–4. [2.2](#)
- [62] B. Laval, J. S. Bird, and P. D. Helland, "An autonomous underwater vehicle for the study of small lakes," *Journal of Atmospheric and Oceanic Technology*, vol. 17, no. 1, pp. 69–76, 2000. [2.2](#), [3.3.3](#)

- [63] Y. Zhang, M. A. Godin, J. G. Bellingham, and J. P. Ryan, "Using an autonomous underwater vehicle to track a coastal upwelling front," *IEEE Journal of Oceanic Engineering*, vol. 37, no. 3, pp. 338–347. [2.2](#)
- [64] A. Marouchos, B. Muir, R. Babcock, and M. Dunbabin, "A shallow water auv for benthic and water column observations," pp. 1–7. [2.2](#)
- [65] F. Zhang, J. Wang, J. Thon, C. Thon, E. Litchman, and X. Tan, "Gliding robotic fish for mobile sampling of aquatic environments," pp. 167–172. [2.2](#)
- [66] I. F. Akyildiz, D. Pompili, and T. Melodia, "Underwater acoustic sensor networks: research challenges," *Ad Hoc Networks*, vol. 3, pp. 257–279, May 2005. [2.3](#)
- [67] K. Akkaya and A. Newell, "Self-deployment of sensors for maximized coverage in underwater acoustic sensor networks," *Comput. Commun.*, vol. 32, pp. 1233–1244, May 2009. [2.3](#)
- [68] I. Vasilescu, C. Detweiler, and D. Rus, "AquaNodes: An underwater sensor network," in *Proceedings of the Second Workshop on Underwater Networks, WuWNet '07*, (New York, NY, USA), pp. 85–88, ACM, 2007. [2.3](#)
- [69] M. Doniec, I. Vasilescu, M. Chitre, C. Detweiler, M. Hoffmann-Kuhnt, and D. Rus, "Aquaoptical: A lightweight device for high-rate long-range underwater point-to-point communication," in *OCEANS 2009, MTS/IEEE Biloxi - Marine Technology for Our Future: Global and Local Challenges*, pp. 1–6, Oct 2009. [2.3](#)
- [70] C. Detweiler, M. Doniec, M. Jiang, M. Schwager, R. Chen, and D. Rus, "Adaptive decentralized control of underwater sensor networks for mod-

- eling underwater phenomena,” in *Proceedings of the 8th ACM Conference on Embedded Networked Sensor Systems, SenSys '10*, (New York, NY, USA), pp. 253–266, ACM, 2010. [2.3](#)
- [71] C. Detweiler, M. Doniec, I. Vasilescu, E. Basha, and D. Rus, “Autonomous depth adjustment for underwater sensor networks,” in *Proceedings of the Fifth ACM International Workshop on UnderWater Networks, WUWNet '10*, (New York, NY, USA), pp. 12:1–12:4, ACM, 2010. [2.3](#)
- [72] A. Tinka, Q. Wu, K. Weekly, C. A. Oroza, J. Beard, and A. M. Bayen, “Heterogeneous fleets of active and passive floating sensors for river studies,” *Journal of Field Robotics*, 2015. [2.3](#), [4.3](#)
- [73] J. Austin and S. Atkinson, “The design and testing of small, low-cost gps-tracked surface drifters,” *Estuaries*, vol. 27, no. 6, pp. 1026–1029, 2004. [2.3](#), [4.3](#)
- [74] J. Beard, K. Weekly, C. Oroza, A. Tinka, and A. M. Bayen, “Mobile phone based drifting lagrangian flow sensors,” in *Networked Embedded Systems for Every Application (NESEA), 2012 IEEE 3rd International Conference on*, pp. 1–7, IEEE, 2012. [2.3](#)
- [75] J. Jaffe and C. Schurgers, “Sensor networks of freely drifting autonomous underwater explorers,” in *Proceedings of the 1st ACM international workshop on Underwater networks*, pp. 93–96, ACM, 2006. [2.3](#), [4.3](#)
- [76] R. E. Davis, C. C. Eriksen, and C. P. Jones, “Autonomous buoyancy-driven underwater gliders,” 2002. [2.3](#)

- [77] H. Singh, A. Can, R. Eustice, S. Lerner, N. McPhee, O. Pizarro, and C. Roman, "Seabed AUV offers new platform for high-resolution imaging," *Eos, Transactions American Geophysical Union*, vol. 85, no. 31, pp. 289–296, 2004. [2.3](#)
- [78] G. Dudek, P. Giguere, C. Prahacs, S. Saunderson, J. Sattar, L. A. Torres-Mendez, M. Jenkin, A. German, A. Hogue, A. Ripsman, and others, "Aqua: An amphibious autonomous robot," *IEEE Computer*, vol. 40, no. 1, pp. 46–53, 2007. [2.3](#)
- [79] R. Camilli, B. Bingham, M. Jakuba, H. Singh, and J. Whelan, "Integrating in-situ chemical sampling with AUV control systems," in *OCEANS'04. MTTs/IEEE TECHNO-OCEAN'04*, vol. 1, pp. 101–109, IEEE, 2004. [2.3](#)
- [80] B. Allen, R. Stokey, T. Austin, N. Forrester, R. Goldsborough, M. Purcell, and C. von Alt, "REMUS: a small, low cost AUV; system description, field trials and performance results," in *OCEANS'97. MTS/IEEE Conference Proceedings*, vol. 2, pp. 994–1000, IEEE, 1997. [2.3](#)
- [81] A. Lucieer, D. Turner, D. H. King, and S. A. Robinson, "Using an unmanned aerial vehicle (UAV) to capture micro-topography of antarctic moss beds," *International Journal of Applied Earth Observation and Geoinformation*, vol. 27, pp. 53–62, 2014. [2.3](#)
- [82] A. Mohapatra, N. Gautam, and R. Gibson, "Combined routing and node replacement in energy-efficient underwater sensor networks for seismic monitoring," *IEEE Journal of Oceanic Engineering*, vol. 38, pp. 80–90, Jan. 2013. [2.3](#)

- [83] P. van Walree and R. Otnes, "Ultrawideband underwater acoustic communication channels," *IEEE Journal of Oceanic Engineering*, vol. 38, pp. 678–688, Oct. 2013. [2.3](#)
- [84] Y. Noh, U. Lee, S. Han, P. Wang, D. Torres, J. Kim, and M. Gerla, "DOTS: A propagation delay-aware opportunistic MAC protocol for mobile underwater networks," *IEEE Transactions on Mobile Computing*, vol. 13, pp. 766–782, Apr. 2014. [2.3](#)
- [85] D. Pompili, T. Melodia, and I. Akyildiz, "A CDMA-based medium access control for UnderWater acoustic sensor networks," *IEEE Transactions on Wireless Communications*, vol. 8, pp. 1899–1909, Apr. 2009. [2.3](#)
- [86] L. E. Bird, A. Sherman, and J. Ryan, "Development of an active, large volume, discrete seawater sampler for autonomous underwater vehicles," in *OCEANS 2007*, pp. 1–5, IEEE, 2007. [2.3](#), [4.3.2](#)
- [87] J.-P. Ore, S. Elbaum, A. Burgin, B. Zhao, and C. Detweiler, *Field and Service Robotics: Results of the 9th International Conference*, ch. Autonomous Aerial Water Sampling, pp. 137–151. Cham: Springer International Publishing, 2015. [2.3](#)
- [88] K. J. Aström and R. M. Murray, *Feedback systems: an introduction for scientists and engineers*. Princeton university press, 2010. [2.4](#)
- [89] N. S. Nise, *CONTROL SYSTEMS ENGINEERING, (With CD)*. John Wiley & Sons, 2007. [2.4](#)

- [90] J. H. Kim and H. B. Park, "H state feedback control for generalized continuous/discrete time-delay system," *Automatica*, vol. 35, no. 8, pp. 1443–1451, 1999. [2.4](#)
- [91] S. Skogestad and I. Postlethwaite, *Multivariable feedback control: analysis and design*, vol. 2. Wiley New York, 2007. [2.4](#)
- [92] Y. Lee, J. Lee, and S. Park, "Pid controller tuning for integrating and unstable processes with time delay," *Chemical Engineering Science*, vol. 55, no. 17, pp. 3481–3493, 2000. [2.4](#)
- [93] H. Shu and Y. Pi, "Pid neural networks for time-delay systems," *Computers & Chemical Engineering*, vol. 24, no. 2, pp. 859–862, 2000. [2.4](#)
- [94] S. E. Hamamci, "An algorithm for stabilization of fractional-order time delay systems using fractional-order pid controllers," *Automatic Control, IEEE Transactions on*, vol. 52, no. 10, pp. 1964–1969, 2007. [2.4](#)
- [95] Z. Shafiei and A. Shenton, "Frequency-domain design of pid controllers for stable and unstable systems with time delay," *Automatica*, vol. 33, no. 12, pp. 2223–2232, 1997. [2.4](#)
- [96] M. Baeza, M. De Luis, J. Raventós, and A. Escarré, "Factors influencing fire behaviour in shrublands of different stand ages and the implications for using prescribed burning to reduce wildfire risk," *Journal of Environmental Management*, vol. 65, no. 2, pp. 199–208, 2002. [2.5](#)
- [97] M. A. Finney, C. W. McHugh, and I. C. Grenfell, "Stand-and landscape-level effects of prescribed burning on two arizona wildfires," *Canadian Journal of Forest Research*, vol. 35, no. 7, pp. 1714–1722, 2005. [2.5](#)

- [98] M. M. Boer, R. J. Sadler, R. S. Wittkuhn, L. McCaw, and P. F. Grierson, "Long-term impacts of prescribed burning on regional extent and incidence of wildfire evidence from 50 years of active fire management in sw australian forests," *Forest Ecology and Management*, vol. 259, no. 1, pp. 132–142, 2009. [2.5](#)
- [99] J. M. DiTomaso, M. L. Brooks, E. B. Allen, R. Minnich, P. M. Rice, and G. B. Kyser, "Control of invasive weeds with prescribed burning 1," *Weed technology*, vol. 20, no. 2, pp. 535–548, 2006. [2.5](#)
- [100] E. A. Allen, J. C. Chambers, and R. S. Nowak, "Effects of a spring prescribed burn on the soil seed bank in sagebrush steppe exhibiting pinyon-juniper expansion," *Western North American Naturalist*, vol. 68, no. 3, pp. 265–277, 2008. [2.5](#)
- [101] J. F. Stritzke and T. G. Bidwell, "Eastern redcedar and its control," *Weeds Today*, vol. 15, no. 3, pp. 7–8, 1984. [2.5](#)
- [102] J. E. Keeley, "Fire management impacts on invasive plants in the western united states," *Conservation Biology*, vol. 20, no. 2, pp. 375–384, 2006. [2.5](#)
- [103] "Rock Creek Rx Entrapment FLA," Nov. 2011. [2.5](#)
- [104] R. Fahy, "Wildland Firefighter Fatalities, 1999-2008," July 2009. [2.5](#)
- [105] *Premo Plastic Sphere Dispenser (PSD)*. [2.5](#)
- [106] A. Hodgson and N. P. Cheney, "Aerial ignition for backburning," *Australian Forestry*, vol. 33, no. 4, pp. 268–274, 1969. [2.5](#)
- [107] D. Wade, "Ignition devices for prescribed burning," Mar. 2013. [2.5](#)



- [108] G. Ippolito and E. Murray, "Two U.S Forest Service Employees & Pilot Die in Helicopter Crash," Mar. 2005. [2.5](#)
- [109] *Pyroshot Hand Launcher*. [2.5](#)
- [110] *Pyroshot Gas Powered Hand Launcher*. [2.5](#)
- [111] *Premo Fireballs*. [2.5](#), [5.1](#)
- [112] *Aerostat Aerial Ignition Spheres*. [2.5](#), [5.1](#)
- [113] "Ascending Technologies." [3.1](#), [4.1](#)
- [114] *Micro Metal Gearmotor, 50:1 ratio*. [3.2.2](#), [5.2.1](#)
- [115] *25D Metal Gearmotor*. [3.2.2](#)
- [116] "TCS Micropumps, UK. Model M200S-SUB - <http://micropumps.co.uk/TCSM200orange.htm>." [3.2.2](#)
- [117] J.-P. Ore, "Autonomous aerial water sampling," Master's thesis, University of Nebraska, 2014. [3.2.3](#)
- [118] *Sefar Nitex - 64 micron Datasheet*. [3.2.4](#)
- [119] B. Garnier and F. Lanzetta, "Tutorial 4: In situ realization/characterization of temperature/heat flux sensors.," [3.3.2](#)
- [120] *US Sensor - GP103J4F Datasheet*. [3.3.2](#)
- [121] S. W. Tyler, J. S. Selker, M. B. Hausner, C. E. Hatch, T. Torgerson, C. E. Thodal, and S. G. Schladow, "Environmental temperature sensing using raman spectra dts fiber-optic methods," *Water Resources Research*, vol. 45, no. 4, pp. 1–11, 2009. [3.3.3](#)

- [122] J. S. Selker, L. Thevenaz, H. Huwald, A. Mallet, W. Luxemburg, N. van de Giesen, M. Stejskal, J. Zeman, M. Westhoff, and M. B. Parlange, "Distributed fiber-optic temperature sensing for hydrologic systems," *Water Resources Research*, vol. 42, pp. 1–8, 2006. [3.3.3](#)
- [123] A. D. Eaton and M. A. H. Franson, *Standard methods for the examination of water & wastewater*. American Public Health Association, 2005. [4.1](#)
- [124] B. Garnier and F. Lanzetta, "Tutorial 4: In situ realization/characterization of temperature/heat flux sensors," tech. rep., Technical Report, 2011. [4.1](#)
- [125] ASCO - RB Series Solenoid Datasheet. [4.3.1](#)
- [126] J. B. Martin, R. G. Thomas, and K. M. Hartl, "An inexpensive, automatic, submersible water sampler," *Limnology and Oceanography: Methods*, vol. 2, no. 12, pp. 398–405, 2004. [4.3.2](#)
- [127] I. A. Blakar, "A close-interval water sampler with minimal disturbance properties," *Limnology and Oceanography*, vol. 24, no. 5, pp. 983–988, 1979. [4.3.2](#)
- [128] A. Marouchos, C. Neill, M. Sherlock, T. Goodwin, E. Van Ooijen, J. Cordell, and B. Tilbrook, "Challenges in autonomous coastal water sampling," in *Oceans, 2012*, pp. 1–6, IEEE, 2012. [4.3.2](#)
- [129] Ultimaker2 - <https://ultimaker.com>. [4.3.4](#)
- [130] Atmel - Atmega328P Datasheet. [4.4.1](#)
- [131] Digi International - XBee. [4.4.2](#)
- [132] Measurement Specialties - MS5803-05BA Datasheet. [4.4.3](#)

[133] *Toshiba Semiconductor - SSM3K329RLFCT-ND Datasheet.* [4.4.4](#)

[134] *Lithium Polymer Battery.* [4.4.5](#)

[135] *seamos.* [4.4.6](#)

[136] *Robot Operating System.* [4.4.6](#)

[137] "Boyle's law." [4.5.3](#)

[138] *Generant - Valve Cv Calculator Datasheet.* [4.5.3](#)

[139] *Micro Metal Gearmotor, 300:1 ratio.* [5.2.1](#)